Structural health monitoring of carbon fiber reinforced polymers and carbon nanotube modified adhesive joints via electrical resistance measurement

Vom Promotionsausschuss der
Technischen Universität Hamburg

zur Erlangung des akademischen Grades
Doktor-Ingenieur (Dr.-Ing.)

genehmigte Dissertation

von
Till Augustin

aus
Hamburg

2018

Gutachter:	Prof. Dr.-Ing. habil. Bodo Fiedler
	Prof. Dr.-Ing. habil. Marcus Rutner
Vorsitzender des Prüfungsausschusses:	Prof. Dr. habil. Michael Morlock
Tag der mündlichen Prüfung:	17.07.2018

Technisch-Wissenschaftliche Schriftenreihe

Herausgeber:

Prof. Dr.-Ing. habil. Bodo Fiedler

Anschrift:

Technische Universität Hamburg
Institut für Kunststoffe und Verbundwerkstoffe
Denickestraße 15
21073 Hamburg

Band 32:

Structural health monitoring of carbon fiber reinforced polymers and carbon nanotube modified adhesive joints via electrical resistance measurement

Till Augustin

1. Auflage

Hamburg 2018

ISSN 2625-6029

Bibliographische Information der Deutschen Nationalbibliothek:

Die deutsche Nationalbibliothek verzeichnet diese Publikation in der Deutschen Nationalbibliothek; detaillierte Informationen sind im Internet über http://www.dnb.de abrufbar.

Kurzfassung

Schäden an Faser-Kunststoff-Verbunden können zu deutlich reduzierter Festigkeit und Lebensdauer führen. Um Inspektionskosten zu verringern und die Sicherheit zu erhöhen, kann es vorteilhaft sein, die Integrität der Struktur während des Betriebes zu überwachen. Ein vielversprechender Ansatz ist die elektrische Widerstandsmessung. In dieser Arbeit wird die Schadensdetektion mittels elektrischer Widerstandsmessung an kohlenstofffaserverstärktem Kunststoff und an kohlenstoffnanopartikelmodifizierten Klebeverbindungen untersucht.

Silbernanopartikeltinte wird auf kohlenstofffaserverstärkten Kunststoff und auf Prepregs aufgedruckt und mechanische Tests mit elektrischen Widerstandsmessungen demonstrieren die Möglichkeit, Delaminationen und Zwischenfaserbrüche in situ zu detektieren. Bei integrierten Leiterbahnen ist eine Schadensdetektion je nach Ausrichtung von Fasern und Leiterbahn möglich. Zusätzlich wird die Schlagschadendetektion an Platten und einem Stringer demonstriert.

Elektrische Widerstandsmessungen in der Ebene und in Dickenrichtung an mit Kohlenstoffnanoröhren modifizierten Klebefilmen auf Epoxidbasis zeigen die Möglichkeit einer Detektion und Lokalisierung von Schlagschäden. Darüber hinaus zeigt sich ein linearer Zusammenhang zwischen elektrischem Widerstand und Klebefilmdicke. Zyklische Ermüdungstests mit gleichzeitiger elektrischer Widerstandsmessung an geschäfteten Klebeverbindungen werden durchgeführt. Rissinitiierung und -wachstum, die durch digitale Bildkorrelation beobachtet werden, können durch Erhöhung des elektrischen Widerstandes nachgewiesen werden.

Bei der Untersuchung von kohlenstoffnanopartikelmodifizierten Epoxidfasern zeigt sich eine gute Korrelation zwischen der elektrischen Widerstandsänderung und dem Spannungs-Dehnungs-Verhalten unter Zugbelastung, was ein hohes Potential für die Verwendung von mit Kohlenstoffnanoröhren modifiziertem Kunststoff als alternatives Material für leitfähige Pfade und neuartige Sensoren aufzeigt.

Abstract

Damage in fiber reinforced polymers (FRP) can lead to significantly reduced strength and fatigue life. To minimize inspection costs and enhance the safety of FRP structures, it can be beneficial to monitor the integrity of the structure during operation. A promising method to achieve this is to conduct electrical resistance measurements. In this thesis, damage detection via electrical resistance measurements on carbon fiber reinforced polymers and on carbon nanoparticle modified adhesive joints is investigated.

Silver nanoparticle-based ink is printed onto carbon fiber reinforced polymers and onto prepregs and mechanical tests with simultaneous electrical resistance measurements demonstrate the possibility to detect delaminations and inter-fiber failures in situ. For integrated conductive paths, a damage detection via electrical resistance measurement is possible with continuous integrated paths. To obtain continuous integrated paths, the fiber direction of the adjacent layer of the path needs to be taken into account. In addition, impact damage detection is demonstrated for plate specimens as well as for an omega stringer.

In-plane and through-thickness electrical resistance measurements on carbon nanotube modified epoxy-based adhesive films show the possibility of accurate detection and localization of impact damages. Furthermore, a linear correlation of electrical resistance and bond line thickness exists. Cyclic fatigue tests of adhesively bonded scarf joints with simultaneous electrical resistance measurements are conducted to investigate the damage detection and localization of repaired composite parts during operation. Crack initiation and growth, observed by digital image correlation, can be detected by an increase of electrical resistance.

Finally, carbon nanoparticle modified epoxy fibers are investigated. Good correlation between electrical resistance change and stress strain behavior under tensile loads is observed, indicating high potential for using carbon nanotube modified polymer as an alternative material for conductive paths and sensor applications.

Content

List of abbreviations

CB	Carbon black
CFRP	Carbon fiber reinforced polymer
CNT	Carbon nanotube
CVD	Chemical vapor deposition
CVM	Comparative vacuum monitoring
DC	Direct current
DIC	Digital image correlation
DSC	Differential scanning calorimetry
EIT	Electrical impedance tomography
ERC	Electrical resistance change
ERT	Electrical resistivity tomography
FBG	Fiber Bragg grating
FLG	Few layer graphene
FOS	Fiber optic sensors
FRP	Fiber reinforced polymer
GFRP	Glass fiber reinforced polymer
IFF	Inter-fiber failure
MWCNT	Multi wall carbon nanotube
NDT	Non-destructive testing
PAN	Polyacrylonitrile
SEM	Scanning electron microscopy
SHM	Structural health monitoring
SWCNT	Single wall carbon nanotube
UD	Unidirectional

1 Introduction

Fiber reinforced polymers (FRP) are widely used as structural materials, in particular for lightweight applications in aerospace, automotive, wind energy, and shipbuilding industry, because of their high specific strength and stiffness, as well as fatigue and corrosion resistance. However, FRP exhibit a complex damage behavior with a variety of damage types with different propagation characteristics, which differ from damages in traditionally used metallic materials. In carbon fiber reinforced polymer (CFRP) structures used in aircrafts, impact events typically cause barely visible damages including delaminations, inter-fiber failures (IFF), and fiber fractures, significantly reducing strength and fatigue life of the structures [1–4]. Therefore, it is important to detect such safety crucial damages. Nowadays, to assure integrity and avoid catastrophic failures of FRP structures, periodic inspections are carried out using non-destructive testing (NDT) methods, such as ultrasonic, visual, vibrational, and radiographic inspection, as well as acoustic methods, and thermography [5–8]. These inspections can be time-consuming and costly due to expensive NDT processes and the resulting downtime. Hence, a permanent monitoring of the integrity of the structure during operation, namely a structural health monitoring (SHM) system, can be valuable in many cases. SHM offers a high potential to enhance safety, reliability, and cost efficiency of fiber reinforced structures.

Several approaches to monitor composites during operation exist. One promising SHM method for materials, which are electrically conductive, is to perform electrical resistance measurements. In contrast to many other SHM methods, no sensors have to be embedded into or applied onto the part, since the material itself acts as a sensor. Hence, the structural properties of the composite part are not negatively influenced, as this can be the case e.g. for large embedded sensors.

For CFRP, numerous studies demonstrate that the high electrical conductivity of the carbon fibers can be used for in situ strain and damage

monitoring via electrical resistance measurements [9–18]. To exploit the electrical conductivity of CFRP and use the material itself as a sensor, a reliable contacting of the material is crucial to enable electrical resistance measurement during operation. Due to its excellent reproducibility and high potential for industrial automation, inkjet printing is a promising technology to place conductive paths on the material and realize reliable contacts for electrical resistance measurements [19–21]. However, inkjet-printed conductive paths on CFRP for damage sensing have not been investigated so far but could bring damage sensing closer to industrial application.

In glass fiber reinforced polymers (GFRP), both the polymeric matrix and the glass fibers are electrically insulating and therefore electrical resistance measurements are not possible. The same goes for all other FRP with non-conductive fiber materials. However, modification of a polymer matrix with carbon nanoparticles can lead to a conductive network resulting in an electrically conductive composite material with piezoresistive properties allowing for strain and damage sensing [17,22–30].

The vast majority of investigated approaches to monitor composite materials during operation applies to intact parts without macroscopic discontinuities that have not undergone a repair process. Yet, structural composites are often subject to impacts that can be critical and need to be repaired. If an SHM system is used to monitor the integrity of the structure, the repaired part and in particular the adhesive joint need to be monitored as well. Especially for adhesively bonded scarfed repairs, as standard in aircraft industry for secondary structures, epoxy-based adhesive films join the scarfed parent laminate and the repair patch. The electrically non-conducting bond line inhibits electrical resistance measurements and therefore the application of an electrical conductivity–based SHM method to monitor the bonded joint. However, a carbon nanoparticle modification of the adhesive film can enable electrical resistance measurements. SHM of adhesively bonded composite joints has been studied using different methods [31–33]. Yet, only few studies on structural health monitoring of adhesively bonded joints via electrical resistance measurements exist, and a

detection with localization of damages in adhesive films via electrical resistance measurements has not been investigated to date.

1.1 Aims and scope

With the challenges pointed out above, the aims of this thesis are to:

1. investigate the damage sensing potential of a silver ink based electrode system, which is directly printed onto and below the CFRP surface with a focus on the detection and localization of inter-fiber failures, delaminations, and impact damages;
2. develop a non-destructive testing method to monitor the integrity of composite bonded joints and repairs with the ability to localize the damage by using an electrically conductive carbon nanoparticle modified adhesive film that enables electrical resistance measurements through the bond line;
3. study the damage sensing capability of carbon nanoparticle modified epoxy fibers as an alternative to metal-based electrodes.

1.2 Structure

This thesis is structured in eight chapters. The following chapter 2 contains an overview of the scientific and technological background on the investigated composites with emphasis on electrical properties and structural health monitoring of composites. Chapter 3 describes the materials used for the experiments. Chapter 4 presents investigations on damage detection and localization of CFRP with printed conductive paths by electrical resistance measurements. Chapter 5 deals with investigations on damage detection and localization of carbon nanoparticle modified adhesive films used in bonded composite joints. In chapter 6, the suitability of carbon nanoparticle modified epoxy fibers for damage sensing is investigated. Finally, chapter 7 concludes the main findings and chapter 8 contains an outlook for further research.

Parts of this thesis have been published in journal articles listed on page 127.

2 Scientific and technological background

2.1 Carbon fiber reinforced polymers

2.1.1 Structure and electrical properties of carbon fibers

Different types of carbon fibers are available and the properties vary in a wide range, depending on the used precursor and the production process. Commercial carbon fibers are made by using either polyacrylonitrile (PAN) or pitch as precursor [34]. Nowadays, the majority of carbon fibers are obtained from PAN [35].

Carbon fibers consist of at least 92 % carbon by weight [36]. They comprise of two-dimensional graphene layers in which sp^2 hybridized carbon atoms are hexagonally arranged. The carbon atoms are covalently bonded by three σ-bonds (in plane) and a π-bond (out of plane). The σ-bonds contribute to high strength and stiffness whereas the π-bond allows free motion of electrons giving high electrical and thermal conductivity parallel to the fiber axis [34]. Between the layers van der Waals bonds act and the stacking sequence of the layers is ABAB with a spacing of about 0.34 nm. The graphene layers are oriented mainly parallel to the fiber axis and show an inhomogeneous structure with imperfections and a high degree of parallelization near the fiber surface (see Figure 2.1) [37].

Due to this structure, carbon fibers have anisotropic electrical properties. The level of electrical conductivity depends on several parameters as heat treatment, graphitization level, and alignment of carbon units [38]. In fiber direction, PAN-based carbon fibers exhibit an electrical conductivity in the range of about 10^4 – 10^5 S/m, whereas the electrical conductivity of pitch-based fibers lies in the range of about 10^5 – 10^6 S/m [34,35,39]. Perpendicular to the fiber direction, the electrical conductivity is significantly lower [40].

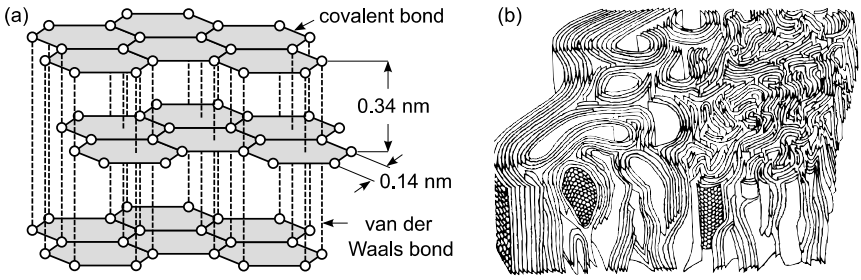

Figure 2.1: Structure of carbon fibers; (a) Crystal structure of a graphite crystal; (b) Schematic structure of a PAN-based carbon fiber [41].

2.1.2 Electrical properties of carbon fiber reinforced polymers

In CFRP, the carbon fibers are electrically conductive (as described above) and the polymer matrix is electrically insulating. The electrical conductivity of epoxy, which is often used as polymeric matrix material, lies in the range of 10^{-14} – 10^{-12} S/m [42–44]. Hence, the electrical conductivity of the fibers (σ_f) is many orders of magnitude higher than the electrical conductivity of the matrix (σ_m). This extreme difference leads to anisotropic electrical properties of the composite material.

If we assume a unidirectional CFRP laminate with equidistant spacing between the carbon fibers and without any touching fibers, the electrical conductivity in fiber direction can be calculated by using the rule of mixture and multiplying the electrical conductivity of the carbon fibers (σ_f) by the fiber volume content (v_f). In this theoretical case, the conductivity perpendicular to the fiber direction is almost zero due to the lack of an electrically conductive network of fibers in transverse direction. Because the conductivity of the matrix is approximately zero, this also results from the rule of mixture perpendicular to the fiber direction where the numerator being the conductivity of the fiber (σ_f) multiplied by the conductivity of the matrix (σ_m) equals zero.

However, in practice, the carbon fibers in a unidirectional laminate are not equidistantly spaced and neighboring fibers touch each other at some points (see Figure 2.2). If a certain fiber volume fraction is exceeded, the fiber-to-fiber contacts result in a conductive network with electrical conductivity in all directions [11]. Compared to the electrical conductivity in fiber direction (σ_0), the electrical conductivity in transverse direction is significantly lower. Furthermore, due to resin rich inter-laminar regions, in thickness direction less fiber-to-fiber contacts per distance are present than in 90°-direction. Hence, the electrical conductivity in 90°-direction (σ_{90}) is higher than the electrical conductivity in thickness direction (σ_t) and we can say that $\sigma_0 > \sigma_{90} > \sigma_t$.

Experiments showed that for typical unidirectional carbon fiber/epoxy composites with a fiber volume content of about $v_f = 50$ % the electrical conductivity ratios can be approximated by $\sigma_{90} / \sigma_0 \approx 10^{-3}$ and $\sigma_t / \sigma_0 \approx 10^{-4}$ [12,45,46]. However, these anisotropy ratios are not valid for all CFRP laminates and can differ because they highly depend on the fiber volume content, as the number of direct fiber contacts increases with the fiber volume content [12,46]. Furthermore, these ratios depend on the thickness of the resin rich inter-laminar regions [47] as well as on the amount of misaligned fibers and the waviness of the fibers and rovings [16].

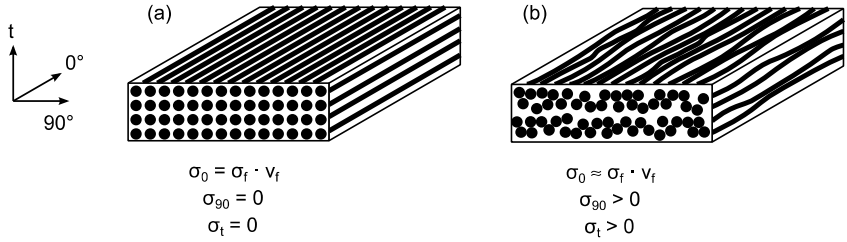

Figure 2.2: Schematic of fiber arrangement in a unidirectional laminate; (a) Theoretical homogeneous arrangement with equidistant spacing between fibers; (b) Real arrangement with different spacing between fibers, waviness of fibers, fiber-to-fiber contacts, and resin rich inter-laminar layer.

Another parameter that influences the electrical conductivity of CFRP laminates is the stacking sequence. In thickness direction, unidirectional laminates exhibit considerably lower electrical conductivity than multidirectional laminates, because more direct fiber contacts are present in case of differently oriented adjacent laminate layers [48–50].

2.2 Carbon nanotube modified polymers

2.2.1 Structure and electrical properties of carbon nanotubes

Carbon nanotubes (CNT) exhibit a hollow cylindrical structure consisting of one or more rolled up coaxial graphene layers with fullerene hemispheres at the ends. The carbon atoms are sp^2 hybridized and hexagonally arranged. Single wall carbon nanotubes (SWCNT) consist of one and multi wall carbon nanotubes (MWCNT) of more than one graphene layer, where the distance between the cylinders is in the same range as the distance of adjacent graphene layers in graphite (0.34 nm) [51,52]. CNT exhibit exceptional high aspect ratios (length/diameter) with values up to several thousand [53] and extremely high strength as well high as elastic modulus values at low density [54–57]. The most commonly used methods for synthetization of CNT are chemical vapor deposition (CVD), arc discharge, and laser ablation, with CVD being the most used method and suitable for scalable industrial productions.

The chirality defines the atomic structure of SWCNT (see Figure 2.3). The chiral vector (c_h) can be described using the vectors a_1 and a_2 in a graphene layer by $c_h = n \cdot a_1 + m \cdot a_2$ with n and m being integers [58]. Depending on the chiral vector SWCNT can have a zigzag (n > 0, m = 0), armchair (n = m), or chiral (n ≠ m, n > 0, m > 0, angle of the chiral vector lies between zigzag and armchair) configuration. The chirality affects the physical properties and in particular the electrical properties of SWCNT.

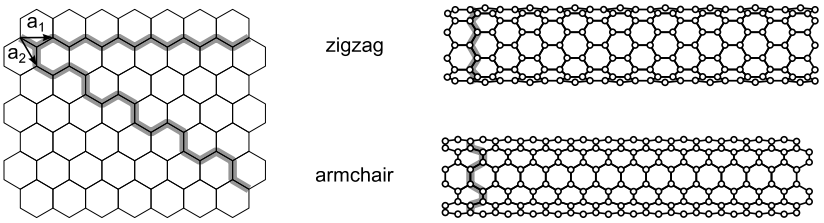

Figure 2.3: Atomic structure of SWCNT, zigzag (n > 0, m = 0) and armchair (n = m).

If $(2 \cdot n + m)/3$ is an integer, the SWCNT are metallic and otherwise semiconducting [59–61]. Hence, the armchair structure always results in metallic properties whereas zigzag and chiral structures can be semiconducting or metallic depending on this condition. In addition to the chirality, defects in the graphene layer can significantly influence the electrical properties of the CNT [62,63].

2.2.2 Electrical properties of carbon nanotube modified polymers

In CNT modified polymers, the CNT are electrically conductive and the polymer is electrically insulating. Modification of a polymer matrix with carbon nanoparticles can lead to a conductive network resulting in an electrically conductive composite material with piezoresistive properties. A conductive network forms above a critical nanoparticle content, the percolation threshold [64], where the electrical conductivity increases several orders of magnitude (see Figure 2.4). At a CNT content of the percolation threshold, first continuous electrically conductive pathways form, which results in a significant increase of electrical conductivity. For increasing CNT content, multiple continuous pathways are present and the

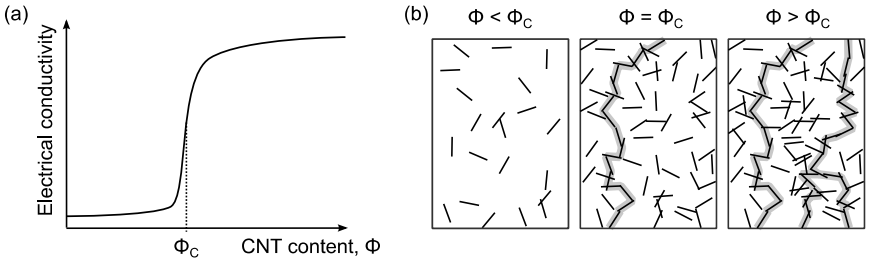

Figure 2.4: Percolation threshold; (a) Electrical conductivity versus CNT content with percolation threshold ϕ_C; (b) Schematic of three different CNT contents; No electrically conductive pathways below percolation threshold, first pathways at percolation threshold, and several pathways above percolation threshold.

electrical conductivity increases further only slightly and runs into a saturation.

Compared to other nanoparticles, CNT offer the advantage that due to their high aspect ratio relatively low percolation thresholds can be obtained. Percolation theory [64,65] assumes homogeneously distributed particles. With the excluded volume concept, the percolation threshold (ϕ_C) of statistically distributed particles can be approximated by $\phi_C = 1/\eta$ (only valid for high aspect ratios (η)) [66]. A typical percolation threshold for a CNT/polymer composite is ϕ_C = 0.1 wt.% (corresponding to a typical aspect ratio of 1000) [67]. However, kinetic percolation, i.e. reagglomeration of particles forming a conductive network, can lead to inhomogeneous particle distribution resulting in percolation thresholds well below the statistically calculated values. In particular, this has been observed for CNT/epoxy composites [43,68,69]. At or above the percolation threshold, experimentally determined electrical conductivities of CNT/polymer composites lie typically in the range of 10^{-5} – 10^{-2} S/m [70,71].

In CNT/polymer composites, two types of electrical resistance form a resistor network for electron conductance: the electrical resistance of the CNT and the electrical resistance at CNT junctions. In typical nanocomposites with low filler content, the individual CNT are surrounded by matrix and direct contacts between neighboring CNT are unlikely. However, even without the presence of direct contacts of neighboring CNT, electrically conductive pathways can form. This can be explained by the quantum mechanics effect called quantum tunneling, stating that the probability for an electron to pass through a potential barrier is non-zero [72]. For CNT/polymer composites, electron tunneling resistance is acknowledged to play the dominant role in electron transport. Therefore, it determines the electrical resistance of the nanocomposite [73,74]. The probability that electron tunneling occurs decreases exponentially with increasing particle distance [75]. Hence, the maximum tunneling distance is only a few nanometer [73].

In an electrically conductive CNT/polymer composite, mechanically two different mechanisms can result in an electrical resistance change (ERC):

1. Damage that causes interruptions of the electrically conductive pathways leading to an irreversible increase of the electrical resistance.
2. Strain that causes a change of the particle distances (tunneling gaps) resulting in a reversible ERC due to the piezoresistive material behavior.

2.3 Structural health monitoring of composites

SHM can be defined as "the process of implementing a damage identification strategy for aerospace, civil and mechanical engineering infrastructure" [76]. SHM is a recent field of research. The first conference exclusively devoted to this topic, the "International Workshop on Structural Health Monitoring" (IWSHM), was initiated in 1997. In 2002, the first issue of a peer-reviewed scientific international journal on this topic, named "Structural Health Monitoring", was published. Since the 1990s, the interest and the amount of conducted research concerning SHM have increased significantly and constantly (see Figure 2.5).

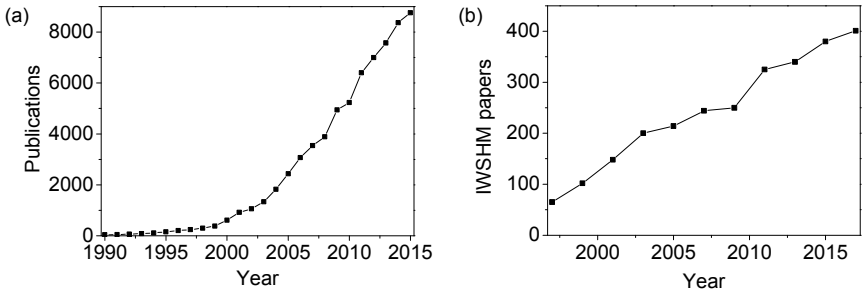

Figure 2.5: Increasing number of publications in the field of structural health monitoring; (a) Scientific publications including patents per year from 1990 – 2015 (obtained by searching "structural health monitoring" via google scholar, 08.01.2018); (b) Number of papers presented at the International Workshop on Structural Health Monitoring (IWSHM) from 1997 – 2017.

2.3.1 Overview of structural health monitoring methods for composites

A broad range of methods for monitoring composite structures exist. SHM methods can be classified into active and passive monitoring methods. In contrast to passive methods, active methods use transducers that inject controlled signals into the structure [77]. The following overview is not

intended to be comprehensive, but only some relevant methods are presented here. Further information on SHM methods can be found e.g. in [78–83].

Fiber optic sensors (FOS) consist of light-conducting fibers out of glass or polymers and can be integrated into composite structures. Due to the refractive index contrast, light can be guided along the fiber length without high losses. Intensity based FOS can monitor strain and transverse crack evolution by measuring the reduction of the optical power due to a length variation of the fiber [84]. As wavelength based FOS mostly **Fiber Bragg grating** (FBG) sensors [85] are used. FBG are periodic variations of the refractive index in the core of an optical fiber [86] that reflect particular wavelengths of light. Length variations of the fiber change the distance of the Bragg gratings resulting in a shift of the reflected wavelengths. With multiple Bragg gratings within one fiber, the local strain distribution and therefore also local damages that result in a change of strain can be monitored [84]. The high fiber diameter of usually > 50 µm can have a negative influence on the structural integrity of a composite laminate [83].

Lamb waves are a form of elastic waves propagating in solid plates [87]. When lamb waves interact with surface damage or internal damages of the material, wave scattering occurs at the damage locations [88]. Usually, piezoelectric transducers are used for excitation and collection of the signals.

Acoustic emission technique is used to detect acoustic signals in form of elastic waves that are caused by the energy release of damages in composite materials. For the detection, surface mounted piezoelectric sensors are used. Matrix cracks, delaminations, and fiber breakage can be detected with this method and a differentiation of the damage types can be obtained, since the different damage types result in characteristic acoustic signals [89]. Since no measurement of the initial condition is possible with this technique, in an SHM system, this method is not suitable as a stand-alone method but can be valuable in addition to another method [90,91]. Furthermore, this method may suffer from background noise.

Comparative vacuum monitoring (CVM) is a method, in which chambers containing either vacuum or atmospheric pressure are oriented in alternating and parallel paths, mounted onto the surface of the structure to be monitored [92]. If a crack on the surface connects adjacent chambers, a leakage path forms and fluid flow takes place. A transducer measures this fluid flow and can detect a crack that connects two chambers [93].

Crack wires comprise of thin optical or electrically conductive fibers that are integrated into the composite [94]. If the stiffness decreases due to damages in the structure, the strength of the crack wires is reached and a rupture of the fibers occurs. Therefore, the light or the electric current is interrupted and with the interruption a damage can be detected.

Vibration-based methods are active approaches that use a specific frequency band to excite a structure [95]. After the excitation, dynamic parameters (natural frequency, frequency response function, damping, mode shapes, etc.) are analyzed and compared with the modal parameters of the undamaged state. Damages that cause changes of the physical properties can be detected by differences in the vibration response [78].

Electrical conductivity methods use electrically conductive self-sensing structures with the ability to monitor their own condition [96]. Due to the inherent electrical conductivity, the structure can be used as a sensor in an SHM system. Electrical methods can be used for electrically conductive composites as CFRP and carbon nanoparticle modified GFRP. Electrical conductivity methods can be classified into electrical impedance tomography (EIT) and ERC methods, which are described in the following sections.

Further SHM methods exist, including strain gauges [97], digital image correlation (DIC) [98], microelectromechanical systems [99], global positioning system (GPS) [100], and others.

When comparing the available SHM methods, the electrical conductivity methods have the significant advantage that the structure itself acts as a sensor. Therefore, no sensors that can lead to detrimental structural properties have to be embedded into the structure, as this is the case e.g. for

FOS. Furthermore, no sensors or devices for exciting the structure have to be applied onto the surface of the structure, as this is the case for many SHM methods mentioned above. Only electrodes need to be in contact with the structure. The advantage obtained from the self-sensing capability makes the electrical conductivity methods promising candidates for future SHM applications. Therefore, the two following sections deal with these methods with regard to CFRP and carbon nanotube modified polymers.

2.3.2 Structural health monitoring of carbon fiber reinforced polymers via electrical conductivity methods

Due to the electrical conductivity of carbon fibers in CFRP structures, the electrical conductivity of the composite can be exploited to monitor the composite in an SHM system. Schulte and Baron [11] first introduced the concept of damage and strain sensing with electrical methods by correlating the electrical resistivity variation with damage and failure of the fibers oriented in loading direction in quasi-static tensile and fatigue tests. Furthermore, the applied strain could be correlated with the measured electrical resistivity. Abry et al. [12] investigated damage sensing capabilities for different fiber volume contents. Seo and Lee [101] showed that the electrical resistance change behaves similar to the stiffness reduction in tensile fatigue tests. They conclude, that the damage can be determined via the electrical resistance change, similar to the stiffness reduction obtained by stiffness measurements. Weber and Schwartz [102] conducted bending fatigue tests with CFRP and found a linear relationship between decrease in bending modulus and increase in electrical resistivity. Furthermore, several other researchers investigated the electrical resistance change method for monitoring damages in CFRP [13,14,17,18,103–107].

In contrast to the resistance measurement method, in the electrical potential method a constant current is always applied between two electrodes and the electrical potential is measured at two or more other points than on the electrodes, where the current is injected. This method has been investigated by several groups [108–111]. Special forms of the potential method are EIT

and electrical resistivity tomography (ERT) [112]. EIT and ERT are imaging techniques that reconstruct the spatial distribution of electrical conductivity by injecting electrical currents and measuring the voltage at a set of boundary electrodes. Schueler et al. [16] were the first to use EIT for damage mapping on CFRP. Recently, further EIT and ERT studies were conducted by Fan et al. [113] and other researchers [114–117].

2.3.3 Structural health monitoring of carbon nanotube modified polymers via electrical conductivity methods

The concept of exploiting the piezoresistive properties of carbon nanoparticle modified polymers for strain and damage monitoring by electrical resistance measurement was first introduced by Kupke et al. [17] and Muto et al. [22]. Fiedler et al. [23] were the first to suggest using carbon nanotubes to modify the polymer matrix for damage sensing. Later, several investigations proved the concept of nanoparticle modification and resistance measurement for strain and damage sensing [26–30,118]. Electrical conductivity-based structural health monitoring of nanoparticle modified composites can be divided into resistance change methods and electrical tomography methods.

Resistance change methods are used to detect and localize internal damages in composites with CNT or carbon black (CB) modified matrix by measuring the electrical resistance before and after damage and calculating the resistance change. Through-thickness and in-plane electrical resistance measurements with distributed line or point electrodes have shown promising results. Wicks et al. [119] presented a damage mapping technique for an aluminum oxide fiber/epoxy composite with CNT grown on the fibers. They applied a grid of lined silver electrodes onto both sides of the specimen and measured the resistance through the thickness and in-plane. Viets et al. [120] demonstrated the damage mapping of CNT modified GFRP using electrical resistance measurement. Naghashpour and Hoa [121] measured the resistance distribution of CNT modified GFRP via electrical resistance measurements at point electrodes distributed over the surface of composite

plates. Zhang et al. [122] introduced a new technique to monitor CB modified GFRP by using weighted changes of in-plane and through-thickness resistances before and after impact damage. Lately, Gungor and Bakis [123] used co-cured carbon fibers as lined electrodes to monitor indentation damage in CB modified GFRP by plotting the resistance change. In the above mentioned studies, in which resistance change methods were used, good correlation of impact and other damages with resistance change was found.

In recent years, EIT and ERT have been investigated for structural health monitoring applications for composite materials, particularly for nanocomposites, in several studies. Hou et al. [124] and Loh et al. [125] used EIT for conductivity mapping on CNT modified thin films applied to substrates and achieved good localization of multiple damages. Baltopoulous et al. [126] used this method to detect through-hole and indentation damages in CNT modified GFRP. An extension of EIT for using the technique on electrically orthotropic GFRP with embedded CNT modified films was presented by Loyola et al. [127,128]. Tallmann et al. [129–133] comprehensively investigated the application of EIT on carbon nanofiber modified polymers and CB as well as CNT modified GFRP. Furthermore, Gallo and Thostenson [134] used both EIT and the resistance change method to detect holes in CNT modified GFRP.

An advantage of ERT and EIT is that fewer electrodes are necessary on the structure subject to be monitored and the electrodes only need to be applied at the boundary. However, the computational effort is significantly lower for resistance change approaches and therefore a real-time monitoring is easier to achieve with this method. In addition, the resistance change method seems to be more suitable for detecting inter-laminar delaminations [122].

SHM of adhesively bonded composite joints has been studied using different methods, e.g. lamb waves [31], DIC [32], and FOS [33]. However, only few studies on structural health monitoring of adhesively bonded joints via electrical resistance measurements exist. Mactabi et al. [135] showed that the electrical resistance change can be used to monitor the integrity of a CNT modified adhesively bonded aluminum joint, and Lim et al. [136] demonstrated a detection of the damage initiation in adhesively bonded

hybrid composite/steel joints by using CNT networks. Zhao and Schagerl [137] used EIT to measure the strain distribution of a single lap joint with a thin inkjet-printed CNT film between adhesive and adherend. Kang et al. [138] and Kim et al. [139] showed that crack initiation and propagation can be detected by electrical resistance and impedance measurement in an adhesive joint with a CNT content of 2.0 wt.%. None of these investigations used adhesive films, as they are used for example in aircraft industry. Recently, Sánchez-Romate [140] spray applied CNT onto adhesive films and demonstrated damage sensing via electrical resistance measurement through the adhesive films in single lap shear and double cantilever beam tests. However, damage localization is not possible with this approach.

2.4 Printed electronics on composites

To employ the composite material itself as a sensor in an SHM system, electrodes need to be placed on the material. A reliable contacting of the material is crucial to enable electrical resistance measurement during operation. The application of electrodes and conductive paths can be achieved using common printing technologies. Inkjet printing is a promising technology for many industrial applications due to its simplicity, flexibility, and scalability at low cost [141]. The following two subsections describe an overview of state of the art printed electronics with both silver nanoparticle-based and carbon nanoparticle-based ink with emphasis on composite materials as substrates.

2.4.1 Printed electronics with silver nanoparticle-based ink

The requirements of metal-based inks for printed electronics are similar to standard inks with the addition that the printed structure needs to be highly electrically conductive. This makes highly electrical conductive metals such as silver ($6.3 \cdot 10^7$ S/m), copper ($5.8 \cdot 10^7$ S/m), gold ($4.1 \cdot 10^7$ S/m), and aluminum ($3.5 \cdot 10^7$ S/m) (values at 20 °C) [142] possible candidates. Most of the conductive inks are based on silver due to the highest electrical conductivity and its oxidation resistance. Aluminum and copper are cheaper than silver, but aluminum has the disadvantage of rapid oxidation. Copper is also prone to oxidation and especially for nanoparticle-based inks, the corrosive properties of the used metal are not negligible due to the large surface area [143,144]. After the printing process, other ink components form insulating layers between the metal particles. Therefore, usually a post-printing process (sintering) is required to obtain a continuous interconnected phase between the metal particles [143,145]. A small particle size allows a strong reduction of the melting point [146] and therefore a low sintering temperature is possible [147]. Low sintering temperatures for conductive paths allow to print electronics on heat sensitive substrates like flexible electronics on polymer foil [21]. When working with CFRP and silver inks, a low sintering temperature is also essential to avoid damaging the

material. Jeon et al. [148] successfully printed silver based electrodes on CFRP for damage sensing. Recently, Takahashi et al. [149] and Joo et al. [150] investigated the reduction of sintering time of metal-based nanoparticle ink on CFRP to apply electrodes for electrical resistance measurements by using flash light sintering, which speeds up the manufacturing process and makes the approach more attractive for industrial application.

2.4.2 Printed electronics with carbon nanoparticle-based ink

Compared to metal-based inks, carbon nanoparticle-based inks offer the advantages of low cost (when compared to silver and gold), no oxidation issues (as present for copper and aluminum), and no necessity of sintering. CNT and graphene are the most promising candidates as carbon nanoparticles to be used in inks. Inkjet printing of CNT based ink [151,152] and graphene based ink [153,154] have gained increasing interest over the last years. They offer high potential for several electronic applications including SHM for composite materials.

3 Materials

3.1 Carbon fiber reinforced polymer

The used carbon fiber reinforced prepregs *HexPly M21/34%/UD194/T800S* by Hexcel Corporation are designed for aerospace applications and consist of an epoxy matrix (M21) with toughening thermoplastic particles and carbon fibers (T800S). Each roving in the prepregs consist of 24000 carbon fibers (24K) with an average fiber diameter of 5 µm, intermediate tensile modulus (294 GPa), and high tensile strength (5.88 GPa). The nominal fiber mass per unit area is 194 g/m^2, the nominal resin content is 34 wt.%, the nominal cured ply thickness is 0.1875 mm, and the curing temperature is 180 °C.

3.2 Glass fiber reinforced polymer

The used GFRP *EP GC 308*, purchased from Arthur Krüger GmbH, consists of an epoxy matrix and biaxial oriented glass fibers. The nominal thickness of the laminate is 2 mm.

3.3 Glass fabric

The glass fabric, purchased from R&G Faserverbundwerkstoffe GmbH, consists of E-glass fibers arranged as twill weave with a low mass per unit area of 80 g/m^2.

3.4 Epoxy resins

For the masterbatch production for adhesive film manufacturing, the epoxy resin *Epon Resin 828* by Hexion Inc. was used. It is an undiluted liquid epoxy resin with relatively low viscosity.

For nanoparticle modified epoxy fibers, the resin *Epikote RIMR 135* by Momentive with the hardener *Epikure RIMH 134* by Momentive were used.

3.5 Carbon nanoparticles

The CNT used in this study for modification of adhesive films are SWCNT *Tuball (75 %)* by OCSiAl. The carbon content is > 85 % and the CNT content > 75 %. Diameter and length of the CNT are 1.8 ± 0.4 nm and > 5 µm, respectively.

For modification of epoxy fibers, in addition to CNT, carbon black (CB) *Printex 300* by Evonik industries AG and few layer graphene (FLG) *AvanGraphene-2* by Avanzare Innovacion Tecnologica, S.L. were used.

3.6 Silver based inks

Silver nanoparticle ink for inkjet printing was formulated at the Institute of Automation Technology (Helmut Schmidt University). Silver nanoparticles (31.0 wt.%) with a D90 value (90 % of the distribution lies below this value) of 60 nm are dispersed in the solvent butyl carbitol (68.5 wt.%) and ethyl cellulose (0.5 wt.%).

For manual application of silver electrodes as well as for contacting copper wires, conductive silver paint *Acheson Silver DAG 1415M*, purchased by Plano GmbH, was used. It consists of 57.5 – 59.0 wt.% silver and a thermoplastic resin as binder.

4 Structural health monitoring of CFRP via electrical resistance measurement

In this chapter, investigations to use inkjet-printed conductive paths on CFRP to detect and localize damages in the material are presented. In addition to printing onto the cured CFRP surfaces, printing directly onto the prepregs to obtain conductive paths integrated into the laminate below the surface is investigated. This approach offers the advantage that the sintering process can be integrated into the curing process (i.e. the autoclave process) and no additional sintering step is necessary. A challenge for achieving integrated paths is the low viscosity of the resin during an autoclave process that could lead to insufficient quality of the printed paths after curing.

Three-point bending tests with simultaneous electrical resistance measurements are carried out. As non-destructive testing methods, X-ray and ultrasonic testing are used for a parallel detection and localization of the damages. From the experimental results, an analytical model is derived describing the electrical resistance change due to IFF and delaminations under three-point bending. Furthermore, impact tests are conducted on CFRP specimens and the electrical resistance change caused by the impact damage is investigated.

This work aims to demonstrate the damage sensing potential of an electrode system, which is directly printed onto the cured CFRP surface and on prepregs with focus on the detection and localization of IFF and delaminations.

4.1 Specimen preparation

4.1.1 Three-point bending test specimens

Conductive paths printed onto surface of cured CFRP

CFRP plates with the two different laminate layups, $[90_3/0_2]_S$ and $[90_3/+45/-45]_S$, were laminated from the prepregs and cured in an autoclave process at a temperature of 180 °C and a pressure of 7 bar for 120 min in a nitrogen atmosphere. The laminate layups were chosen to introduce IFF on the bottom side of the specimens and delaminations on top of the lower three 90°-layers under bending conditions. Subsequently, specimens with dimensions of 100 mm x 15 mm x 1.9 mm (in accordance with DIN EN ISO 14125) were cut from the plates using a water-lubricated diamond saw. Additionally, for electrical characterization of the CFRP, a UD laminate with the laminate layup $[0]_{10}$ was manufactured using the described autoclave process. From this plate specimens with dimensions of 15 mm x 15 mm x 1.9 mm were cut.

Functional silver-ink was printed on the CFRP surface to obtain conductive paths. No surface treatment was carried out prior to printing to keep the amount of manufacturing steps as low as possible. The surfaces were cleaned using isopropyl alcohol. The used single nozzle print head (by microdrop Technologies) has a nozzle diameter of 70 µm. A piezo actuator controls the emission of single drops. The voltage and the current pulse applied to the piezo actuator as well as the nozzle temperature can be varied to obtain an optimal drop. The control software and the moveable table, where the substrate is placed, allow for printing images on the CFRP. This system forms a reliable and reproducible drop with the ink as described above. A sintering temperature of 170 °C was applied for 4 h to obtain conductive silver paths. Figure 4.1 (a) shows the printing setup used. The printed conductive paths on the CFRP using this setup are shown in Figure 4.1 (b) and (c) in different magnifications.

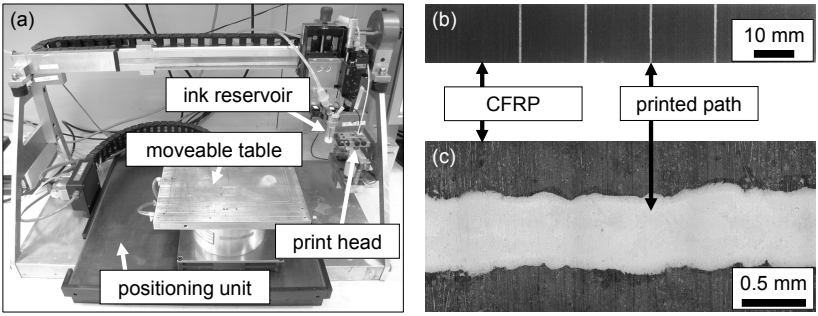

Figure 4.1: (a) Inkjet printing setup; (b) Image of specimen with four printed conductive paths; (c) Light microscopy observation of printed path prior mechanical testing.

To enable reliable contacting with the system for resistance measurements, stranded copper wires were connected with the printed conductive paths using conductive silver paint. Silver paint was also applied on the edges of the specimens that were used for electrical characterization. After this preparation, the specimens were dried for 5 h at 40 °C in a vacuum oven and stored in a desiccator until testing to keep the specimen conditions constant.

Integrated conductive paths printed onto prepregs before curing

In addition to specimens with conductive paths printed onto the cured CFRP surface, as described above, specimens with conductive paths integrated into the laminate below the surface were manufactured.

Therefore, prepregs were stacked to the laminate layup $[90_2/0_2]_S$ and vacuum-bag consolidated for 5 min to reduce the roughness of the outer layers for the printing process. This causes a surface that is smooth enough for the inkjet printing process. Then, the conductive paths were printed onto the outer prepreg layers. Onto both sides, another prepreg layer was added over the printed paths obtaining the laminate layup $[90_3/0_2]_S$. Subsequently, the autoclave process was conducted as described above. The sintering of the silver nanoparticles was integrated into the autoclave process and no additional sintering process was necessary. After curing, the three-point bending test specimens were cut from the plates, the conductive paths were

connected with copper wires, and the specimens were dried as described above.

4.1.2 Impact test specimens

CFRP plates with the laminate layup $[45/90/-45/0]_{3S}$ were laminated from the prepregs and cured in an autoclave process (see 4.1.1). Specimens with dimensions of 150 mm x 100 mm x 4.5 mm were cut from the plates using a circular saw with a diamond saw blade. Silver paint was applied on the surfaces of the specimens in form of 16 equidistantly distributed circles (distance of midpoints: 25 mm) with a diameter of 5.5 mm. Stranded copper wires were connected with these circles by using conductive silver paint (see Figure 4.2).

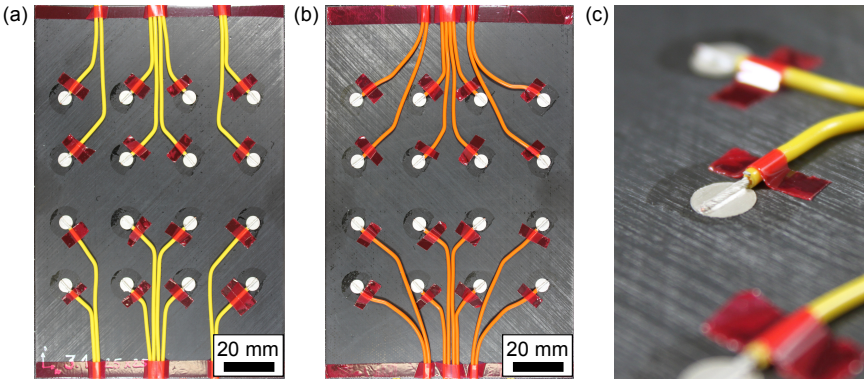

Figure 4.2: Impact test specimens; (a) Top side with 16 point contacts; (b) Bottom side with 16 point contacts; (c) Detail of circular electrode with connected copper wire.

4.1.3 Omega stringer/skin demonstrator for impact tests

In addition to the plate specimens described above, a structural CFRP part with geometry and layup close to stiffening elements widely used in fuselages of modern aircrafts is investigated. The demonstrator consists of

an omega stringer adhesively bonded onto a skin. Therefore, a stringer with the laminate layup [45/-45/0_2/90/0_2/-45/45] and dimensions of 130 mm (width) x 200 mm (length) x 30 mm (height) was laminated onto a metallic tool that was coated with release agent. Then, a vacuum bag was placed over the layup and attached to the tool. Curing was conducted in an oven at 180 °C for 120 min.

Conductive paths out of silver nanoparticle–based ink were inkjet-printed onto both sides of the stringer (see Figure 4.3). Copper wires were connected to the outer ends of the printed conductive paths using conductive silver paint.

The skin was manufactured from prepregs with a multidirectional laminate layup. Before the autoclave process, a thin glass fiber fabric was placed onto the surfaces of the laminated prepregs to act as an outer, electrically insulating layer. After the subsequent autoclave process, the skin was cut to dimensions of 240 mm x 170 mm x 3 mm.

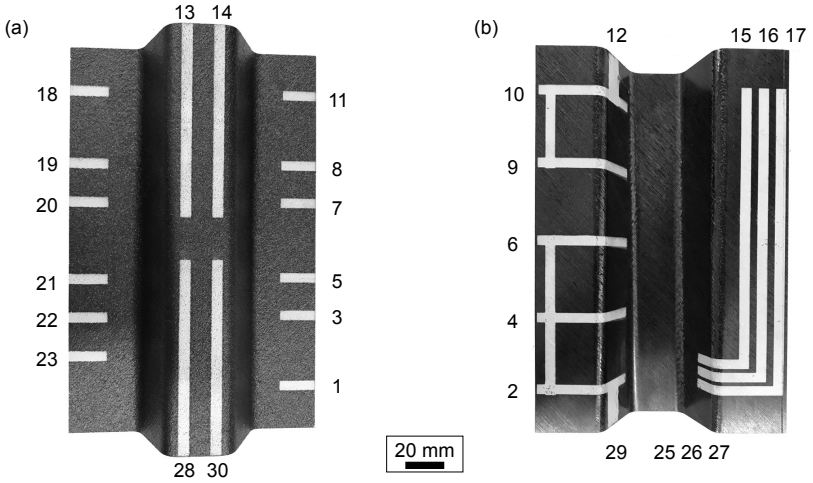

Figure 4.3: Omega stringer with inkjet-printed conductive paths; (a) Top side; (b) Bottom side; Contacts used for the electrical measurements are numbered.

To achieve a good adhesion between stringer and skin, the surfaces to be bonded were activated by a low-pressure plasma treatment (SmartPlasma 10 by Plasmatechnology) with a power of 300 W at a pressure of 0.3 mbar for 60 s. Then, an epoxy-based adhesive film without nanoparticle modification was placed between stringer and skin. A vacuum bag was placed over this layup and curing of the adhesive film took place at 120 °C for 120 min in an oven. As a last step, the copper wires were fixed with adhesive tape to avoid rupture at the connection points. Figure 4.4 shows the manufactured part.

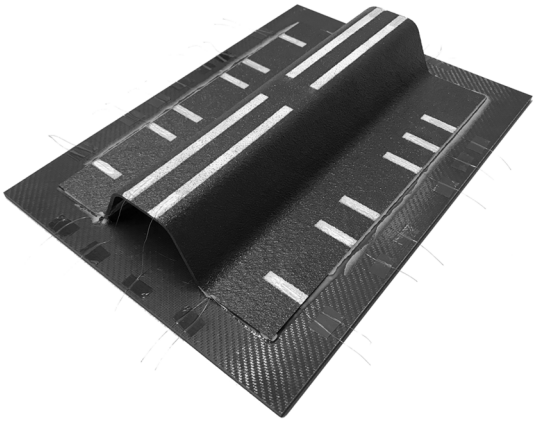

Figure 4.4: Omega stringer with printed conductive silver paths adhesively bonded on a skin.

4.2 Experimental

4.2.1 Electrical characterization

Four channel measurements were carried out to determine the conductivity of the UD CFRP specimens in three directions by using a digital multimeter (Keithley 2601A). Ten specimens were tested in the following three directions, respectively:

- In fiber direction (0°-direction)
- Perpendicular to fiber direction, in plane (90°-direction)
- Perpendicular to fiber direction, out of plane (thickness direction)

On each specimen, one continuous electrical measurement was carried out. From the resistance (R), the measuring length (l), and the cross section (A), the conductivity (σ) is calculated as follows:

$$\sigma = \frac{l}{R \cdot A} \tag{4.1}$$

Additionally, the conductivity of the printed silver nanoparticle-based paths was measured for comparison of the conductivity of path and CFRP substrate. Therefore, five specimens with insulating surfaces were investigated. On each specimen, one path with a length of 38.2 mm, a width of 0.67 mm, and a thickness of 7 µm was printed. Sintering of the conductive paths was conducted before electrical measurements. On each specimen, one continuous electrical measurement was carried out by connecting the digital multimeter (Keithley 2601A) with the ends of the conductive paths.

4.2.2 Three-point bending tests

Three-point bending tests were conducted using a universal testing machine (Zwick Z2.5 TH) to achieve high tensile loads in the lower 90°-layers and

systematically introduce IFF on the bottom side of the specimens and delaminations above the lower 90°-layers. The test speed was set to 2 mm/min to generate a sufficient time interval between the individual failures to detect the failures separately. Both loading pin and supporting pins (further denoted as cylinders) of the three-point bending test setup consist of aluminum oxide (Al_2O_3) to ensure electric insulation of the specimens during testing. The distance between the lower cylinders was 55 mm and the diameters were 10 mm and 4 mm for the upper and lower cylinders, respectively.

Different test series were conducted and are described in the following. In the first test setup, conductive paths are printed parallel to the 100 mm long edges and the resistance is measured along these paths to investigate the change of resistance along the paths exposed to bending. In addition, tests with printed paths on both sides of the specimens are executed and the resistance is measured through the material during mechanical testing.

Electrical resistance measurements along printed paths

The specimen geometry and the locations of the conductive paths are shown in Figure 4.5 (a). Two paths are printed on the bottom side of the specimen. This design was chosen to be able to compare two measured signals from two paths lying next to each other. To measure the direct current (DC) resistance over the length of the conductive paths the ends of the paths are connected with a digital multimeter (Keithley 2000). Figure 4.5 (b) shows a schematic of the test setup.

Electrical resistance measurements through material

To be able to measure the resistance through the material, specimens with printed paths on both sides are produced. The design of the conductive paths for measuring through the material is shown in Figure 4.6 (a). The DC resistance is measured from the top electrode to each of the four electrodes on the bottom side of the specimen. Figure 4.6 (b) shows the test setup and the connected electrodes for the four measured resistances.

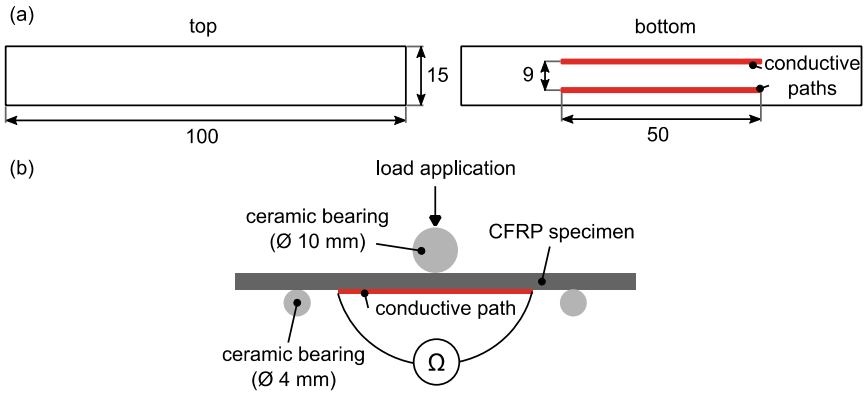

Figure 4.5: (a) Specimen geometry, design of conductive paths for measuring resistance along printed paths; (b) Three-point bending test setup with electrical resistance measurement along printed paths.

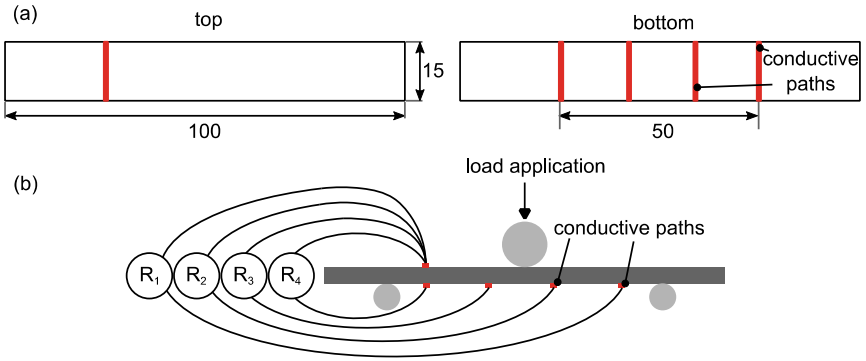

Figure 4.6: (a) Specimen geometry, design of conductive paths for measuring resistance through material; (b) Three-point bending test setup with electrical resistance measurement through material.

Electrical resistance measurements with integrated conductive paths

In addition to the test series described above, specimens with conductive paths integrated in the laminate were tested. The conducive paths were placed below the outer ply in the laminate and the specimen geometry was unchanged. However, to enable a contacting of the printed paths, the conductive paths were longer and the sizes of the outer plies were reduced. Figure 4.7 shows the specimen design with the integrated conductive paths.

To investigate the structure of the embedded conductive paths, light microscopy observations on polished sections were made.

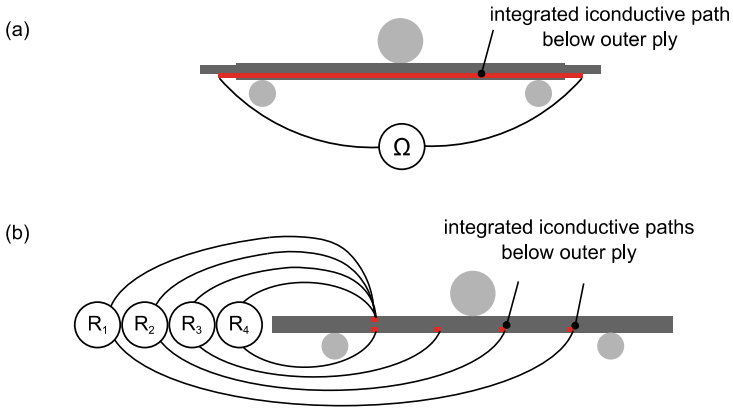

Figure 4.7: Design of integrated conductive paths; (a) Measurement along printed path; (b) Measurement through material.

4.2.3 Impact tests on plate specimens

Electrical resistance measurements were conducted using a digital LCR meter (Peaktech 2170). The resistances of all possible electrode combinations were measured for the through-thickness measurements. In-plane measurements were conducted by measuring the resistance of the adjacent electrodes in both x–y planes in which the electrodes are located. Impacts were introduced using a drop weight impact test according to

ASTM D7136-05 [155]. Four clamps fix the specimen as shown in Figure 4.8. A hemispherical hardened steel impactor with a weight of 1.96 kg was dropped from a height of 1040 mm above the center of the specimen resulting in a potential energy of 20 J. This energy corresponds to an energy-to-thickness ratio of 4.4 J/mm. To obtain the contact force during the impact event, the head of the impactor is equipped with a strain gauge full bridge. An antirebound system prevents multiple impacts during testing.

After the impact event, the resistances of all electrode pairs were measured again for investigation of the resistance changes due to the impact damage.

To evaluate location and size of the impact damages, ultrasonic measurements were carried out (USPC 3040; Ingenieurbüro Dr. Hillger). Pulse-echo method was used and demineralized water served as coupling medium.

For evaluation of the measured resistances, according to Zhang et al. [122], heat maps can be obtained by calculating a damage index P(x,y), which interpolates over the area of in-plane measurements.

To be able to apply this evaluation method to both in-plane and through-thickness measurements, the two-dimensional equations are expanded to

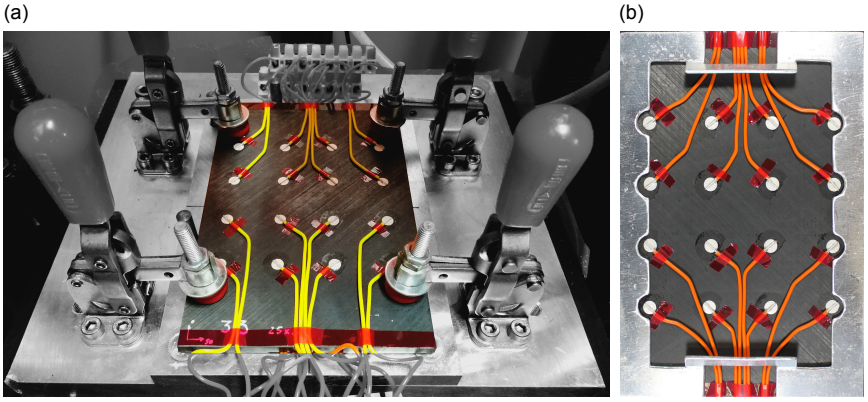

Figure 4.8: Impact test setup; (a) Specimen fixed for impact introduction; (b) Specimen on support with cable openings on both sides.

three dimensions, resulting in the following equations. Furthermore, some adaptions of the method are made. P(x,y,z) is the accumulated weighted electrical resistance change at the position (x,y,z).

$$P(x,y,z) = \frac{\sum_{k=1}^{N} P_k(x,y,z)}{M} = \frac{\sum_{k=1}^{N} \delta_k \cdot W_k[R_k(x,y,z)]}{M} \tag{4.2}$$

Where the index k refers to the specific measuring path, which is defined as straight line between two electrodes. N is the number of measuring paths and M is the number of measuring paths that are considered for the location (x,y,z). M is introduced to avoid an accumulation of the resistance changes leading to overweighted resistance changes at locations with a high number of measuring paths, as this is the case for the method presented by Zhang et al. [122]. The change of the electrical resistance δ_k is $\Delta R_k/R_{0,k}$. The parameter $R_k(x,y,z)$ is defined as the relative distance from the location (x,y,z) to the k^{th} measuring path.

$$R_k(x,y,z) = D_{a,k}(x,y) + D_{s,k}(x,y) - D_k \tag{4.3}$$

Where D_k is the distance of the k^{th} measuring path, and $D_{a,k}(x,y,z)$ and $D_{s,k}(x,y,z)$ are the distances between the location (x,y,z) and the beginning and the end of the k^{th} measuring path, respectively.

W_k is a step function that considers only resistance changes of measuring paths that lie within a defined relative distance from the location (x,y,z).

$$W_k[R_k(x,y,z)] = \begin{cases} 1 & for\ R_k(x,y) < \beta \\ 0 & for\ R_k(x,y) \geq \beta \end{cases} \tag{4.4}$$

To define suitable zones of influence, the scaling factor β was set to 3 mm. For smaller values, no significant increase in the resolution was seen. Points of a pattern of 5 mm x 5 mm were chosen as locations to calculate P(x,y,z).

4.2.4 Impact tests on omega stringer/skin demonstrator

Impact damages were introduced at three different locations of the stringer. Two foot impacts (left and right) were applied onto the adhesively bonded areas and one head impact was applied in the middle regarding the width of the omega stringer. Electrical resistances of all possible combinations of electrode pairs were measured before and after the impact event.

To conduct these electrical resistance measurements, a device that is able to measure the electrical resistance of all possible combinations of up to 32 channels with multiplexing capabilities was designed and produced by the Forschungswerkstatt Elektrotechnik at Hamburg University of Technology. The measuring device was connected to a computer to allow for defining the channels to be measured. Twenty-nine channels of the measuring device were connected with the copper wires that are connected to the omega stringer (see Figure 4.9).

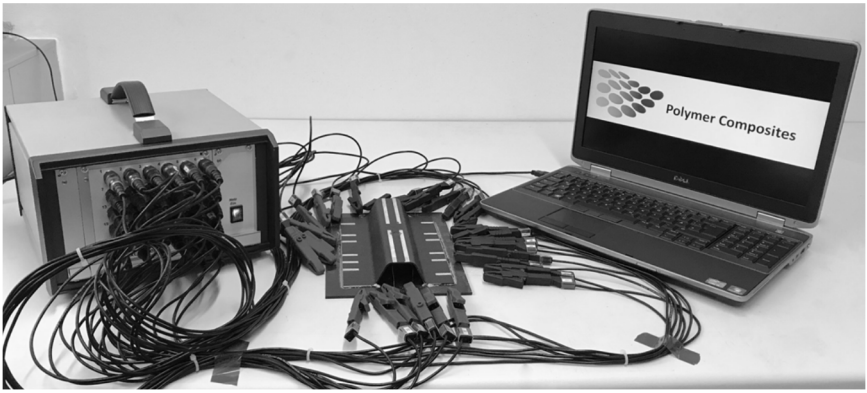

Figure 4.9: Setup for conducting electrical resistance measurements on an omega stringer using a resistance measurement device with multiplexing capability.

4.2.5 Nondestructive testing

Radiography was used for detection and localization of IFF in three-point bending test specimens (Faxitron Model 43855a). The tube current was 3 mA at 20 keV and the exposure time of the D2 films was 5 min. For better visibility of cracks, a zinc iodide-based contrast medium, consisting of ZnI_2, H_2O, isopropyl alcohol, and Agfa Agepon, was applied on the specimen edges prior to X-ray exposure. Development and fixing of the films was conducted using the manual developer Agfa Structurix G128 in conjunction with the fixer Agfa Structurix G328. Finally, the films were flushed in water for 10 min and dried in a drying chamber for 20 min.

To evaluate locations and size of the delaminations in impact test specimens and three-point bending test specimens at different load levels, ultrasonic measurements were carried out (USPC 3040; Ingenieurbüro Dr. Hillger). Pulse-echo method was used and demineralized water served as coupling medium. Selected specimens were tested at load levels with displacements from 0 mm up to 12.5 mm in displacement steps of 2.5 mm. Characterization of the delaminations were performed on the generated C-scans.

4.3 Results

The conductivity values of UD specimens are shown in Table 4.1. As expected, the highest conductivity is present in fiber direction and the conductivity perpendicular to the fiber direction in plane is higher than the conductivity perpendicular to the fiber direction in thickness direction (due to resin rich areas between the plies). The conductivity of a printed path is two orders of magnitude higher than the conductivity of the CFRP in fiber direction. This difference enables to measure changes of the current flow from the highly conductive paths to the lower conductive CFRP.

Electrical conductivity and in particular through-thickness electrical conductivity of CFRP varies extremely depending on fiber volume content and size of the inter-laminar polymer layers. Compared to the values presented here, much lower conductivities have been measured in some other studies [156,157]. In these studies, microscopy images show larger inter-laminar polymer layers than the light microscopy images of the investigated CFRP. However, there are also studies that report electrical conductivities in the same range [47] or even higher than the ones reported here, measured on comparable materials [12] even for interleaved systems [47].

Table 4.1: Electrical conductivities of unidirectional specimens, $[0]_{10}$, in three directions and printed silver nanoparticle-based sintered path on insulating substrate in S/m.

	Fiber direction	Transverse direction, in-plane	Through-thickness direction	Sintered silver nanoparticle ink
Mean value in S/m	$3.7 \cdot 10^3$	$1.5 \cdot 10^1$	$1.4 \cdot 10^0$	$4.9 \cdot 10^5$
Standard deviation in S/m	$0.4 \cdot 10^3$	$0.4 \cdot 10^1$	$0.4 \cdot 10^0$	$0.9 \cdot 10^5$

Data from literature and the measured values (see Table 4.1) for electrical conductivity of CFRP are summarized in Figure 4.10.

In the cross sectional view (see Figure 4.17) it can be seen that the inter-laminar polymer layers are relatively small and at some points touching fibers of adjacent layers can be observed. In combination with the high fiber volume content, this leads to a relatively high through-thickness conductivity, compared to laminates with larger inter-laminar polymer layers.

A comparison of the through-thickness conductivity of UD and quasi isotropic laminates supports this observation. The through-thickness conductivities of quasi isotropic laminates (laminate layup: $[45/0/-45/90]_S$) made from the same prepregs using the same amount of specimens were measured. An electrical conductivity in through-thickness direction of 3.3 ± 0.3 S/m is found, which is twice as high as the conductivity

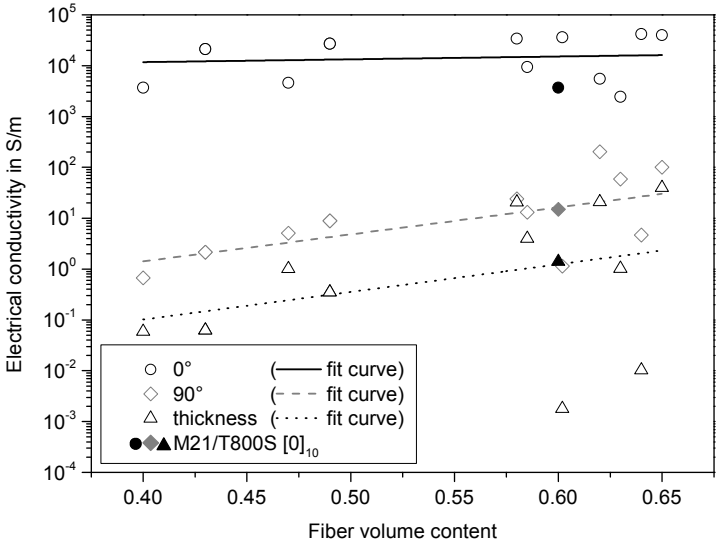

Figure 4.10: Comparative log plot of electrical conductivity versus respective fiber volume content of CFRP. Unfilled symbols correspond to literature data [12,46,47,156,158–160] and filled symbols correspond to measured values for M21/T800S (cf. Table 4.1).

measured on the UD specimens. The higher conductivity of the quasi isotropic laminates is present due to more connection points of touching fibers of adjacent layers compared to UD laminates. Other researchers have also observed this trend by comparing UD and multidirectional laminates [48].

4.3.1 Electrical resistance measurements along printed paths for surface crack detection

In this section, the results of the investigations on specimens with conductive paths that were printed onto the surface of cured CFRP are presented.

Figure 4.11 shows typical results of the mechanical and electrical measurements for a specimen with a layup of $[90_3/0_2]_S$. The resistance without loading (R_0) is 2.1 Ω for both conductive paths, and the resistance change (ΔR) is specified as the difference of the measured resistance without (R_0) and during loading (R).

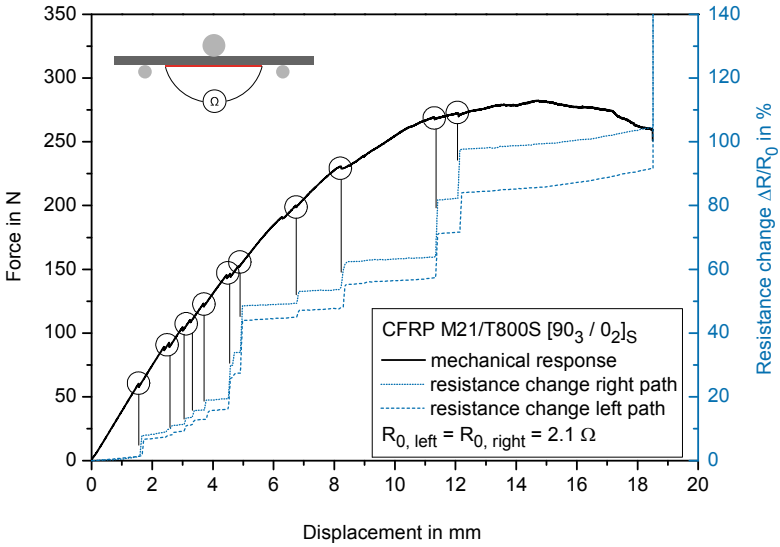

Figure 4.11: Force and resistance change of conductive paths versus displacement, $[90_3/0_2]_S$ laminate.

The force increases to a maximum at a displacement of 14.8 mm and fracture of the specimen occurs at 18.7 mm. In addition to the mechanical response, the change of electrical resistance is shown for the two conductive paths, measured from one end to the other of the same path, respectively. Both the force-displacement curve and the resistance change-displacement curves contain several discontinuities indicated by circles in the diagram. The discontinuities correlate perfectly with the steps in the resistance change.

The discontinuities in the measured force are attributed to damages in the material. Since the dominating failure modes in cross-ply laminates subjected to bending and the failures observed in the tested specimens are IFF and delamination, these two failure modes lead to the discontinuities of the measured force and resistance signals. All failures detected by the measured force, exceeding a certain amount of energy release, can be detected by resistance changes. X-ray images show that all discontinuities in the mechanical response correlate to IFF and the developing delaminations show no distinct discontinuities. The resistance increase at the end of the test (up to unmeasurable values) indicates the final fracture of the specimen cutting the specimen completely and therefore all possible conductive paths for current flow. Thus, all failures exceeding a certain size and therefore being relevant for the integrity of the specimen as well as the final fracture can be detected reliably.

Light microscopy observations of the damaged printed paths show that IFF at the surface cause interruptions as well as flaking of the paths in proximity to the cracks (see Figure 4.12). Hence, the resistance increases when IFF occur due to the interruption of the paths in the region of the cracks at the surface. The current flow in case of IFF flows through the CFRP, which has a higher resistance compared to the silver-based printed path, resulting in a resistance increase. The current flow is schematically shown in Figure 4.13.

This method enables to detect IFF reliably on the surface. It can be used to monitor surfaces where surface cracks are crucial. Damages of the paths occurred only due to events of IFF. Debonding of the CFRP-silver interface could not be observed. Therefore, the quality of the interface is sufficient for the considered application even without additional surface treatment.

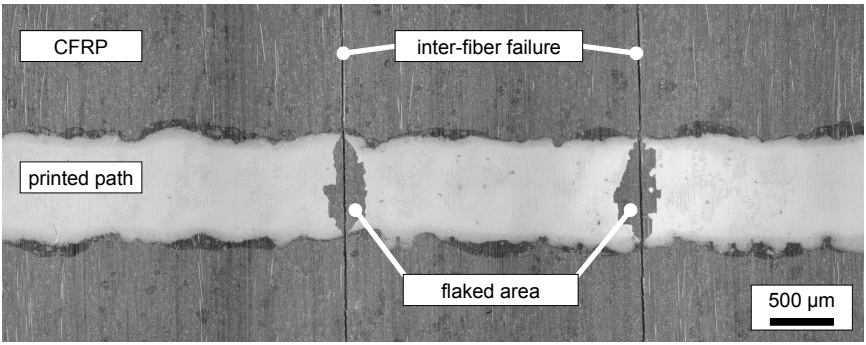

Figure 4.12: Light microscopy observation of printed path after testing.

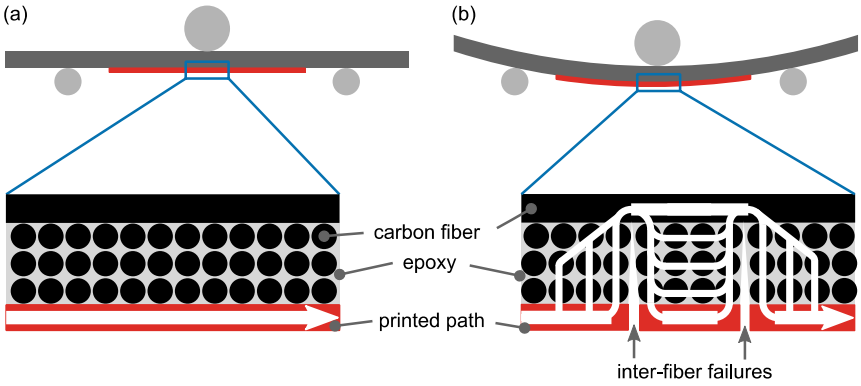

Figure 4.13: Schematic of current flow (white arrows, simplified); (a) Through undamaged printed path; (b) Through damaged printed path and composite material in case of inter-fiber failures.

The 0°-fibers in the cross-ply laminate have a significant influence on the mechanical as well as on the electrical behavior.

Therefore, a substitution of the 0°-layers with ±45°-layers was conducted and the results are shown in Figure 4.14. Due to the different layup, the maximum force and the Young's modulus are reduced and less IFF occur. The resistance change is similar compared with the resistance change of the cross-ply laminate, shown in Figure 4.11.

It can be said that with the substituted middle layers, surface cracks can be detected reliably as well. Therefore, a detection of all IFF is possible for both 0°-layers and ±45°-layers as middle layers of the laminate.

For both laminates, the resistance increase varies significantly for differently located IFF. Therefore, specimens are tested and unloaded at every IFF event and X-ray images are made to correlate the damage location with the resistance increase that the damage causes (see Figure 4.15). At the first damage event, two IFF occur and the resistance increases 4.1 %. For the third IFF the resistance increases clearly as well. The next two IFF, which are present in between two existing IFF (test steps 3 and 4), show only small increase in resistance. The last IFF does not lie in between two IFF and leads to a significant increase of the resistance again.

IFF that lie in between two other IFF lead to a smaller resistance increase compared to the IFF that do not lie in between two other IFF. Failures in between two other failures do not change the current flow as much as failures outside of other failures, since the path of least resistance is not changed in the case of a new crack in between two other cracks.

Hence, a reliable detection of IFF with the presented approach is possible. However, a localization of the damage is only possible if multiple paths with different electrode locations are used.

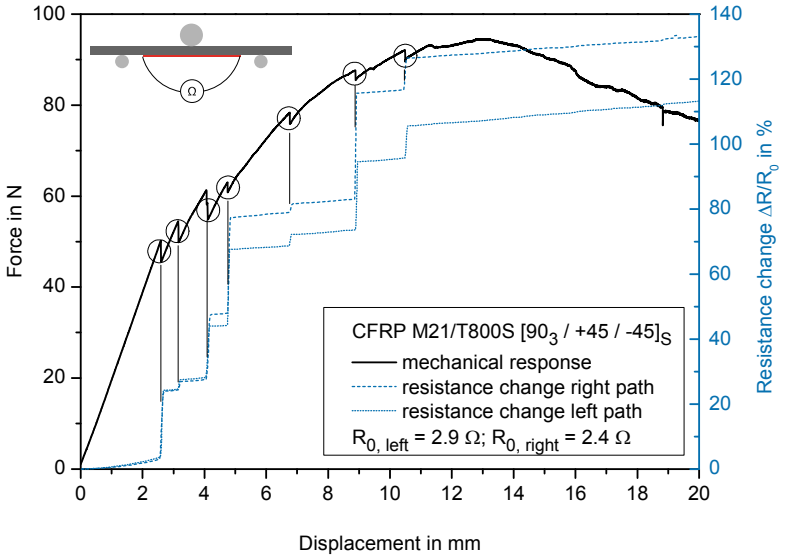

Figure 4.14: Force and resistance change of conductive paths versus displacement, $[90_3/+45/-45]_S$ laminate.

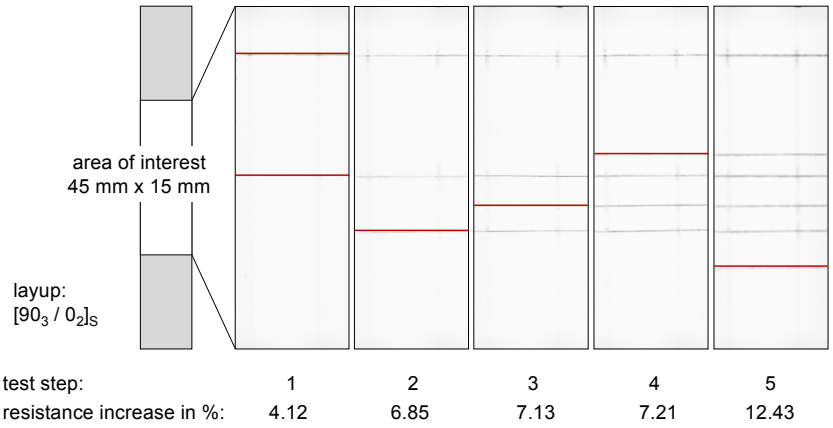

Figure 4.15: X-ray images of loaded specimen showing the development of inter-fiber failures and the according measured resistance increase.

4.3.2 Electrical measurements through the material for delamination detection

Mechanical and electrical measurements for a representative specimen are plotted in Figure 4.16. The mechanical response is qualitatively the same as in Figure 4.11. The resistance changes are different for the four measured channels. For channel 1 (from top electrode to bottom electrode 1) and channel 4 (from top electrode to bottom electrode 4) the relative resistance change is in the range of ±2.5 % until final fracture, where the resistances suddenly increase to infinity. The resistance change of channels 2 and 3 (from top electrode to bottom middle electrodes) increases significantly with increasing displacement up to 26 % and 17.5 % before final failure, respectively.

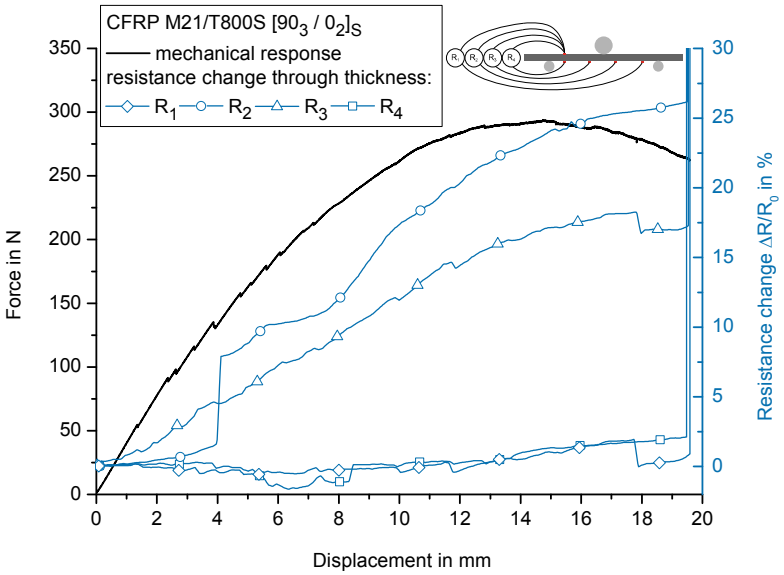

Figure 4.16: Force and resistance change of the four measured channels versus displacement.

The non-significant resistance changes of channel 1 and 4 (to electrodes left and right of the specimens) indicate that the current flow is not changed significantly in these areas of the specimen. It is assumed that close to these electrodes no delaminations and IFF that interrupt the current flow are present. For channel 2 and 3 the resistance increase indicates that damages occur inside of the material close to the most stressed areas in the center of the specimen. This can be proven by light microscopy observations of a tested specimen shown in Figure 4.17. Above electrodes 2 and 3 (center electrodes), IFF in the three lower 90°-layers and delaminations in between the 0°- and 90°-layer are found. Above the outer electrodes (1 and 4) only IFF are detected by light microscopy.

The comparison of the regions close to the outer electrodes and close to the inner electrodes shows that the only difference is the presence of delaminations in the higher loaded (center) area. IFF in the 90°-layers are present in all areas. Since the resistance change increases only for measurements with electrodes close to the most loaded areas where delaminations occur, delaminations can be detected by a significantly higher resistance change compared to areas where only IFF occur, which are not detected by the through-thickness measurements.

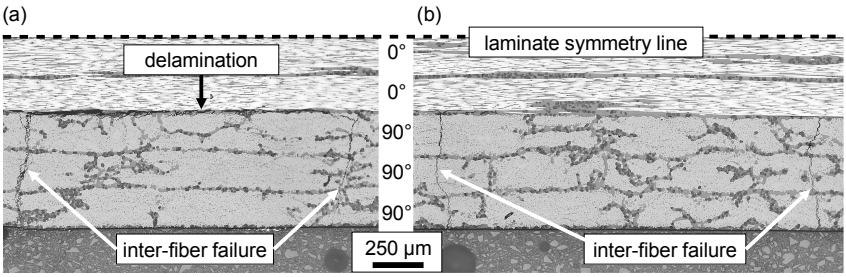

Figure 4.17: Light microscopy observation of polished sections after testing; (a) Region above electrodes 2 and 3 (middle electrodes), inter-fiber failures and delaminations; (b) Region above electrodes 1 and 4 (outer electrodes), only inter-fiber failures.

C-scans from ultrasonic testing show the development of delaminations (see Figure 4.18). No delaminations are present at 2.5 mm displacement. First delaminations are detected at 5.0 mm displacement. Between these two loading steps the resistance, measured to the middle electrodes, increases significantly. Hence, a detection of the first delaminations by resistance measurements is possible. With increasing displacement both the delaminations and the resistance for the electrodes close to delaminations increase. Furthermore, the delaminations appear in a depth of about 1.3 mm, which is the location of the lower 0°/90°-interface, since the cured ply thickness is 0.19 mm, resulting in a depth of the interface of 1.3 mm. This delamination area corresponds to the location of the delaminations found in light microscopy observation (see Figure 4.17).

Hence, detection as well as a localization of delaminations is possible with the used path design and through-thickness resistance measurement, because delaminations lead to a resistance increase at delamination areas in thickness direction.

Considering this high potential of printed conductive paths onto the surface of CFRP for structural health monitoring applications, it is also of interest whether damage detection is possible for conductive paths that are

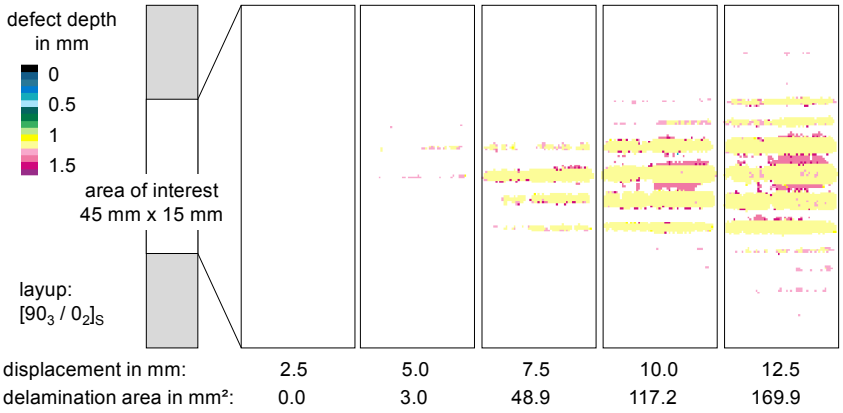

Figure 4.18: Ultrasonic C-scans with depth information for different displacement steps in three-point bending test showing delaminations.

integrated inside of the laminate between adjacent plies. The following section describes the results for integrated conductive paths.

4.3.3 Electrical measurements on specimens with conductive paths integrated inside of the laminate

For the electrical resistance measurements along printed paths (see Figure 4.7, (a)), no correlation of damages and resistance increase is present. During the three-point bending test, no distinct resistance increases are observed. Hence, a damage detection is not possible with these integrated paths.

However, for the electrical resistance measurements through the material (see Figure 4.7, (b)), the resistance change of the four measured channels exhibits a similar behavior compared to the same test setup with the conductive paths printed onto the surface (cf. Figure 4.6). Figure 4.19 shows representative results of this test.

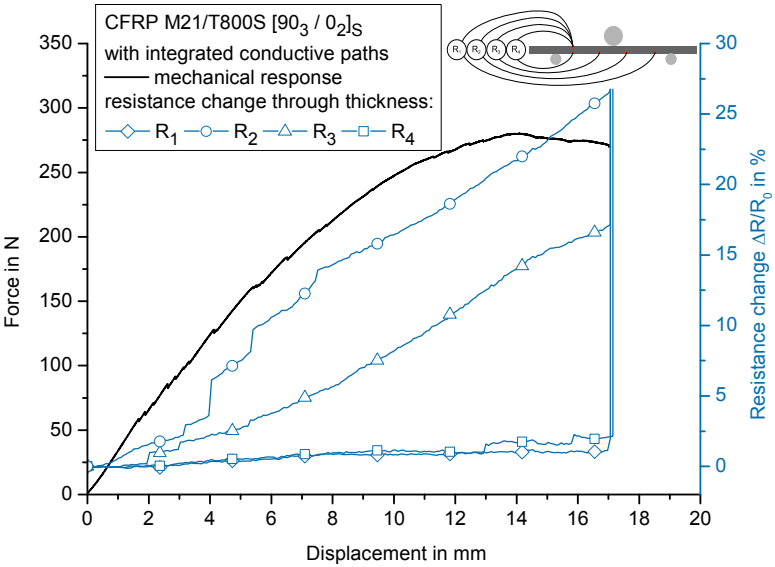

Figure 4.19: Force and resistance change of the four measured channels versus displacement on specimen with integrated conductive paths.

As observed before for the specimens with the printed path on the surface of the material, here similarly the resistances of channels 2 and 3 increase and the resistances of channels 1 and 4 do not show significant changes during the test. Therefore, for this integrated conductive path design the damage detection is possible in the same way as with conductive paths on the surface.

Light microscopy images of polished sections show the structure of the integrated paths. Paths that lie in fiber direction of the two adjacent plies are straight and continuous (see Figure 4.20 (a)), whereas paths that are oriented orthogonal to the fiber direction of the two adjacent plies are undulated and contain several discontinuities (see Figure 4.20 (b), (c), (d)). The waviness of these non-continuous paths adapts to the rovings of the two adjacent plies. Furthermore, most of the discontinuities lie in proximity to resin rich areas. During the heating up within the autoclave process, the resin reaches a very low viscosity. This could lead to relocations of the non-sintered silver nanoparticles leading to the observed discontinuities of the paths. This assumption is also supported by the fact that most of the discontinuities are located near resin rich areas.

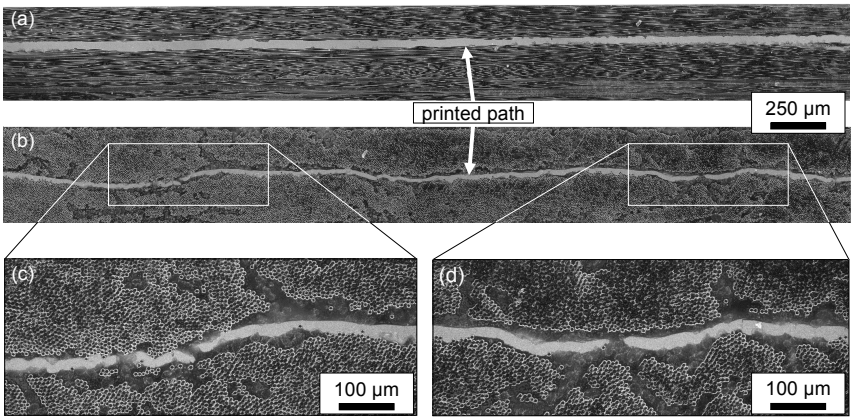

Figure 4.20: Light microscopy observation (dark field) of polished sections of printed paths integrated in CFRP laminate below top layer; (a) Path and fibers of adjacent plies are oriented parallel; (b) Path and fibers of adjacent plies are oriented orthogonal; (c), (d) Details of regions with undulated, noncontinuous conductive path.

Comparing the results of light microscopy observation and three-point bending tests with simultaneous electrical resistance measurements, a damage detection via electrical resistance measurement is possible with continuous integrated paths that are oriented parallel to the fiber direction of the adjacent layers. However, if discontinuities that occur for paths printed orthogonal to the fiber direction of the adjacent layers are present, reliable damage detection is not possible. Therefore, the fiber direction needs to be taken into account if printed paths are applied onto prepregs to achieve integrated conductive paths.

4.3.4 Analytical model

To gain a deeper understanding of the influence of IFF and delaminations on the electrical resistance change of CFRP, an analytical model is proposed in the following.

The analytical model is developed to be able to predict the electrical resistance change for defined loading and corresponding damage states of a CFRP specimen with printed conductive paths (configuration shown in Figure 4.5). With the model, an identification of the contributions to the electrical resistance change of both IFF and delaminations shall be possible. Furthermore, with such a model, the electrical resistance changes can be calculated for different laminate layups and electrical conductivity values and therefore also for other material systems.

Considering the anisotropic electrical resistances of the system, an equivalent circuit diagram is developed for the CFRP specimen (see Figure 4.21). The total resistance is measured from one to the other end of the printed path. It comprises the electrical resistance of the printed path (R_P), the contact resistance between printed path and CFRP (R_C), the resistance in thickness direction for each layer (R_t), and the 0°-layers and 90°-layers resistances in path direction for each layer (R_0 and R_{90}). The model is based on the assumption that damages reduce the effective area that can be used for electron transport, leading to a local increase of the electrical resistance.

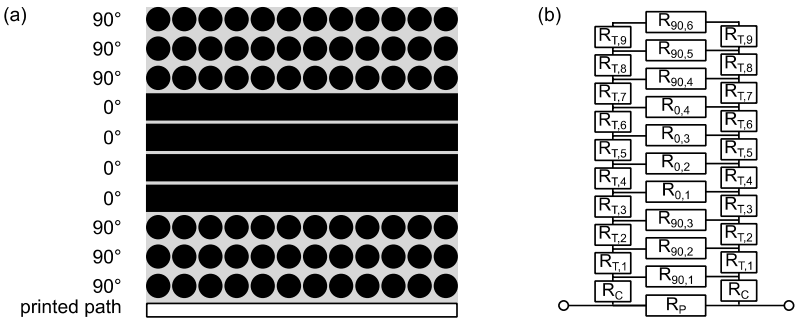

Figure 4.21: (a) Layup of the CFRP laminate with printed conductive path; (b) Equivalent circuit diagram of the system.

For this model, the following assumptions and simplifications are made:

- The material exhibits ohmic behavior. Hence, Ohm's law applies.
- Electrical current density is homogeneously distributed in all cross sections.
- Electrical resistance is the same for all layers of the same fiber direction and same damage state (i.e. $R_0 = R_{0,1} = R_{0,2} = R_{0,3} = R_{0,4}$ and $R_{90,lower} = R_{90,1} = R_{90,2} = R_{90,3}$ and $R_{90,upper} = R_{90,4} = R_{90,5} = R_{90,6}$).
- Electrical resistance in thickness direction between two adjacent plies is the same, independent of the fiber directions of the two neighboring layers, but it decreases for damaged layers (i.e. $R_{t,lower} = R_{t,1} = R_{t,2} = R_{t,3}$ and $R_t = R_{t,4} = R_{t,5} = R_{t,6} = R_{t,7} = R_{t,8} = R_{t,9}$).
- The contact resistance between printed path and the neighboring layer is half of the resistance as the one between two neighboring layers, because the resin rich inter-laminar layer between path and surface is half the size compared to the inter-laminar layer between two adjacent layers.
- In a first step, we consider the influence of IFF only. Therefore, we assume that after the first IFF, the effective areas of the printed path and of the lower 90°-layers are zero because the IFF interrupt these paths permitting electron transport (i.e. R_P = inf and $R_{90,lower}$ = inf).
- Every IFF reduces the effective area of the three lower 90°-layers by a fixed number p in %.

With the experimentally determined dimensions of a printed path, the effective area of the printed path can be expressed as

$$A_p = \begin{cases} 700 \cdot 10^{-6}\ m \cdot 8 \cdot 10^{-6}\ m & for \quad i = 0 \\ 0 & \quad\ i > 0 \end{cases} \tag{4.5}$$

Where i is the number of IFF.

The effective areas in thickness direction are

$$A_{t,1} = A_{t,2} = A_{t,3} = \begin{cases} 15 \cdot 10^{-3}\ m \cdot 50 \cdot 10^{-3}\ m & i = 0 \\ 15 \cdot 10^{-3}\ m \cdot 50 \cdot 10^{-3}\ m \cdot \frac{100 - p \cdot (i-1)}{100} & for \quad i > 0 \end{cases} \tag{4.6}$$

$$A_{t,4} = A_{t,5} = A_{t,6} = A_{t,7} = A_{t,8} = A_{t,9} = 15 \cdot 10^{-3}\ m \cdot 50 \cdot 10^{-3}\ m \tag{4.7}$$

Moreover, in the 90°- and 0°-layers, the effective areas can be expressed as

$$A_{90,1} = A_{90,2} = A_{90,3} = \begin{cases} 0.1875 \cdot 10^{-3}\ m \cdot 15 \cdot 10^{-3}\ m & for \quad i = 0 \\ 0 & \quad\ i > 0 \end{cases} \tag{4.8}$$

$$A_{0,1} = A_{0,2} = A_{0,3} = A_{0,4} = A_{90,4} = A_{90,5} = A_{90,6} = 0.1875 \cdot 10^{-3}\ m \cdot 15 \cdot 10^{-3}\ m \tag{4.9}$$

The lengths for calculating the resistances are taken from the specimen geometry:

$$l_P = l_{90} = l_0 = 50 \cdot 10^{-3}\ m \tag{4.10}$$

$$l_t = 0.1875 \cdot 10^{-3}\ m \tag{4.11}$$

Conductivity values σ_P, σ_t, σ_{90}, and σ_0 are taken from electrical resistance measurements (see Table 4.1). With these values, the resistances of all elements depicted in Figure 4.21 (b) are calculated using Ohm’s law:

$$R_m = \frac{l_m}{\sigma_m \cdot A_m}\ with\, m = P, t, 90, 0 \tag{4.12}$$

With the resistances and the equivalent circuit diagram, the total resistance R$_{\text{total}}$) for the initial state and for any number of IFF (i) can be expressed as:

$$R_{total} = \cfrac{1}{\cfrac{1}{R_p} + \cfrac{1}{2R_c + \cfrac{1}{\cfrac{1}{R_{90,1}} + \cfrac{1}{2R_{t,1} + \cfrac{1}{\cfrac{1}{R_{90,2}} + \cfrac{1}{2R_{t,2} + \cfrac{1}{\cfrac{1}{R_{90,3}} + \cfrac{1}{2R_{t,3} + \cfrac{1}{\cfrac{1}{R_{0,1}} + \cfrac{1}{2R_{t,4} + \cfrac{1}{\cfrac{1}{R_{0,2}} + \cfrac{1}{2R_{t,5} + \cfrac{1}{\cfrac{1}{R_{0,3}} + \cfrac{1}{2R_{t,6} + \cfrac{1}{\cfrac{1}{R_{0,4}} + \cfrac{1}{2R_{t,7} + \cfrac{1}{\cfrac{1}{R_{90,4}} + \cfrac{1}{2R_{t,8} + \cfrac{1}{\cfrac{1}{R_{90,5}} + \cfrac{1}{2R_{t,9} + \cfrac{1}{\cfrac{1}{R_{90,6}}}}}}}}}}}}}}}}}}}}}}$$

(4.13)

The initial electrical resistance from the experiments is 2.47 ± 0.24 Ω and the analytical model calculates 2.37 Ω. Hence, the model gives a slightly lower initial resistance than observed experimentally, but the value is in the scatter of the experimental values (some measured values lie above and some lie below the calculated values).

To compare the analytical results with results from the electrical measurements, electrical resistance changes of the first 10 IFF are analyzed for 14 different experimental measurements. For the first calculation, the reduction of the effective area (p) is kept constant. This means that we assume the change of effective area to be independent of the number of IFF (except for the first IFF – here, the effective area is not reduced) as well as independent of the position of the failure. Calculations are conducted for p = 5 % to p = 10 % and plotted with the experimental data (see Figure 4.22). These values were chosen as they fit well into the range of the corresponding resistance increases per IFF observed in the experiments.

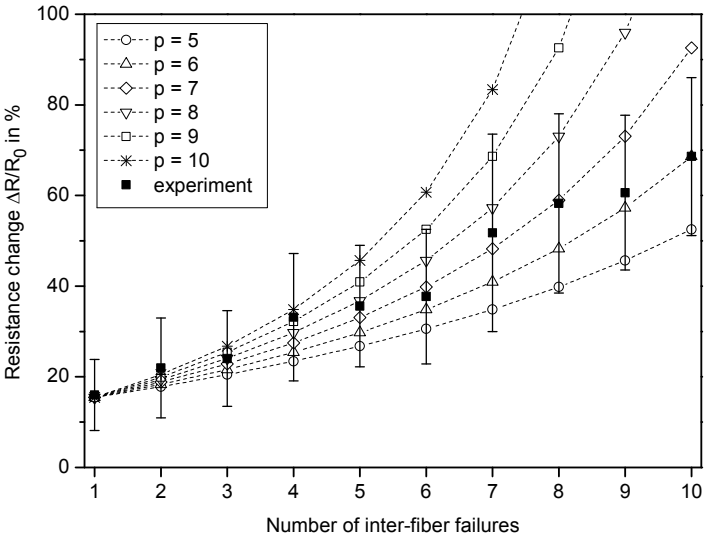

Figure 4.22: Resistance change for first ten inter-fiber failures with assumption that every inter-fiber failure has the same influence on the resistance change, independent of number and location.

For low numbers of IFF, i < 5, the analytical solutions for p > 7 fit best to the experimental values. However, for higher numbers of IFF, i > 5, these analytical solutions overestimate the resistance change significantly and the analytical solutions for p = 6 and p = 7 lie closer to the measured values. In general, for increasing number of IFF, the analytical solutions overestimate the experimentally determined values for the resistance change. This discrepancy is caused by the fact that statistically the reduction of the effective area decreases for increasing number of IFF, because of two reasons: First, if an IFF occurs between two existing IFF, the resistance increase is significantly smaller. Second, the more cracks are present, the closer the cracks lie together and the effect of the change of the effective area decreases. Therefore, it is necessary to adjust the model as described in the next paragraph.

Due to the statistically decreasing influence of a crack for increasing numbers of IFF, the parameter p is adjusted depending on the number of IFF (i) as follows:

$$p_1 = p \tag{4.14}$$

$$p_{i+1} = 0.94 \cdot p_i \quad \text{for i} > 0 \tag{4.15}$$

The factor 0.94 is determined from the experiments by evaluation of the decreasing resistance changes for increasing number of IFF.

In addition to the influence of IFF, the change of the effective area due to delaminations needs to be considered. The delamination area is taken from the ultrasonic C-scans (see Figure 4.18) and plotted in a diagram with a linear fit describing the delamination area. The axis describing the number of IFF is also approximated from the experimental results (see Figure 4.23).

Due to the different x-axes of the number of IFF and the displacement, the linear fit function needs to be defined. Then, the delamination area can be expressed as follows:

$$A_{dela} = \begin{cases} 0 & i \leq 6 \\ -101.86 \cdot 10^{-6} m^2 + 14.82 \cdot 10^{-6} m^2 \cdot i & for \quad i \geq 7 \end{cases} \tag{4.16}$$

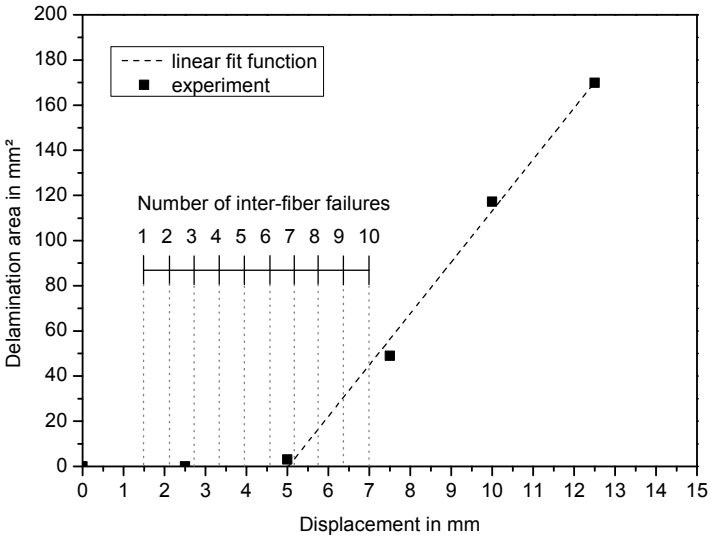

Figure 4.23: Delamination area from ultrasonic C-scans versus displacement and number of inter-fiber failures.

Therefore, the effective area of the lower 90°-layers considering both IFF and delaminations is:

$$A_{t,1} = A_{t,2} = A_{t,3} = \begin{cases} 15 \cdot 10^{-3}\, m \cdot 50 \cdot 10^{-3}\, m & for \;\; i = 0 \\ 15 \cdot 10^{-3}\, m \cdot 50 \cdot 10^{-3}\, m \cdot \frac{100 - p \cdot (i-1)}{100} - A_{dela} & for \;\; i > 0 \end{cases} \tag{4.17}$$

With the addition of the above described equations, the results of the analytical model are plotted in Figure 4.24.

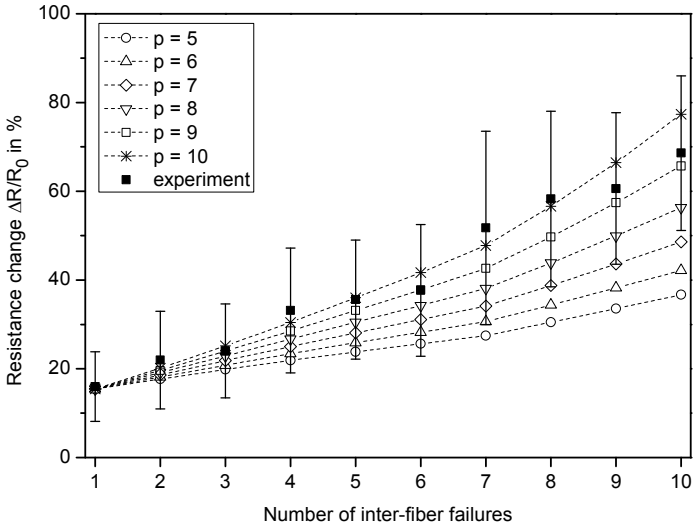

Figure 4.24: Resistance change calculated by analytical model for parameter p = 5…10 and experimental results.

It can be seen that the analytical results lie close to the experimental results for all regarded damage states for p = 9 and p = 10. The best results are obtained for p = 9.5 (see Figure 4.25). In addition, Figure 4.25 shows the contributions to the electrical resistance change caused by IFF and delaminations that were calculated separately. The influence of the IFF dominates but the curve for the IFF shows a slightly regressive behavior. Delaminations contribute to the electrical resistance change from the 7th IFF and the curve shows a progressive behavior. Therefore, it can be concluded that the influence of IFF dominates for the less damaged state. However, for increasing amount of damages, the influence of the delaminations increases.

The reason why the contribution of delaminations to the resistance increase sets in after several IFF are already present can be explained by the fact that delaminations occur after the first IFF because of high inter-laminar shear stresses at the crack tips of the present IFF. Eventually, the delaminations start growing leading to an increasing contribution of the delaminations.

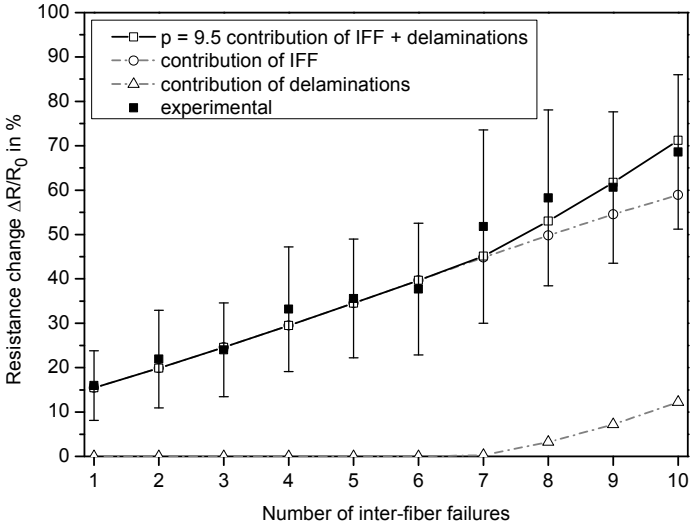

Figure 4.25: Resistance change calculated by analytical model for parameter p = 9.5 and experimental results as well as contribution of inter-fiber failures and delaminations to resistance change.

The analytical model shows good agreement with experiments for the initial resistance of the undamaged specimen. Furthermore, the analytical results show good agreement with experiments for electrical resistance change caused by IFF and delaminations. The model can be used to predict the electrical resistance change for a defined loading and damage state and it can be estimated how the IFF and delaminations each contribute to the total electrical resistance change. With relatively small adjustments, this analytical model could be adapted to other cross-ply laminate layups with different geometries and electrical conductivities.

4.3.5 Impact damage detection

Figure 4.26 shows representative heat maps constructed from through-thickness electrical resistance measurements including the delamination area, determined by ultrasonic C-scans. For the measurements that consider only the electrode pairs consisting of electrodes that lie directly on the other side of the specimen (see Figure 4.26 (a)), the highest electrical resistance measured is located around the electrode located at (62.5 mm, 37.5 mm). It can be seen that the delamination area lies close to this electrode. However, the resistance increase indicates a damage location slightly to the right of the measured delamination area. Figure 4.26 (b) shows measurements that consider the through-thickness measurement of all electrodes of the opposite side that lie within a distance of ± 25 mm with respect to the considered electrode in x- and y-direction, respectively. The maximum

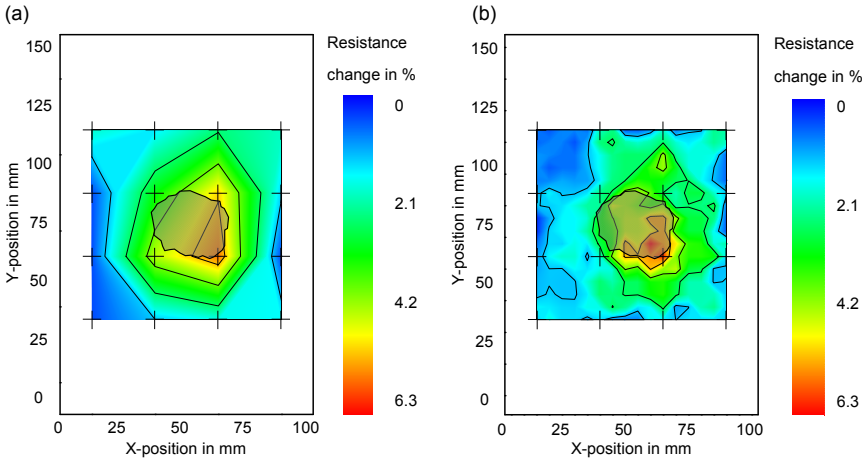

Figure 4.26: Heat map showing electrical resistance change for CFRP specimen with impact damage. Contour of impact damage is shown in transparent gray, locations of electrodes are marked as crosses; (a) Through-thickness measurement considering only electrode pairs that lie directly on opposite sides of the specimen; (b) Through-thickness measurement considering all electrodes of the opposite side that lie within a distance of ± 25 mm to the considered electrode in x- and y-direction, respectively.

resistance increase again lies close to the same electrode. However, considering the first two equipotential lines, this heat map approximates the delamination area relatively good.

Considering only in-plane measurements results in a different heat map (see Figure 4.27). Here, the maximum electrical resistance change lies close to the electrode, where fiber failure is visible on the surface. The maximum resistance increase corresponds well to the location of the fiber failure on the surface (see equipotential line with highest values). Further equipotential lines are located around the regarded electrode.

Through-thickness measurements can estimate the location of the delamination area relatively well. Considering more electrode pairs than only the ones lying directly opposite of each other can improve the damage location accuracy and leads to a better resolution of the damaged area. In-plane measurements are not as suitable for delamination area detection,

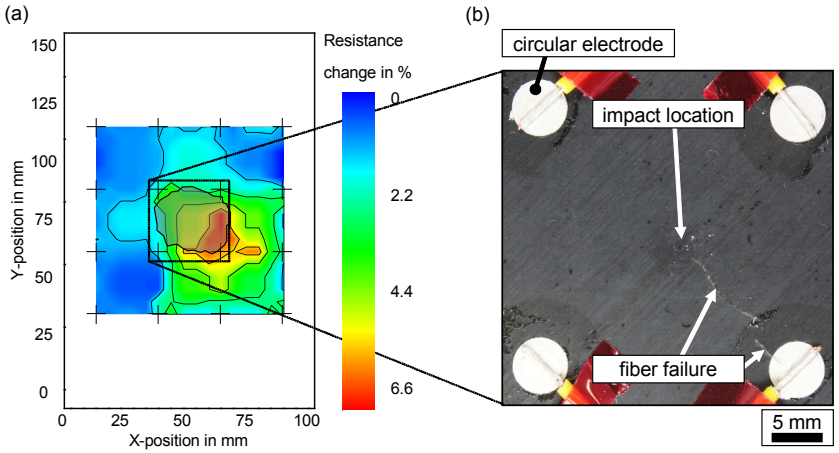

Figure 4.27: Heat map showing electrical resistance change for CFRP specimen with impact damage. Contour of impact damage is shown in transparent gray, locations of electrodes are marked as crosses; (a) In-plane measurement on impact side, considering the eight closest electrodes on the same specimen side (i.e. the surrounding electrodes in the same plane); (b) Detail of the impacted specimen area with surficial fiber failure.

because the damages close to the surface dominate the measured resistance change (this has also been shown by Xia et al. [161]). Hence, through-thickness measurements are more suitable to detect damages below the surface and in-plane measurements are better suited to detect damages at or close to the surface. Combining both measurement techniques offers the opportunity to distinguish between surface cracks and damages further below the surface.

4.3.6 Omega stringer/skin demonstrator

For the omega stringer, first the electrical resistances measured before introduction of the impacts are analyzed. If all measurements are considered, the initially measured resistances range from 1 Ω to 210 Ω. The different distances and orientations between the electrode pairs as well as their geometries cause these relatively large differences of the initial resistances. The larger the electrodes and the closer the distance between the electrodes, the lower is the electrical resistance for the electrode pair.

To evaluate the resistance change due to the impact damage over the whole area of the stringer, selected electrode pairs that lie close to each other and on opposite sides of the stringer are chosen and evaluated. Hence, a through-thickness measurement of the resistances over the whole part can be achieved. At the locations of the three introduced impacts, the resistance is significantly increased. For the foot impacts, the maximum resistance increases are 285 % and 126 %, respectively. For the head impact, the maximum resistance increase is 154 %. Due to the difference of these three local maximum values, the resistance change of the three regarded areas (left foot, head, right food) is normalized by setting each local maximum value to 100 %. With this normalization, it is possible to see all significant resistance changes at the three areas of the stringer. Figure 4.28 shows the normalized resistance change due to the three introduced impacts.

The increased resistances correspond well with the impact damage locations. Therefore, detection and localization of the damages is possible. The localization potential of the foot impacts (F1 and F2) is excellent. However, due to the electrode design, the localization possibility of the head impact (H1) is not as precise as for the foot impacts. For a more precise damage localization of the head impact (H1) more conductive paths would be necessary to improve the resolution of the monitored area. Hence, the electrode design determines the localization potential significantly.

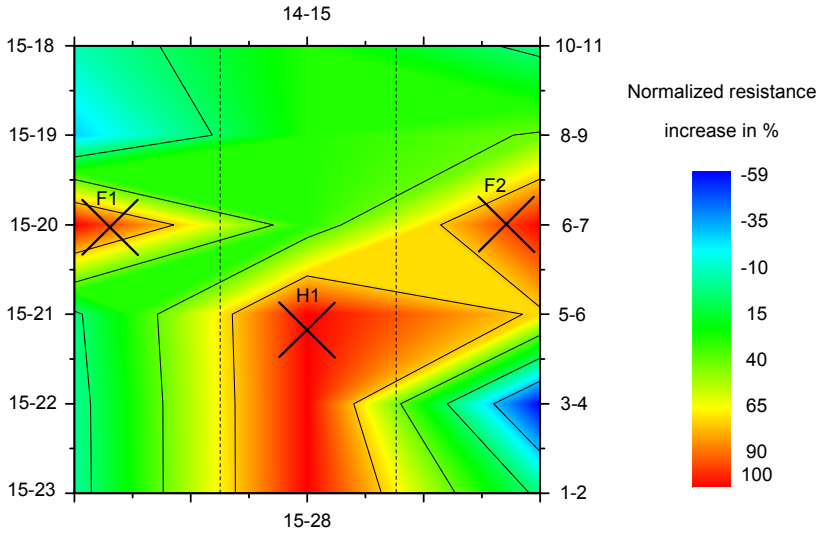

Figure 4.28: Normalized resistance change of through-thickness measurements caused by impact for top view of omega stringer; Impact locations are marked as X with F1 and F2 being foot impacts and H1 being a head impact; Pairs of numbers describe the channels between the resistance was measured.

5 Structural health monitoring of adhesive bondings via electrical resistance measurement

In this chapter, investigations are presented that aim to develop a non-destructive testing method to monitor the integrity of composite bonded joints and repairs with the ability to localize the damage.

Therefore, conductive paths are applied onto non-conductive GFRP structures by inkjet printing. CNT modified adhesive films are manufactured to enable electrical resistance measurements through the bond line. Impacts are introduced into adhesively bonded GFRP plates and electrical resistance measurements are carried out to detect and in particular to localize damages. The results are compared and verified by ultrasonic inspection, reflected light scans, and light microscopy. Furthermore, adhesively bonded scarf joints subject to cyclic loading are investigated. Conductive paths are inkjet-printed onto scarfed and electrically insulated CFRP surfaces and CNT modified adhesive films are used to enable electrical resistance measurements through the bond line. The bonded joints are exposed to cyclic loading and electrical resistance measurements are carried out. Damage mapping is used to detect and localize damages and the results are compared with strain measurements using DIC.

5.1 Specimen preparation

5.1.1 CNT modified adhesive films

For the manufacturing of the adhesive films, epoxy resin and 0.5 wt.% SWCNT were mixed in a glovebox and dispersed using a three-roll mill (120E by EXAKT Advanced Technologies GmbH). The milling process was conducted seven times at constant rotational speed of the rolls of 33 min^{-1}, 100 min^{-1}, and 300 min^{-1}, respectively. To achieve a good dispersion quality

of the SWCNT in the resin, the gap widths between the rolls were 120 µm and 40 µm for the first step, 40 µm and 13 µm for the second step, and 13 µm and 5 µm for the subsequent five steps. A minimum gap size of 5 µm results in a uniform dispersion and a retention of the aspect ratio of CNT as shown earlier by Gojny et al. [162]. The chosen parameters result in very well and uniformly dispersed particles in the polymer, as presented in different investigations [118,163–165]. From this dispersion, the company 3M Germany GmbH manufactured adhesive films with a SWCNT content of 0.1 wt.%. This nanoparticle content provides electrical conductivity above the percolation threshold even for thin regions of the adhesive film. A nylon carrier cloth guarantees a minimum bond line thickness after curing. Figure 5.1 shows a light microscopy image of the used carrier cloth without adhesive film.

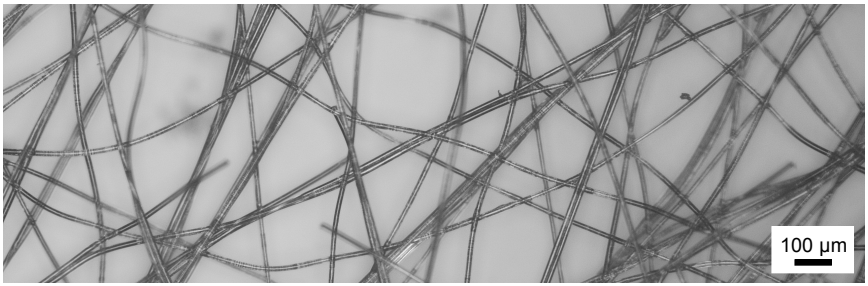

Figure 5.1: Light microscopy observation of carrier cloth used in the adhesive films.

5.1.2 Adhesively bonded GFRP specimens for impact tests

Epoxy-based biaxial GFRP plates (EP GC 308) were cut to dimensions of 150 mm x 100 mm x 2 mm using a milling machine. Along two edges of the plates, notches were cut for better contacting of conductive paths. To achieve a high adhesion strength, the GFRP surfaces to be bonded were activated by a low-pressure plasma treatment (SmartPlasma 10 by Plasmatechnology) with a power of 300 W at a pressure of 0.3 mbar for 90 s.

Conductive paths out of silver nanoparticle–based ink were inkjet-printed onto the GFRP specimens using a single nozzle print head (microdrop Technologies) with a nozzle diameter of 70 µm. Conductive paths with an interspace of 8.75 mm were printed parallel to the edges. As shown in Figure 5.2, two different path designs were printed, namely, a lined design (a), where the conductive paths lie parallel to each other and a crossed design (b), where the conductive paths of the two substrates are arranged perpendicular to each other.

Then, the adhesive film was placed between two GFRP plates with the conductive paths facing toward the adhesive film. The adhesive film was cured in an autoclave process at a temperature of 125 °C and a pressure of 5 bar for 120 min in a nitrogen atmosphere. No additional sintering process

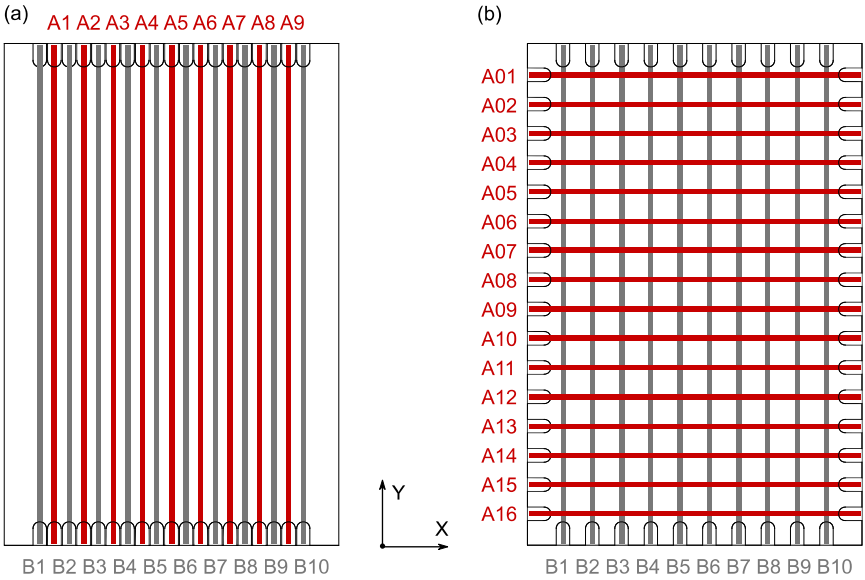

Figure 5.2: Conductive path designs for bonded GFRP specimens: conductive paths A lie in a plane above and conductive paths B lie in a plane below adhesive film; (a) Lined design with parallel conductive paths; (b) Crossed design with perpendicular conductive paths.

was necessary, because the autoclave process involves a sintering of the conductive silver paths.

To enable reliable contacting for resistance measurements, stranded copper wires were connected with the printed conductive paths using conductive silver paint (Acheson Silver DAG 1415 M).

5.1.3 Adhesively bonded CFRP scarf joint specimens for cyclic tests

The used carbon fiber reinforced prepregs consist of an epoxy matrix and carbon fibers (HexPly M21/34%/UD194/T800S by Hexcel). CFRP plates with the laminate layup $[-45/90/45/0]_S$ were laminated from prepregs and cured in an autoclave process at a temperature of 180 °C and a pressure of 7 bar for 120 minutes in a nitrogen atmosphere. Subsequently, the plates were tapered with a scarf angle of 2.86° (corresponding to a thickness to length ratio of 1:20) using a diamond coated milling cutter (OptiMill-Composite-Speed M7218-1000AQ by Mapal) operated in a CNC mill. To achieve electrical insulation, a phenolic resin based coating (2242 by Kal-Gard) with a thickness of 6.9 ± 1.7 µm (measured by light microscopy) was spray applied onto the surface of the scarfed CFRP. Conductive paths out of silver nanoparticle-based ink were inkjet-printed onto the scarfed and coated areas using a single nozzle print head (by microdrop Technologies) with a nozzle diameter of 70 µm. The conductive paths have an interspace of 8.75 mm and were placed parallel to the edges of the specimens.

The adhesive film was placed between two scarfed surfaces and cured under vacuum in an autoclave process at a temperature of 125 °C and a pressure of 5 bar for 120 minutes in a nitrogen atmosphere. No additional sintering process was necessary, because the autoclave process involves a sintering of the conductive silver paths. To enable reliable contacting for resistance measurements, stranded copper wires were connected with the printed conductive paths using conductive silver paint (Acheson Silver DAG 1415M).

GFRP with fibers oriented in ±45° direction and aluminum tabs with a width of 50 mm and a thickness of 1 mm were bonded onto both ends of the cured

plates with solvent free two-part epoxy adhesive (UHU plus endfest 300) at 80 °C for 30 minutes. Specimens with dimensions of 230 mm x 25 mm x 1.5 mm with a free test length of 130 mm were cut from the plates using a water-lubricated diamond coated saw blade. The edges of the specimens were polished with abrasive paper up to 1000 grain size. Specimen geometry and the arrangement of the printed paths are shown in Figure 5.3, where the specimen is shown schematically from the top (a) and from the edge (b). The conductive path design is shown in (a) and (c). Paths 1, 2, and 3 are placed on one scarfed area and the conductive paths A and B are located on the other scarfed area, i.e. on the opposite side of the adhesive.

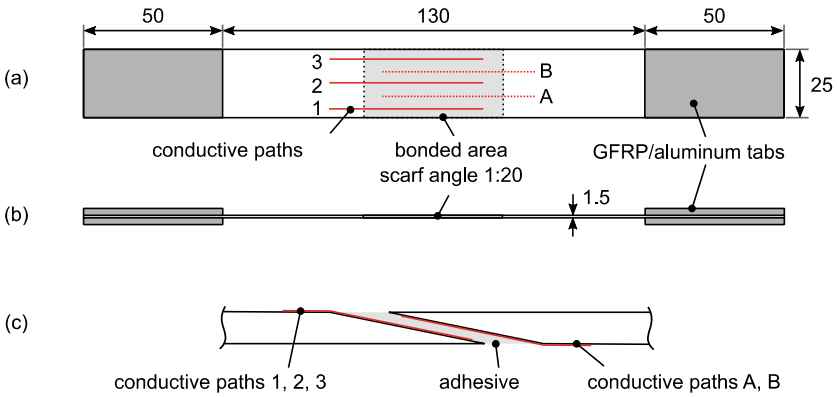

Figure 5.3: Geometry and conductive path design of CFRP scarf joint specimens.

5.2 Experimental

5.2.1 Scanning electron microscopy analyses of adhesive films

To investigate the dispersion quality of the SWCNT in the adhesive films, scanning electron microscopy (SEM) analyses were conducted on separately cured adhesive film specimens using a LEO Gemini 1530 (Zeiss) electron microscope. The InLens detector with an acceleration voltage of 15 kV was used to visualize SWCNT inside the polymer due to potential variations that are caused by electron charging close to the surface within a depth of about 50 nm as described by Kovacs et al. [166].

5.2.2 Impact tests on adhesively bonded GFRP

Through-thickness as well as in-plane continuous electrical resistance measurements were conducted using a digital multimeter (Voltcraft 91). In case of the crossed design, the resistances of all possible 160 combinations of top electrodes (A01–A16) to bottom electrodes (B01–B10) were measured for the through-thickness measurements. In case of the lined design, the resistances of each conductive path to the two closest conductive paths from the opposite side of the adhesive film (A1–B1, A1–B2, A2–B2, A2–B3, etc.) were measured for the through-thickness measurements, resulting in 18 combinations. In-plane measurements were conducted measuring the resistance of the adjacent paths in both x–y planes in which the paths are located. Thus, for the crossed design, the resistances between A01 and A02, A02 and A03, and so on as well as B1 and B2, B2 and B3, and so on and for the lined design the resistance between A1 and A2, A2 and A3, and so on as well as B1 and B2, B2 and B3, and so on were measured.

Impacts were introduced into the adhesively bonded GFRP specimens using a drop weight impact test according to ASTM D7136-05 [155]. Four clamps fix the specimen as shown in Figure 5.4. A hemispherical hardened steel impactor with a weight of 2.46 kg was dropped from a height of 560 mm

above the center of the specimen resulting in a potential energy of 13.5 J. This energy corresponds to an energy-to-thickness ratio of 3.35 J/mm, which is half of the energy per thickness specified in the above-mentioned standard. The reduction in the impact energy was chosen to avoid large damages on the surfaces. To obtain the contact force during the impact event, the head of the impactor is equipped with a strain gauge full bridge. An antirebound system prevents multiple impacts during testing.

After the impact event, the resistances of the same combinations as considered before introduction of the damage were measured again for investigation of the resistance changes due to the impact damage.

To evaluate location and size of the impact damages, ultrasonic measurements were carried out (USPC 3040; Ingenieurbüro Dr. Hillger). Pulse-echo method was used and demineralized water served as coupling medium. Additionally, reflected light scans were recorded (Epson Perfection V850 Pro) to evaluate the impact damages as well as the damage position relative to the conductive paths. For more detailed damage analysis and for determination of the bond line thickness, polished cross sections located at the center of the impacts were investigated using an optical microscope (Olympus BX51).

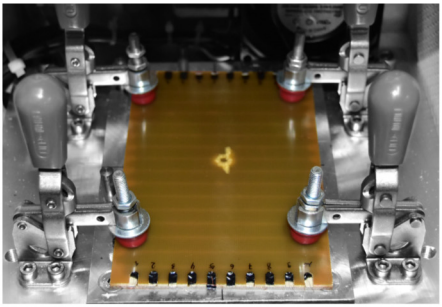

Figure 5.4: Impact test setup with four clamps holding the specimen with introduced impact damage.

5.2.3 Cyclic tests on adhesively bonded CFRP scarf joints

Axial, constant-amplitude, force-controlled, cyclic fatigue tests with coupon specimens were conducted using a servo-hydraulic 100 kN fatigue testing machine (Instron/Schenk). Specimens were fixed with a pressure of 140 bar using hydraulic clamps. Ambient conditions were kept constant with temperature and relative humidity of 23 °C and 50 %, respectively. The specimens were loaded with a sinusoidal force in the tension-tension regime with a load ratio R = 0.1 and a testing frequency of 5 Hz. Testing procedures and data acquisition were carried out using the software WaveMatrix (Instron). For each test, maximum force (F_{max}) and minimum force (F_{min}) were kept constant. The schematic test procedure is shown in Figure 5.5. DC electrical resistance measurements during fatigue testing were conducted using a digital multimeter (Keithley 2000). Four resistance combinations, namely A to 1, A to 2, B to 2, and B to 3, were measured successively with a measurement duration of 1 second (five cycles) per channel. For contactless measurement of strain and crack propagation on the edge of the specimen in

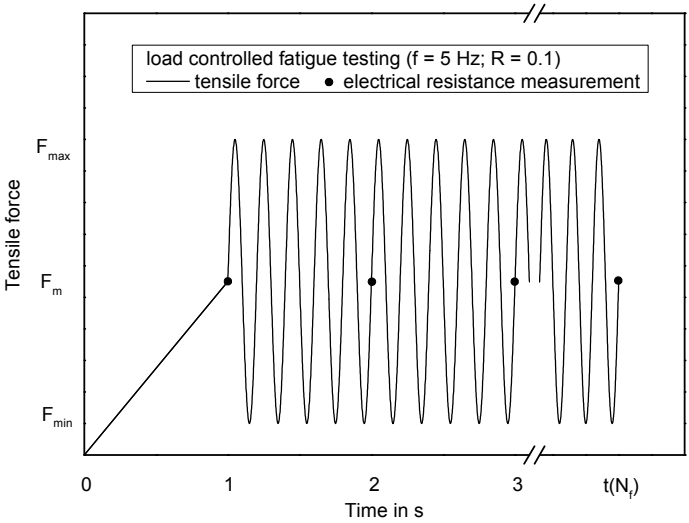

Figure 5.5: Schematic test procedure for fatigue tests with electrical resistance measurements.

the scarfed area, DIC measurements were carried out using an Aramis 4M system (GOM GmbH). Due to the small measuring area of 10 x 7 mm^2, a two-dimensional setup with one camera is used as suggested by Kosmann et al. [167]. A speckle pattern sprayed onto the edges of the specimens allows for computer-aided image evaluation with the software GOM Correlate 2016 (GOM GmbH). The camera points to the edge next to the conductive path 3.

5.3 Results

5.3.1 Adhesive film

The SEM images of adhesive film specimens show that the SWCNT were effectively dispersed within the three-roll mill process resulting in an excellent dispersion quality with no visible agglomerates (see Figure 5.6).

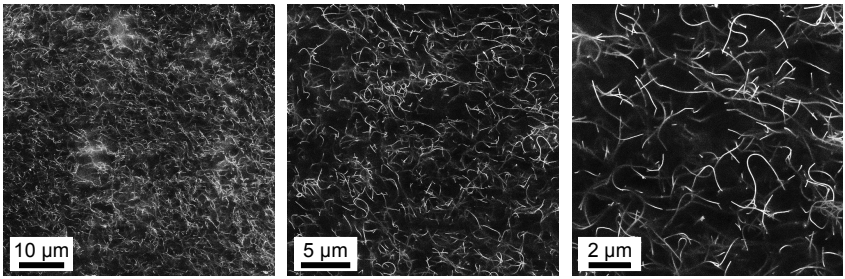

Figure 5.6: Representative SEM images of adhesive film with 0.1 wt.% SWCNT, increasing magnification from left to right, CNT appear bright and polymer matrix dark.

5.3.2 Impact tests on adhesively bonded GFRP

Impact characterization

Ultrasonic C-scans and reflected light images of the delamination area are presented in Figure 5.7 for a representative specimen. For both imaging techniques, damage size and shape are very similar, and the contour is approximately identical. Hence, for further comparisons of damage size and localization by electrical resistance measurements, the contour of these images can be used.

The cross-sectional view of the damaged area (see (c) and (d) of Figure 5.8) shows that matrix cracks and delaminations spread in a conical pattern (also referred to as pine tree shape damage pattern), which is typical for impact damages in FRP laminates. For better visibility of the damage, Figure 5.8 (d) shows only the damages, whereas all other areas are displayed in white. Two different damage mechanisms in the adhesive film are found. Therefore, two representative examples are shown with higher magnification.

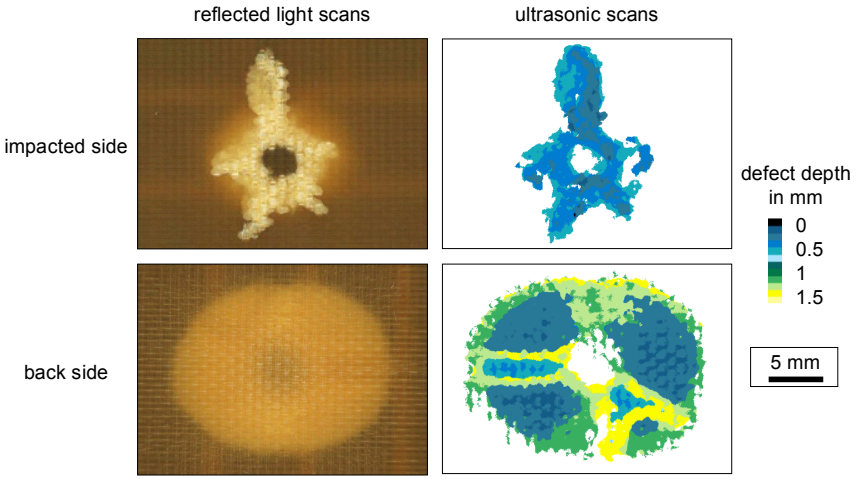

Figure 5.7: Reflected light and ultrasonic scans of damaged area taken from both impacted and back side.

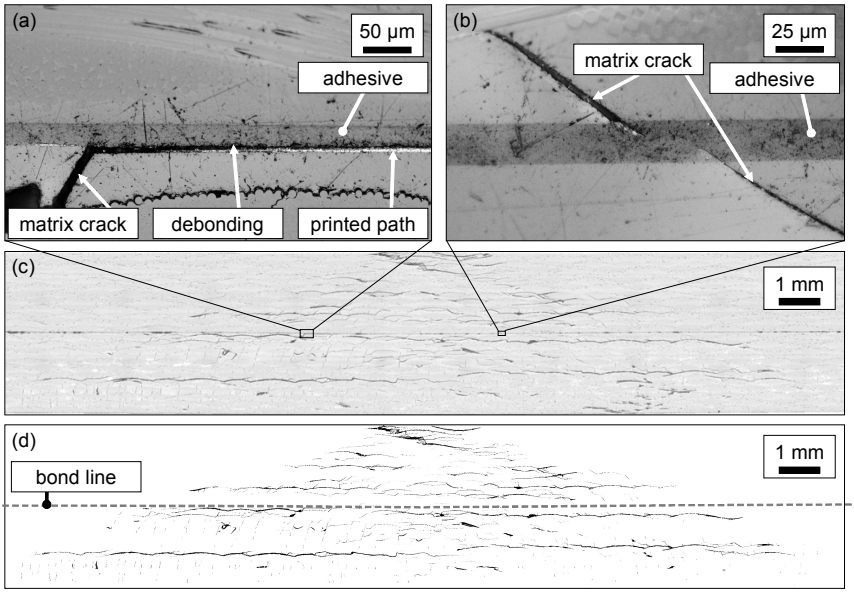

Figure 5.8: Micrographs of impact damage, view from center of impact: (a) Detail of crack at interface of conductive path and adhesive film (damage mechanism A); (b) Detail of crack running into adhesive film (damage mechanism B); (c) Cross-sectional view of impact; (d) Cross-sectional view of impact, only cracks are displayed.

In Figure 5.8 (a) (damage mechanism A), a matrix crack is connected to a damage at the interface of adhesive and silver path (debonding). The connection of the debonding and the matrix crack is located at the edge of the silver path. In Figure 5.8 (b) (damage mechanism B), two matrix cracks run into the adhesive from top and bottom sides and stop inside of the adhesive without running through the adhesive film. Additionally, matrix cracks that run into the adhesive from only one side and stop inside of the adhesive have been observed. These damages in the adhesive are located over the length of the damaged area and were not observed outside of the conical damage pattern. Both described damage mechanisms contribute to an increase of the resistance in the damaged adhesive regions for in-plane and through-thickness electrical resistance as described below.

In-plane electrical resistance measurements

Figure 5.9 shows the measured in-plane resistance changes for the specimens with parallel lined path design. The locations of the resistance changes are defined by the given coordinate system. The lower left corner and the upper right corner of the specimen correspond to x = 0 mm, y = 0 mm and x = 100 mm, y = 150 mm, respectively. Reflected light images of the impact location show the size and shape of the impact measured on both surfaces. On the front surface, the indentation of the impact can be seen as a circle in the center of the damage. The conductive paths are visible as vertical

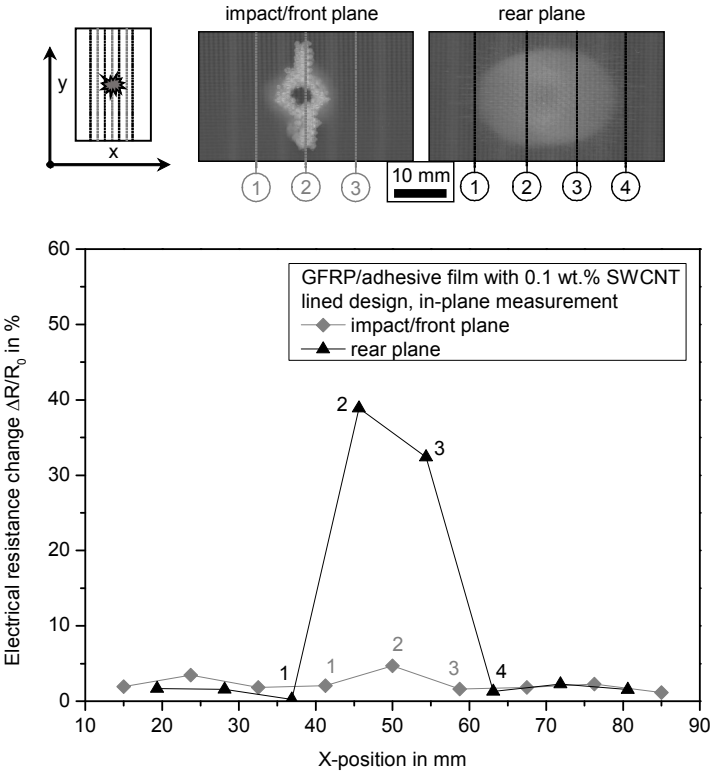

Figure 5.9: In-plane electrical resistance change and reflected light images of impact locations of both surfaces of specimen with lined path design and correlation with reflected light images.

lines lighter than the rest of the specimen. Lines in the reflected light images indicate the locations in between two conductive paths where the electrical resistance measurements were conducted.

On the front side, the electrical resistance change in this plane (indicated by gray squares) is relatively small over the whole length of the specimen with a maximum of 5 % at location 2. It can be seen that the delaminations overlap only slightly with two conductive paths (left and right from mark 2), and the other conductive paths are completely outside of the delamination area. However, the maximum of the resistance increase matches the impact damage location. On the rear side, the resistance change (indicated by black triangles) shows a clear increase of 39 % and 33 % for locations 2 and 3, respectively. As expected, the undamaged regions show no significant resistance change. In x-direction, the size of the delaminations on the rear is larger compared to the size of the delaminations on the front. On the rear, the delamination overlaps three conductive paths (left and right from mark 2 and mark 3, respectively).

The regions where impact damages overlap conductive paths show a significantly increased resistance after the impact. The resistance is only marginally increased in case of a delamination area in between two conductive paths on the front plane (as in region 2), since only damage mechanism B occurs here. The resistance increase that can be seen on the rear plane in regions 2 and 3 is assumed to be caused dominantly by damage mechanism A. Potentially, damages of the conductive paths caused by the impact could add to a resistance increase.

Therefore, a damage detection and localization is possible in x-direction with in-plane measurements when the damage is larger than the interspace of two conductive paths. If the damage is located between two conductive paths and the paths are not affected by the damage (i.e. only damage mechanism B occurs), a reliable detection and localization of the damage is more difficult because of only slight increase in resistance. Hence, the interspace distance of the conductive paths determines the threshold for the smallest impact damages that are detectable.

The results of the in-plane resistance measurements for a specimen with a crossed path design are shown in Figure 5.10. Due to the perpendicular path arrangement, on the front plane the impact damage two conductive paths. A resistance increase for the measuring regions 2, 3, and 4 is seen. This corresponds exactly to the impact damage region. On the rear plane, the damage also overlaps two conductive paths and the resistance is increased significantly for the three regions next to these paths.

A damage detection and localization of the introduced damage is possible in both x- and y-directions when a crossed path design is used.

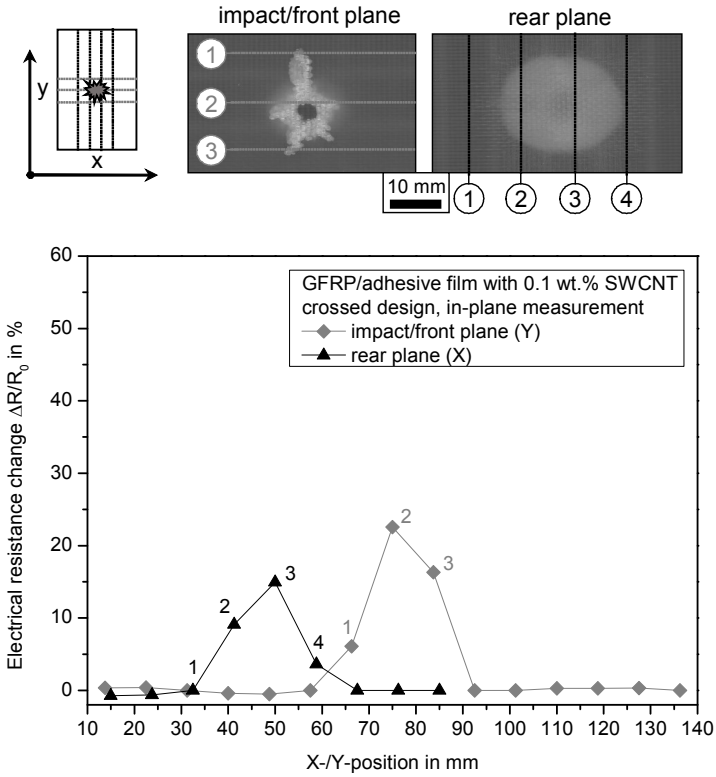

Figure 5.10: In-plane electrical resistance change and reflected light images of impact locations of both surfaces of specimen with crossed path design and correlation with reflected light images.

Through-thickness electrical resistance measurements

The through-thickness electrical resistances for a specimen with parallel lined path design are measured before introduction of the impact. Initially, the measured through-thickness resistance ranges from 273 Ω to 480 Ω. The relatively large differences of the measured values can be attributed to manufacturing influences and in particular to deviations of the bond line thickness that could be observed using light microscopy. The resistance change due to the impact damage is shown in Figure 5.11 on the left. The resistance change shows a significant increase from 45 mm to 55 mm in x-direction and has a maximum of 78.6 %. The increased resistance corresponds well with impact damage location and size (marked in transparent gray) taken from the reflected light images from both sides of the specimen. Therefore, a damage localization is possible in x-direction. In addition, the size of the impact damage can be approximated with an accuracy that is determined by the distance between the conductive paths.

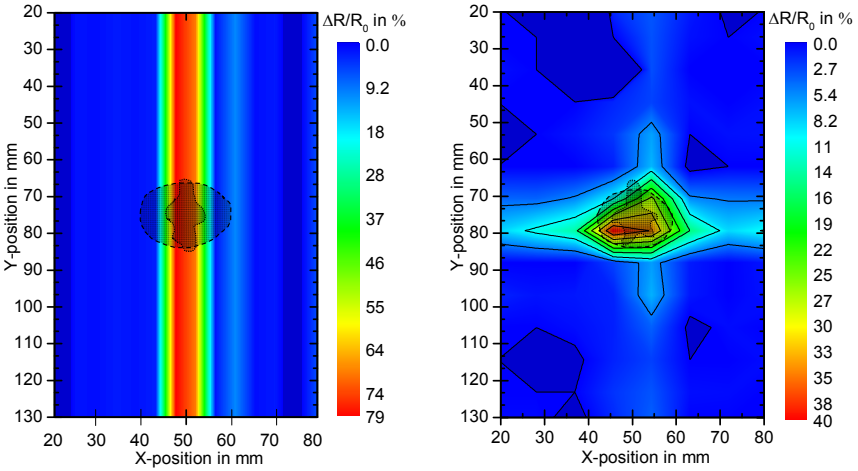

Figure 5.11: Resistance change of through-thickness measurements caused by impact, impact damage area (transparent gray) measured on upper and lower surfaces; Left: lined path design; Right: crossed path design.

In Figure 5.11 on the right, the results from the through-thickness electrical resistance measurement on a specimen with a crossed path design are shown. The measured resistance ranges from 65 Ω to 286 Ω. After impact introduction, the resistance significantly increases in the center of the specimen with a maximum of 40 % compared to the resistance before damage introduction. It can be seen that the shape and size of the area with significantly increased resistance represent the damaged area (indicated in transparent gray) accurately.

The measured resistance changes of 40 % and 78.6 % are relatively high. Therefore, other parameters with an influence on the measured resistance like temperature or measuring device and measuring technique do not hinder the damage localization potential. This also goes for unevenly distributed resistances measured before damage introduction, since the significant resistance changes are only present in the damaged areas, independent of the absolute values of the measured resistances.

Bond line thickness and electrical resistance correlation

A correlation of bond line thickness measured by using light microscopy images of different cross sections and the electrical resistance measured before damage introduction is shown in Figure 5.12. The electrical resistance increases with increasing bond line thickness. For the range of 20–180 µm, the relation of these two parameters can be described with a linear equation.

The relatively low amount of measured values in the range of 60–110 µm is caused by a nonlinear distributed thickness of the bond line in the considered cross sections. For further decreasing bond line thicknesses, the linear relation is not valid, since for a bond line thickness of 0 µm the conductive paths would be in contact and the resistance would be in a range of a few ohms, because only the resistance of the conductive paths would contribute to the measured resistance. However, for the range considered here, a good correlation is achieved by the linear fit with a coefficient of determination $R^2 = 0.9$. The good correlation and linear relation prove that a

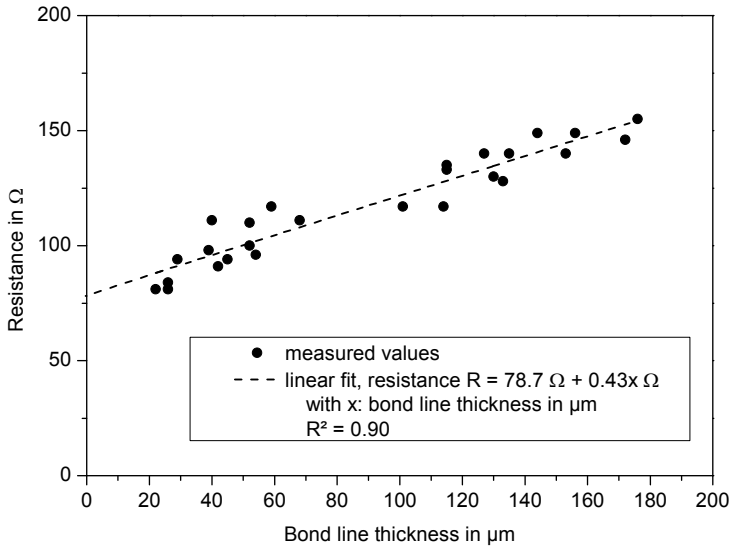

Figure 5.12: Dependency of measured resistance before damage introduction and bond line thickness.

good dispersion quality of the SWCNT is present in the adhesive. Hence, the measured resistance before damage introduction can be used to determine the bond line thickness at specific areas as well as the bond line thickness distribution over the monitored area. With other non-destructive testing methods, a determination of the bond line thickness is very difficult to achieve. Therefore, this method has a high potential to be used also for a quality control of adhesively bonded joints.

5.3.3 Cyclic tests on adhesively bonded CFRP scarf joints

In an S-N curve the maximum stress versus the fatigue life is plotted (see Figure 5.13). The fatigue life is defined as the number of cycles that a specimen sustains before final fracture. At the highest load level, with a maximum stress of σ_{max} = 213.3 MPa, the fatigue life is in the range of 10^2 cycles and at the lowest load level, with a maximum stress of σ_{max} = 106.7 MPa, the fatigue life is in the order of 10^6 cycles. The cross-sectional area of the specimens is taken for calculation of the stresses.

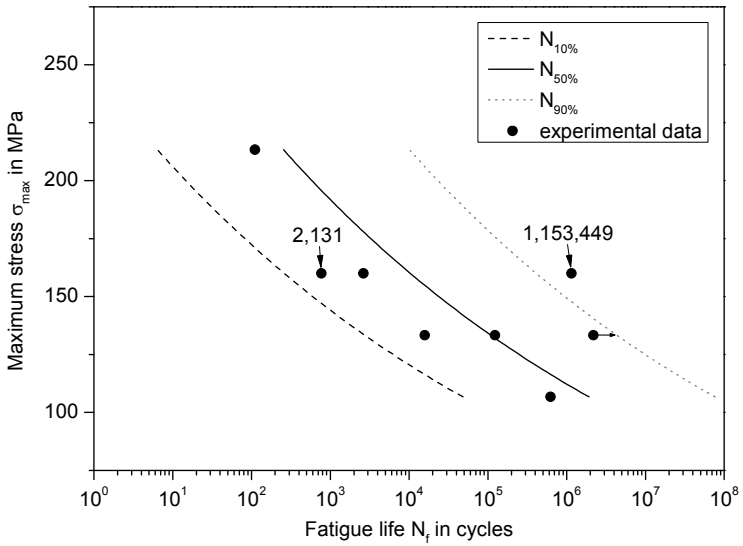

Figure 5.13: S-N curve of scarfed adhesively bonded CFRP coupon specimens, R = 0.1.

In the following, the principal strains from DIC measurements and corresponding results of electrical resistance measurements are presented exemplarily for two specimens loaded with a maximum stress of σ_{max} = 160 MPa. Results of the presented specimens exhibit life times of 2,131 cycles (see first specimen) and of 1,153,449 cycles (see second specimen). These specimens were chosen because they show two different representative behaviors observed over their life time.

Crack initiation and final failure at same location (short life time)

In Figure 5.14, results from DIC measurements are shown at four characteristic stages of the life time. The location of the recorded detail is shown on top of the figure.

1. The detail displays the principal strain at one end of the scarf joint at the beginning of cyclic loading. The strain distribution is relatively homogeneous. Only in the regions of the adhesive and of the 90°-layers the strains are slightly increased, since these regions have the lowest stiffness.

2. After 85 % of the life time, the strains increase locally at the end of the adhesive joint, indicating the presence of a crack at the edge of the adhesive along the bond line.

3. One cycle before final failure, the strains are almost unchanged and the increased strains in the damaged area are still visible and approximately of the same size.

4. After final failure (at N_f = 2,131 cycles), it can be seen that the crack moved further along the bond line.

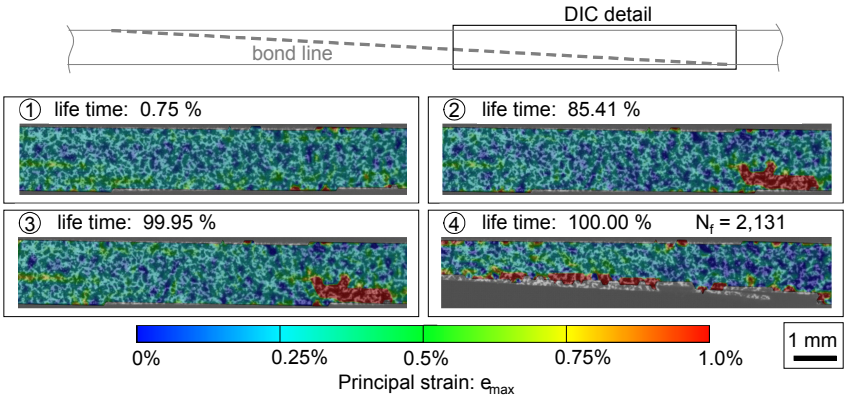

Figure 5.14: Principal strain at four different stages of the life time with crack initiation and final failure at same location.

The resistance change (defined as $[R-R_0]/R_0 = \Delta R/R_0$) of the four channels is shown in Figure 5.15. During the first 20 % of the life time, the resistance change stays in the range of ±10 % for all channels. Then, the resistances of channels 3B and 2B increase slightly and the resistances of channels 2A and 1A stay at the low level. Between 85 % and 90 % of the life time, the resistance changes rise suddenly to 40 – 100 % for all measured channels. During the last 10 % of the life time, the resistance increases further for all channels with significantly higher resistance increases of channels 2B and 3B reaching 171 % just before final failure. The initial resistances (R_0) range from 0.14 MΩ to 3.3 MΩ (channel 1A: 3.3 MΩ, channel 2A: 2.9 MΩ, channel 2B: 0.14 MΩ, channel 3B: 0.18 MΩ).

Comparing the results from DIC and electrical resistance measurements, it can be seen that the resistance increases significantly when a macroscopic damage is observed in the DIC measurements at about 85 % of the life time. Hence, the damage can clearly be detected due to a significant resistance increase. The higher resistance increase of the channels 3B and 2B suggest a

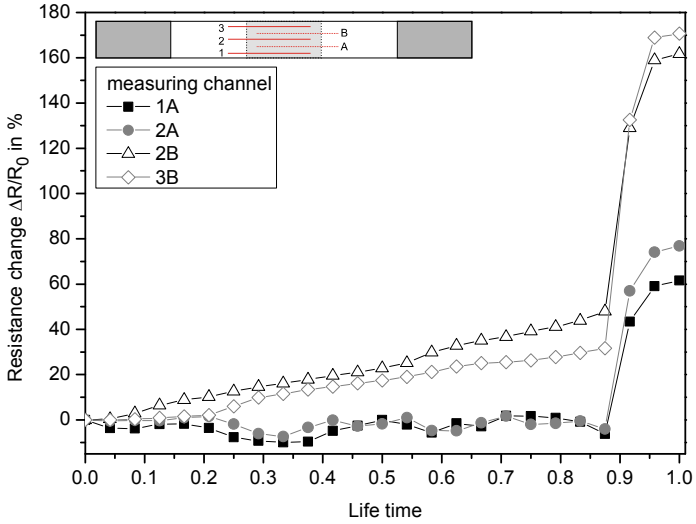

Figure 5.15: Electrical resistance changes of the four measured channels over the life time for a specimen with crack initiation and final failure at same location.

damage initiation and microscopic crack growth from 20 % to 85 % of the life time and a macroscopic crack growth from 85 % of the life time on the upper side of the specimen. From these results of DIC and electrical resistance measurement, it can be concluded that a damage detection in advance of final failure is possible and the damage can be located due to different resistance signals of the measured channels.

Negative resistance changes are present in channels 1A and 2A (lower side of specimen) starting from 20 % of the life time, which corresponds to the time at which the resistance in the channels of the upper specimen side start to increase. Since these opposing trends of the resistance changes occur synchronously, it is assumed that the microscopic damages, causing an increase of the resistance of the channels on the upper specimen side, produce a slightly asymmetrical loading condition that results in a resistance decrease of the channels on the lower specimen side due to elastic compression and plastic deformation. In addition to elastic compression, the decrease in electrical resistance can be caused by plastic deformation leading to a decreasing thickness of the adhesive as reported by Todoroki et al. for CFRP specimens [168].

Crack initiation and final failure at different locations (long life time)

The results of the specimen presented in this subsection show another typical failure mode and the corresponding resistance changes. In Figure 5.16, the principal strains are displayed in the same way as described above. The four characteristic stages are as follows.

1. At the beginning of cyclic loading, a macroscopic region with increased strains appears at the end of the adhesive along the bond line after 0.15 % of the life time.

2. After 9.13 % of the life time, the area of increased strains is slightly larger and a crack within this region is visible.

3. The crack and the area with the highest strains along the bond line increase slightly up to 99.99 % of the life time.

4. However, final failure (at N_f = 2,131 cycles) occurs along the bond line and at the end of the joint not where the crack started to grow but approximately 4 mm left of the end of the bond line.

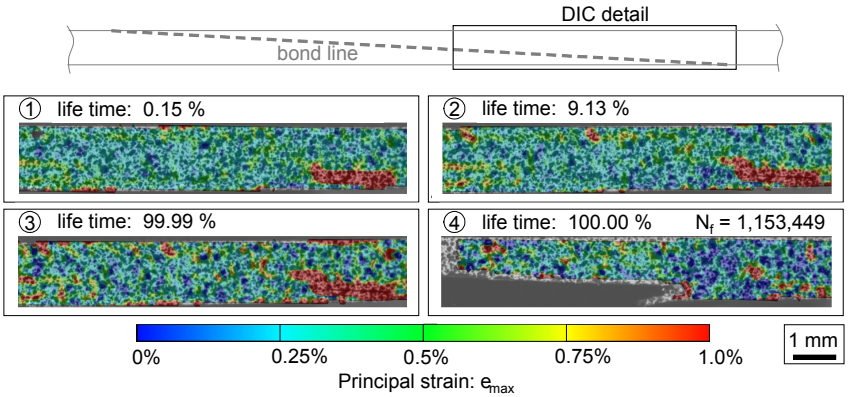

Figure 5.16: Principal strain at four different stages of the life time with crack initiation and final failure at different locations.

The plot of the resistance change versus life time for this specimen shows small resistance changes of ±15 % for all channels until a life time of around 15 % (see Figure 5.17). In this first section, channel 3B shows the highest positive resistance changes. Then the resistance decreases at the channels 1A and 2A and the resistance increases for the other two channels. At around 90 % of the life time, all channels show a resistance increase and 3B shows the highest resistance increase with 35.6 %. From 96 % of the life time until final failure, the resistance of channels 2B and 3B decreases and the resistance for the other two channels increases. The initial resistances (R_0) range from 1.4 MΩ to 2.1 MΩ (channel 1A: 2.1 MΩ, channel 2A: 2.1 MΩ, channel 2B: 1.8 MΩ, channel 3B: 1.4 MΩ).

Here, damage initiation occurs at an early stage of the life time, as can be seen from the DIC results. The resistance increases in the region where the crack growth takes place. The resistance decrease for the two "B" channels and increase for the two "A" channels, starting from approximately 96 % of the life time, occurs due to a relocation of the highest strains and therefore a

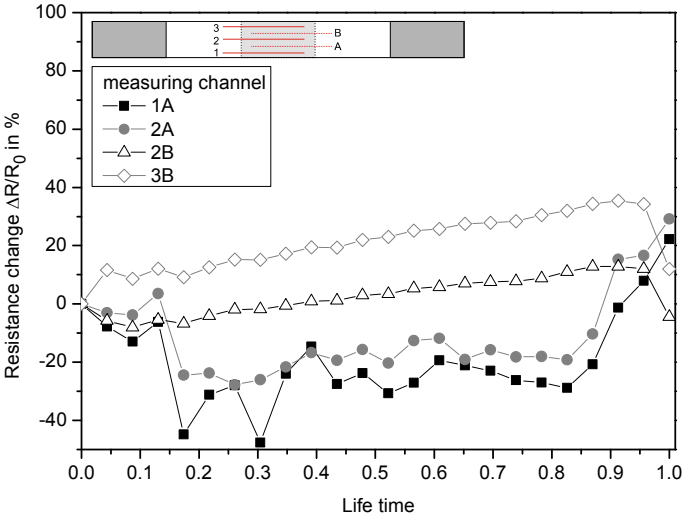

Figure 5.17: Electrical resistance changes of the four measured channels over the life time for a specimen with crack initiation and final failure at different locations.

relocation of the crack that is growing. Now the growing crack is on the lower side (opposite side of the DIC detail) of the specimen. This is confirmed by the final fracture location, which does not lie in the region where the crack growth initially took place but 4 mm to the left of the adhesive. Hence, the location of the current crack growth and a relocation of the crack growth are detectable by electrical resistance measurements, since here increasing resistance changes are present.

Again, decreasing resistances can be observed at the lower specimen side. Because the resistance decrease occurs directly after a macroscopic crack is visible for the first time in the DIC details (see Figure 5.16, detail 2), it is assumed that the negative resistance change again results from a slightly asymmetrical loading of the specimen due to the present damages.

As mentioned above, changes of the electrical resistance can be caused not only by damages, but the measured electrical resistance can be a superposition of effects of damages, elastic, and plastic deformation. The influence of elastic deformation could be observed in quasi-static tensile tests and in the presented cyclic tests by comparing the measured resistances at different loading states. It is therefore important to consider the resistance change due to elastic deformation. Hence, if a structural part is monitored with the presented method and a large variation of elastic deformation states is present, the degradation due to damages and plastic deformation can be obtained by comparing the electrical resistance change at loading states with a comparable amount of elastic deformation.

Due to the high damage detection and localization potential of the presented method, an application into an SHM system might be possible. However, the fatigue properties presented in this thesis lie below the fatigue properties of specimens without the insulating coating. To further develop the method, the mechanical performance should be improved and shifted towards the repaired specimen without insulating coating or preferably to the level of an intact CFRP laminate with the same thickness. This could be achieved by using an alternative coating material with the same electrical but higher mechanical properties and should be subject to further investigations.

6 Structural health monitoring of CNT/epoxy fibers via electrical resistance measurement

In the previous two chapters, the used conductive paths consist of metal-based ink. As shown before, metal-based inks exhibit very high electrical conductivities and are therefore suitable for damage detection and localization via electrical resistance change in CFRP as well as in electrically conductive adhesive joints. However, integrated into FRP structures and in particular in between the fibers, metal-based conductive paths could act as defects and initiate failures. For conducive paths integrated in electrically insulating composite structures as GFRP or other structures with low electrical conductivity, carbon nanoparticle/epoxy might be suitable for damage sensing.

Therefore, the study presented in this chapter aims to investigate the influence of nanoparticle morphology and filler content in polymer nanocomposites on the electrical properties in small elongated volumes with regard to the size effect. With an experimental approach representing small volumes, as they are present between the fibers in FRP and in printed conductive paths, the most promising particles for improving electrical properties are discussed. The aim is further to identify the most suitable nanoparticle morphology for sensors in SHM applications with electrically conductive paths of small volume, by determining the percolation thresholds and analyze how the electrical properties change under tensile load. Furthermore, the mechanical properties were investigated but are not part of this thesis and are described in [118].

In addition to the aspect ratio of the nanoparticles, the aspect ratio of the tested volume has an influence on the percolation threshold. Nonetheless, the geometrical influence on the percolation threshold is often neglected in experimental investigations. Most theoretic studies on percolation theory in finite systems consider cubic geometries and only few studies with respect to non-cubic, elongated geometries exist. Theoretical calculations show that

the percolation threshold increases for increasing elongation of a finite size volume [169–171]. In FRP laminates, small volumes of polymer matrix between the fibers exhibit an elongated shape. Furthermore, printed paths can exhibit an elongated shape. Hence, it is of great interest to investigate the electrical properties and in particular the piezoresistive behavior of nanoparticle modified polymers in small elongated volumes.

6.1 Specimen preparation

Epoxy fibers are produced as described in [172] using the resin Momentive Epikote RIMR 135 with the hardener Momentive Epikure RIMH 134. The resin to hardener mixing ratio is 10:3 as recommended for this system (glass transition temperature T_g = 93 °C). The method of using epoxy fibers is adapted from Hobbiebrunken et al. [173]. The different types of carbon-nanoparticles used to investigate the influence of particle morphology are SWCNT, CB and FLG (details are given in section 3.5).

For the nanoparticle modified fibers, nanoparticles and epoxy resin are mixed inside a glove box and dispersed with a three-roll mill (EXAKT Advanced Technologies GmbH 120E) that works on the principle of applying high shear rates on the mixture to disperse the nanoparticles homogeneously. The milling process is repeated seven times at constant rotational speed of the rolls of 33 min^{-1}; 100 min^{-1}, and 300 min^{-1}, respectively. The gap widths are adjusted from 120 µm to 5 µm. The amount of nanoparticles added to the resin is varied to determine the electrical percolation thresholds for the different particle morphologies in small, elongated volumes. After dispersion, the hardener is added to the modified resin and the mixture is stirred for approximately 10 min and then degassed under vacuum (15 mbar abs) for 15 min. As can be seen in SEM images (see Figure 6.3), uniform nanoparticle dispersion is obtained.

Fibers are pulled with a needle from the epoxy when it starts to vitrify. Via the pulling speed of the needle, the fiber diameter can be adjusted to a certain point. The fibers are cut and glued at one end on paper sheets based on ASTM D3379 [174] for single fiber tensile tests and then cured in an oven at

20 °C for 24 h and at 80 °C for 15 h, as recommended for this matrix system. Only one side is fixed to avoid tension stresses in the fibers because of thermal or chemical shrinkage during curing. With differential scanning calorimetry (DSC) measurements it is assured that the matrix system is completely cured. The second end of the fiber is fixed on the paper after curing. Behind the glue for fixation on the paper, the fibers are electrically contacted with silver conductive paint. The free test length is 25 mm and the electrical resistance measurement length is l_e = 27 mm.

6.2 Experimental

Figure 6.1 shows a scheme of the developed set-up for tensile tests of epoxy fibers including the measurement of the electrical resistance during mechanical testing. The specimens are mounted in a universal testing machine (Zwick Z100) with a 50 N capacity load cell. A digital multimeter (Keithley 2601A) is connected to both ends of the fiber for measuring the DC electrical resistance during the test.

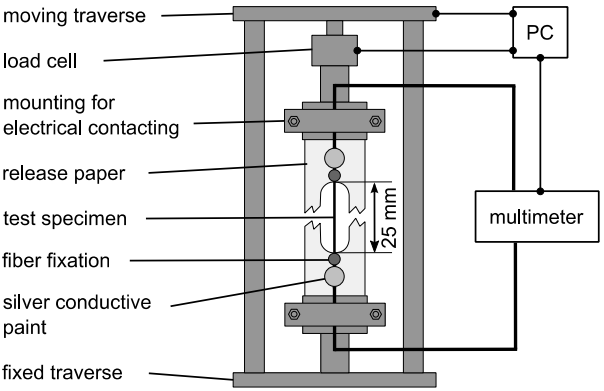

Figure 6.1: Schematic representation of test set-up for single epoxy fibers in the universal testing machine with measurement of electrical resistance during tensile test.

For investigating the distribution of the electrical resistance over the length of a single fiber, fibers are cut into two parts and the electrical resistance of both parts is measured. Subsequently, this procedure is repeated with each of the two parts of the fibers. Four-wire resistance measurement is conducted with a constant voltage of 1 V. The chosen voltage value results in low scatter of the measured resistance when compared with lower voltages. Insulation of the wires to the contacts with the fiber on the paper assures that exclusively the resistance of the fiber is measured and avoids any close circuit via the testing machine.

The side bars of the paper, connecting the upper and lower part of the specimen, are cut before testing. Test speed is set to 25 mm/min to minimize plasticity effects with necking and assure a more brittle failure mode of the fibers. The cross section after failure is analyzed for each specimen by using an optical microscope (Olympus BX51) and by SEM to determine the nanoparticle distribution. SEM is carried out using a Zeiss Leo Gemini 1530 electron microscope by using the SE2 detector with a working distance between 5 mm and 7 mm at 8 kV and without sputtering of the surface. A mixture of the SE2 detector with the InLens detector is used.

6.3 Results

In this section, the electrical characterization results are shown, including percolation threshold and the resistance distribution over the length of a single fiber. Subsequently, the resistance change during tensile loading is presented.

6.3.1 Percolation threshold and resistance distribution

For CB and FLG modified epoxy fibers, the electrical conductivity is below the geometry and device determined measuring limit. Therefore, the percolation thresholds of these fibers are above the value of the highest investigated nanoparticle concentrations of 15.0 wt.% and 2.4 wt.% for CB and FLG, respectively. The electrical resistance of CNT modified fibers is measurable and fibers with different nanoparticle concentrations are

characterized. Electrical conductivities over CNT particle concentrations for the tested fibers are plotted in Figure 6.2. The fibers with CNT contents below 0.3 wt.% exhibit a conductivity below the measuring limit (except for two specimens). A percolation threshold of 0.3 wt.% CNT is determined from the two different conductivity levels and the significant increase of conductivity at this CNT concentration.

SEM images of fracture surfaces, as shown exemplarily in Figure 6.3, highlight the structure of the CNT network. A dense network formed by homogeneously dispersed nanoparticles is visible for fibers with a CNT content of 0.5 wt.%. For fibers with CNT contents below the percolation threshold no conducting networks are visible [118]. The visible orientation of the CNT is attributed to pulled-out particles lying in crack growth direction. For the investigations presented in the following a CNT content above the percolation threshold of 0.5 wt.% is chosen to achieve electrical conductivity and piezoresistive behavior of the fibers.

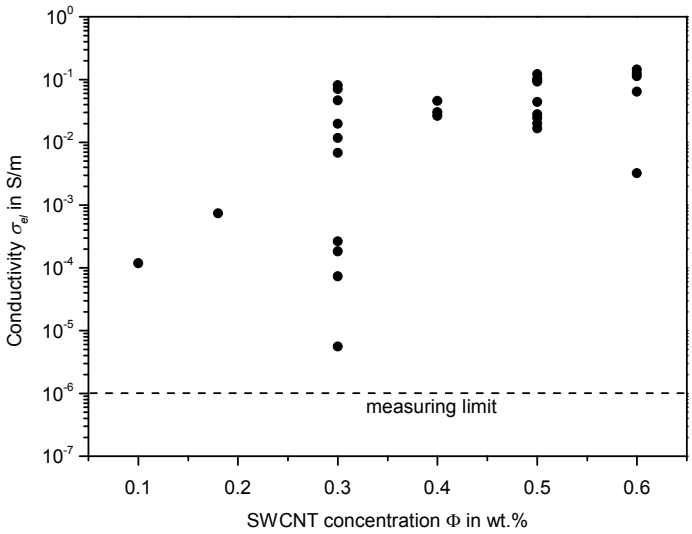

Figure 6.2: Percolation curve of SWCNT modified epoxy fibers.

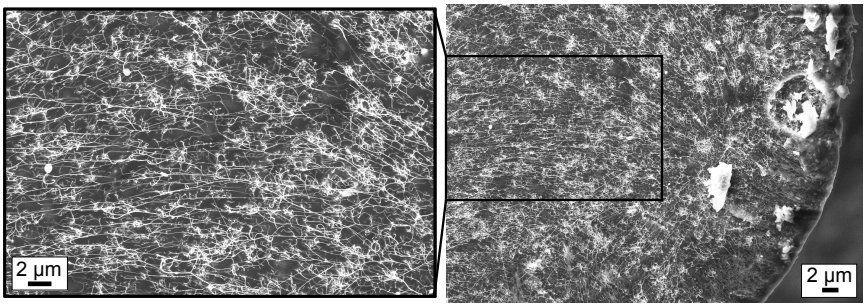

Figure 6.3: SEM image of representative fracture surface of an epoxy fiber modified with 0.5 wt.% CNT resulting in an electrically conductive nanoparticle network. Epoxy and CNT are displayed in dark gray and white, respectively.

Figure 6.4 shows the resistance measured at adjacent parts of one exemplary fiber with a diameter of d_f = 258 µm. Due to cutting the fibers and applying the new contacts, the lengths of the cut parts do not sum up to 100 %. The resistance measured over a length of 23.7 mm is 7.5 MΩ. For perfectly homogeneous distributed electrical properties, the percentages of length and resistance of the cut parts would have the same value, as the resistance per length would be the same for different parts. However, small differences in the resistance per length of the two pieces as well as of the four pieces can

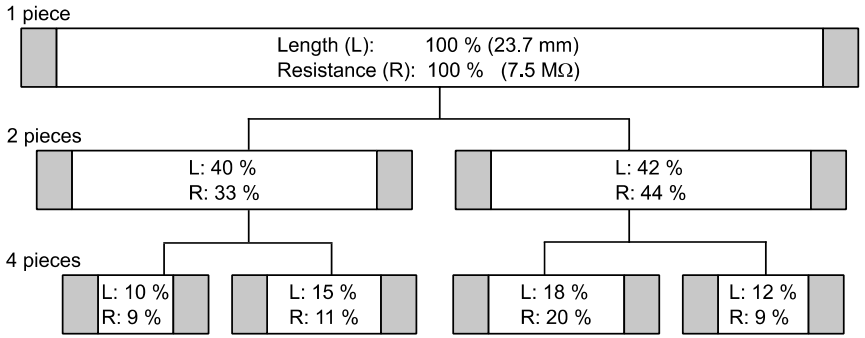

Figure 6.4: Family tree of fiber 1, d_f = 258 µm, resistance and length measured along the fiber on cut fiber parts.

be observed. Yet, for this fiber, the distribution of the resistance over the length of the fiber is relatively homogeneous.

Figure 6.5 shows the ratio of measured resistance (R) to resistance of the uncut fiber (R_1) versus the ratio of fiber length (l_e) to the length of the uncut fiber (l_{e1}). Three representative fibers with different diameters are shown. Measured values of fiber halves are plotted on the right side (l_e / l_{e1} > 30 %), whereas the left side (l_e / l_{e1} < 30 %) shows the values measured for the quarters of the same fibers. Theoretically, assuming homogeneous resistance distribution over the fiber length, $R/R_1 = l_e/l_{e1}$ applies. The dashed line indicates this relation. As can be seen in Figure 6.5, this theoretical relation is not exactly applicable in practice due to scattering of the measured values. The scatter indicates homogeneity of the distribution of the resistance over the fiber length. For example the shortest part of fiber 2 (indicated by circles) has a higher resistance, compared with the three other sections of the same fiber in the region of l_e/l_{e1} = 12 - 15 %.

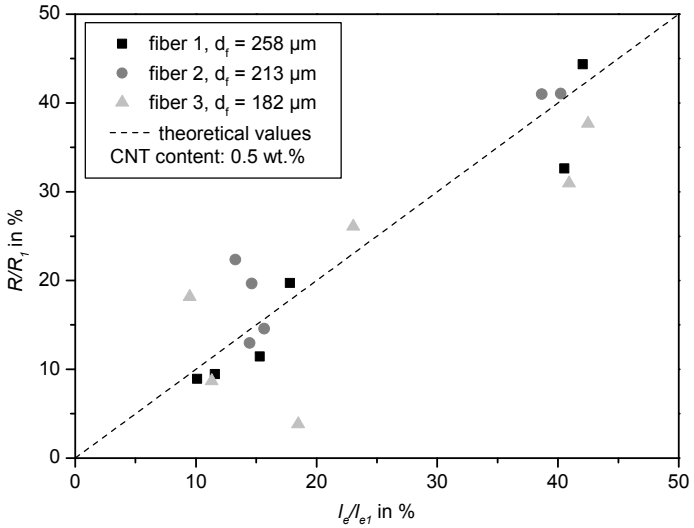

Figure 6.5: Ratio of fiber section resistance to resistance of uncut fiber versus ratio of fiber section length to length of uncut fiber.

Fibers with small diameter show a higher scatter in resistance over the length. For fibers with greater diameter ($d_f > 250$ µm), the electrical properties are distributed relatively homogeneous. Therefore, it is assumed that with an automated production process an excellent distribution of the resistance over the fiber length could be achieved.

6.3.2 Electrical resistance measurements during tensile tests

Figure 6.6 shows a representative stress-strain curve of a fiber with a CNT content of 0.5 wt.% during tensile testing with in situ electrical resistance measurement. The stress and the resistance change are shown as continuous and dashed lines, respectively. The stress is calculated from the original fiber cross section and the strain is calculated using displacement data from the moving traverse of the universal testing machine and the original fiber length. Due to the small specimen size, no other strain measurement is applicable. The stress-strain curve shows a linear region (up to $\varepsilon = 2.1$ %

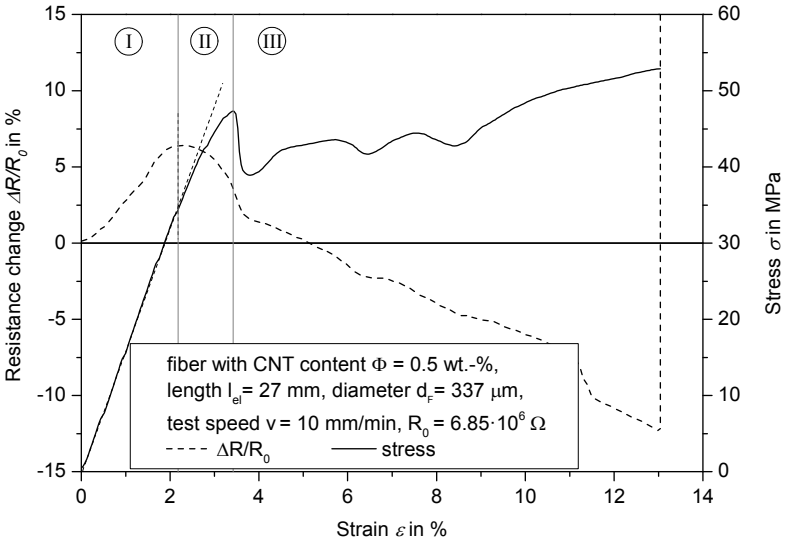

Figure 6.6: Stress-strain curve and electrical resistance change of a single epoxy fiber modified with 0.5 wt.% CNT in fiber tensile test.

strain) followed by plastic deformation and yielding (at $\varepsilon = 3.4$ % strain). Then multiple necking occurs until final fracture at $\varepsilon = 13$ % strain. The resistance increases exponentially, followed by a point of inflexion and reaches a maximum at $\varepsilon = 2.1$ % strain. The resistance decreases continuously for increasing strain and drops below the initial resistance for high strains.

The percolation thresholds of $\phi_c > 15$ wt.% for CB, $\phi_c > 2.4$ wt.% for FLG, and $\phi_c = 0.3$ wt.% for CNT lie above typical percolation thresholds reported in literature [28,67,68]. This can be explained by two mechanisms. Firstly, the nanoparticles are well dispersed and homogeneously distributed and the level of kinetic percolation is very low. Secondly, the fibrous geometry with its high aspect ratio statistically results in higher percolation thresholds, since the probability of conductive paths decreases for increasing length to diameter ratio.

For small volumes, for instance in the interspaces of fibers in FRP, this effect is often neglected but needs to be considered for choosing an appropriate nanoparticle content resulting in the desired piezoresistive properties. The resistance is not distributed homogeneously over the length of the fibers. The reason for this is a statistical distribution of the particles and the linked amount of redundant conductive network paths, which varies over the fiber length. For decreasing cross sections this influence increases due to a decreasing redundancy of network paths at the same nanoparticle content. Furthermore, variations of the fiber diameter can cause varying conductivity over the length of the fiber. Both effects explain the trend of increasing scatter with decreasing fiber diameter. The stress-strain curve is divided into three characteristic regions (see Figure 6.6) and the piezoresistive behavior is explained according to these regions.

Region I: The fibers exhibit linear elastic followed by linear viscoelastic stress-strain behavior. The resistance change shows an exponential increase followed by a point of inflexion and a maximum of $\Delta R/R_0 = 5 \pm 1$ % for all tested specimens. Since the Poisson's ratio of the matrix ($\nu = 0.38$) is smaller than 0.5, the tensile loading increases the specimen volume and therefore the average distance of the CNT increases as well. This increase of particle

distance leads to an exponential increase of the tunneling resistance, which mainly determines the electrical resistance of CNT modified polymers [74]. Hence, the resistance of the specimen increases exponentially as well. In contrast to the increase of the particle distance in length direction, the particle distance in width direction decreases, leading to a resistance decrease.

Region II: Non-linear viscoelastic and irreversible deformation occur and the matrix starts to yield. The transverse contraction increases further, causing a particle distance decrease in transverse direction and therefore the tunneling resistance decreases. Due to stress peaks induced by the particles, local viscoelastic and plastic deformation and local plastic yielding occur, leading to thinner epoxy layers between the particles and thus to a smaller distance and decreasing tunneling resistance. Shui and Chung [175] and Meeuw et al. [28] reported similar behavior for 3-D and 2-D volumes. At the resistance maximum, the opposing effects that influence the tunneling resistance compensate. On the one hand, the particle distance increases due to strain in fiber direction, on the other hand, it decreases due to transverse contraction and thinner epoxy layers between the particles due to plastic yielding. These opposed effects have a comparable influence on the tunneling and thus on the measured resistance. Hence, at this point both effects level out and no resistance change is observed.

Region III: At yield stress, necking of the fibers occurs and the effects of transverse contraction and yielding of the matrix dominate, resulting in local thinner epoxy layers between the nanoparticles. The tunneling gaps and with them the measured resistance decrease. Multiple necking occurs and the electrical resistance decreases in all these necked regions, resulting in a continuous resistance decrease until final fracture of the specimen, which leads to an unmeasurable high resistance. Final failure separates the electrical conductive path by rupture of the specimen, which results in a non-measurable high resistance.

With the described characteristic of the resistance change due to tensile loading, CNT/polymer composites with small elongated volumes can be used as strain sensors. The resistance maximum is located at the beginning of local

plastic deformation of the matrix, indicated by a decrease in the slope of the stress-strain curve (refer to Figure 6.6, slope change indicated by a dotted line). Thus, CNT modified epoxy can be used as a sensor to detect the initiation of plastic deformation and with it the initiation of irreversible damage of the material at the maximum of the measured resistance. For most applications, the ambiguity of the resistance signal, which occurs at higher strains is not problematic, because due to the stiffer fiber reinforcement, fracture in FRP occurs at lower strains than those at which the resistance decreases (as seen in [28]).

7 Conclusion

This research expands the potential of electrical resistance measurements for structural health monitoring applications by investigating and demonstrating possibilities for damage detection and localization with

- silver ink based electrodes, which are directly printed onto cured CFRP and onto uncured prepregs,
- carbon nanoparticle modified adhesive films, which are used for structural bonded joints,
- carbon nanoparticle modified epoxy fibers.

The scholarly contributions of each investigation are summarized below.

7.1 Structural health monitoring of CFRP

Inkjet-printed silver nanoparticle ink on CFRP allows for in situ monitoring and detection of both surface cracks and delaminations inside the material. If IFF occur on the surface, the electrical resistance measured along single printed paths increases due to interruptions of the printed paths, which have a significantly lower resistance than CFRP. Failures inside of the material can be detected by measuring the electrical resistance through the CFRP. With through-thickness measurements, delaminations can be detected by an increase of the electrical resistance. If multiple electrodes are printed on the material surface and several measurements are conducted synchronously, a localization of the defects is possible. Hence, in case of tailored designs of printed paths, additionally to the detection also a localization of IFF and delaminations in CFRP is possible.

Inkjet printing of silver nanoparticle ink can also be conducted onto uncured prepregs. With this approach, the paths can be integrated into the laminate between two plies. An additional process step for sintering the silver nanoparticles can be omitted, because sintering takes place during the autoclave process. Due to the low viscosity of the resin during the curing

cycle, a deformation of the conductive paths can occur. The deformation is significantly larger for paths that lie perpendicular to the fiber direction of the adjacent plies compared to paths that are arranged parallel to the fiber direction. This difference results in interrupted paths in the case of perpendicularly oriented paths and fibers and intact paths in the case of parallel oriented paths and fibers. Resulting from this difference, with a parallel orientation, damage detection and localization is possible comparable to the case of conductive paths printed on the surface. However, with a perpendicular orientation and non-continuous conductive paths, damage detection is not possible. Therefore, if printed onto prepregs, the orientation of conductive paths and fiber direction is an important parameter that determines the structural health monitoring capabilities. With regard to industrial application, an integration of the printing process into an existing automated tape laying process of prepregs could minimize the costs for application of conductive paths because no additional time-consuming process steps would be necessary for application and sintering.

The presented analytical model shows good agreement with experiments for the initial resistance and for the electrical resistance change caused by IFF and delaminations. The model can be used to predict the electrical resistance change for a defined loading and damage state and it can be estimated how the IFF and delaminations each contribute to the total electrical resistance change.

Furthermore, detection and localization of impact damages was demonstrated on both plate specimens with point electrodes and on an omega stringer with inkjet-printed conductive paths. It was found that through-thickness measurements allow for detection of delaminations and that in-plane measurements are suitable to detect surface cracks. Combining both measurement techniques offers the opportunity to distinguish between surface cracks and damages further below the surface. In through-thickness measurements, considering more electrode pairs than only the ones lying directly opposite of each other can improve the damage location accuracy and leads to a better resolution of the damaged area. Therefore, an

appropriate calculation method able to determine values for locations between the electrodes was presented.

With the used inkjet technology, more complex conductive path geometries such as branched networks are printable as well. Furthermore, printing onto curved surfaces is possible. Depending on the curvature, a print head mounted on a robotic arm could be useful. In case of the presence of structural features (e.g. stringers), a division into different systems monitoring parts and joints independently might be necessary. When applied in structures with integrated lightning protection, the conductive paths need to be arranged in a way that they do not significantly change the current flow caused by lightning. However, existing metal foils or meshes used for lightning protection can act as two-dimensional electrodes and be integrated into the structural health monitoring system for through-thickness electrical resistance measurements.

7.2 Structural health monitoring of adhesive bondings

Damage detection and localization of impact damages in adhesively bonded GFRP plates were achieved by in-plane and through-thickness electrical resistance measurements using SWCNT modified adhesive films and silver nanoparticle–based printed circuits.

In-plane measurements show that the electrical resistance measured between two adjacent conductive paths increases, if the damaged area overlaps one or both of these paths. It can be distinguished between more and less damaged areas of the adhesive due to the two damage mechanisms observed in the adhesive: a debonding at the interface of the conductive path and the adhesive results in a higher resistance increase than a matrix crack running into the adhesive.

Through-thickness measurements also show the possibility of damage detection and localization by damage mapping. Here, the resistance changes were even higher compared to the in-plane measurements. Parallel oriented paths allow for damage detection and localization in one dimension, and perpendicular oriented paths enable damage detection and localization in

two dimensions. The full localization potential of this method can be exploited only using perpendicular oriented paths, because the damage can be located within the two-dimensional laminate plane. Therefore, the perpendicular arrangement is the preferred design.

With the presented scalable method, damages can reliably be detected from the electrical resistance measurements. Furthermore, location, size, and shape of the damage as well as the intensity of the damage inside of the damaged area can be determined. In addition to the damage detection and localization potential, the bond line thickness at specific locations and the distribution of the bond line thickness can be determined using a linear relation of the bond line thickness and the through-thickness electrical resistance.

Printed conductive paths on scarfed CFRP surfaces allow for damage detection and localization by using CNT modified epoxy adhesive films and electrical resistance measurements through the adhesive during cyclic loading.

The presented method offers the opportunity to monitor the integrity of scarf repairs during operation. Significant electrical resistance increases can be linked to crack initiation and crack growth, which were confirmed with DIC measurements. Crack initiation can be identified by a sudden increase of the electrical resistance and crack growth can be detected by a rise of the resistance over the life time. Therefore, a damage of the joint can be detected clearly before final fracture and sudden catastrophic failure can be avoided. The location of the crack and the crack growth can be monitored by using a design of parallel oriented conductive paths and the sensitivity of the localization depends on the interspace of the printed conductive paths. A change of the location of the dominating growing damage is detectable due to different measured channels.

With an increased mechanical performance, the presented method may be introduced into scarf repairs of primary structures that are safety relevant to detect damages before final failure occurs. The inkjet-printed conductive

paths are applied within an automated process. Therefore, the application is relatively fast and may be implemented into an automated repair process.

7.3 Structural health monitoring of CNT/epoxy fibers

With a carbon nanoparticle modification, multifunctional materials combining electrical conductivity for damage sensing with enhanced mechanical properties are obtained. With a better understanding of simultaneous testing of mechanical and electrical properties in small elongated volumes, a size effect is found to exist for electrical properties. Carbon nanoparticle modified epoxy exhibits a significantly higher percolation threshold in small elongated volumes compared to the bulk material. For applications such as electrically conductive nanoparticle modified polymer wires, a larger amount of particles is necessary to use these volumes for sensing applications. CNT modified epoxy fibers are well suited as electrical conductive paths since the amount of filler can be adjusted in a way that the beginning of plastic yielding is identified by the maximum of resistance change. Furthermore, until onset of plastic yielding the resistance change can be used as a strain sensor. CB and FLG are identified to be not suitable to form a conductive network in small elongated volumes because percolation thresholds are very high.

For multifunctional polymer or FRP materials, CNT with a weight fraction above 0.3 wt.% are shown to be the most promising nanoparticle filler for improving both electrical and mechanical properties, even in small elongated volumes. With this modification, smart structures for structural health monitoring with improved mechanical properties can be designed.

8 Outlook

Due to the high potential of silver nanoparticle-based conductive paths on CFRP structures for SHM applications, the approach will be further investigated on larger CFRP structures that are exposed to complex load cases. Therefore, in the project “EvoCarboN”, funded by Hamburgische Investitions- und Förderbank, pultruded CFRP chassis from Carbon Truck & Trailer GmbH will be used in emission-free electric utility vehicles and monitored by electrical resistance measurements during their real application. This project aims to bring the presented approach closer to application by developing suitable electrode networks and measuring techniques that are able to detect and localize damages in large structural CFRP parts.

Concerning CNT modified epoxy fibers, further research should focus on the applicability of the proposed SHM method using electrical conductive paths in FRP laminates and structures. CNT modified polymer based conductive paths offer the possibility of excellent adhesion with a composite with polymer matrix. Therefore, CNT/polymer is a promising material combination for printed circuits for SHM on composites. Within the frame of the project „Multifunktionale Komposite - Gedruckte Elektronik zur strukturintegrierten Zustandsüberwachung von Faser-Kunststoff-Verbunden“, funded by the Deutsche Forschungsgemeinschaft, CNT modified polymers printed onto composites will be comprehensively investigated. In particular, inks suitable for inkjet and screen printing and compatible with the structure to be monitored will be developed and the SHM capabilities will be evaluated.

With regard to real applications, depending on the operational conditions, it might be necessary to consider the environmental conditions because temperature and humidity have an influence on the electrical resistance of CFRP and CNT modified polymers. To determine an accurate damage location over a changing temperature/humidity profile it is necessary to

know the influence of these parameters on the electrical resistance of the considered structure.

References

[1] Tai NH, Yip MC, Lin JL. Effects of low-energy impact on the fatigue behavior of carbon/epoxy composites. Composites Science and Technology 1998;58(1):1–8.

[2] Ramkumar RL. Effect of Low-Velocity Impact Damage on the Fatigue Behavior of Graphite/Epoxy Laminates. In: Long-term behavior of composites. American Society for Testing and Materials; 1983, 116–135.

[3] Prichard JC, Hogg PJ. The role of impact damage in post-impact compression testing. Composites 1990;21(6):503–11.

[4] Richardson MOW, Wisheart MJ. Review of low-velocity impact properties of composite materials. Composites Part A: Applied Science and Manufacturing 1996;27(12):1123–31.

[5] Åström BT. Manufacturing of polymer composites. London: Chapman & Hall; 1997.

[6] Gholizadeh S. A review of non-destructive testing methods of composite materials. Procedia Structural Integrity 2016;1:50–7.

[7] Cheng L, Tian GY. Comparison of Nondestructive Testing Methods on Detection of Delaminations in Composites. Journal of Sensors 2012;2012(3):1–7.

[8] Garnier C, Pastor M-L, Eyma F, Lorrain B. The detection of aeronautical defects in situ on composite structures using Non Destructive Testing. Composite Structures 2011;93(5):1328–36.

[9] Roh HD, Lee H, Park Y-B. Structural health monitoring of carbon-material-reinforced polymers using electrical resistance measurement. International Journal of Precision Engineering and Manufacturing-Green Technology 2016;3(3):311–21.

[10] Chung DDL. Structural health monitoring by electrical resistance measurement. Smart Materials and Structures 2001;10(4):624–36.

[11] Schulte K, Baron C. Load and failure analyses of CFRP laminates by means of electrical resistivity measurements. Composites Science and Technology 1989;36(1):63–76.

[12] Abry J. In situ detection of damage in CFRP laminates by electrical resistance measurements. Composites Science and Technology 1999;59(6):925–35.

[13] Wen J, Xia Z, Choy F. Damage detection of carbon fiber reinforced polymer composites via electrical resistance measurement. Composites Part B: Engineering 2011;42(1):77–86.

[14] Kaddour AS, Al-Salehi FAR, Al-Hassani STS, Hinton MJ. Electrical resistance measurement technique for detecting failure in CFRP materials at high strain rates. Composites Science and Technology 1994;51(3):377–85.
[15] Todoroki A, YOSHIDA J. Electrical Resistance Change of Unidirectional CFRP Due to Applied Load. JSME International Journal Series A Solid Mechanics and Material Engineering 2004;47(3):357–64.
[16] Schüler R, Joshi SP, Schulte K. Damage detection in CFRP by electrical conductivity mapping. Composites Science and Technology 2001;61(6):921–30.
[17] Kupke M, Schulte K, Schüler R. Non-destructive testing of FRP by d.c. and a.c. electrical methods. Composites Science and Technology 2001;61(6):837–47.
[18] Takahashi K, Hahn HT. Towards practical application of electrical resistance change measurement for damage monitoring using an addressable conducting network. Structural Health Monitoring 2011;11(3):367–77.
[19] Lee H-H, Chou K-S, Huang K-C. Inkjet printing of nanosized silver colloids. Nanotechnology 2005;16(10):2436–41.
[20] Smith PJ, Shin D-Y, Stringer JE, Derby B, Reis N. Direct ink-jet printing and low temperature conversion of conductive silver patterns. Journal of Materials Science 2006;41(13):4153–8.
[21] Perelaer J, Hendriks CE, Laat, Antonius W M de, Schubert US. One-step inkjet printing of conductive silver tracks on polymer substrates. Nanotechnology 2009;20(16):165303.
[22] Muto N, Arai Y, Shin SG, Matsubara H, Yanagida H, Sugita M et al. Hybrid composites with self-diagnosing function for preventing fatal fracture. Composites Science and Technology 2001;61(6):875–83.
[23] Fiedler B, Gojny FH, Wichmann MHG, Bauhofer W, Schulte K. Can carbon nanotubes be used to sense damage in composites? Annales de Chimie Science des Matériaux 2004;29(6):81–94.
[24] Thostenson ET, Chou T-W. Carbon Nanotube Networks: Sensing of Distributed Strain and Damage for Life Prediction and Self Healing. Advanced Materials 2006;18(21):2837–41.
[25] Wichmann MHG, Buschhorn ST, Gehrmann J, Schulte K. Piezoresistive response of epoxy composites with carbon nanoparticles under tensile load. Physical Review B 2009;80(24):667.
[26] Böger L, Wichmann MHG, Meyer LO, Schulte K. Load and health monitoring in glass fibre reinforced composites with an electrically conductive nanocomposite epoxy matrix. Composites Science and Technology 2008;68(7-8):1886–94.

[27] Alamusi, Hu N, Fukunaga H, Atobe S, Liu Y, Li J. Piezoresistive strain sensors made from carbon nanotubes based polymer nanocomposites. Sensors 2011;11(11):10691–723.
[28] Meeuw H, Viets C, Liebig WV, Schulte K, Fiedler B. Morphological influence of carbon nanofillers on the piezoresistive response of carbon nanoparticle/epoxy composites under mechanical load. European Polymer Journal 2016;85:198–210.
[29] Li C, Thostenson ET, Chou T-W. Sensors and actuators based on carbon nanotubes and their composites: A review. Composites Science and Technology 2008;68(6):1227–49.
[30] Gao L, Chou T-W, Thostenson ET, Zhang Z, Coulaud M. In situ sensing of impact damage in epoxy/glass fiber composites using percolating carbon nanotube networks. Carbon 2011;49(10):3382–5.
[31] Pavlopoulou S, Soutis C, Manson G. Non-destructive inspection of adhesively bonded patch repairs using Lamb waves. Plastics, Rubber and Composites 2013;41(2):61–8.
[32] Caminero MA, Pavlopoulou S, Lopez-Pedrosa M, Nicolaisson BG, Pinna C, Soutis C. Analysis of adhesively bonded repairs in composites: Damage detection and prognosis. Composite Structures 2013;95:500–17.
[33] Davis C, Baker W, Moss SD, Galea SC, Jones R. In situ health monitoring of bonded composite repairs using a novel fiber Bragg grating sensing arrangement. In: Proc. SPIE 4934, Smart Materials II, p. 140–149.
[34] Chung DDL. Carbon fiber composites. Norwich, NY: Knovel; 2002.
[35] Minus M, Kumar S. The processing, properties, and structure of carbon fibers. JOM 2005;57(2):52–8.
[36] Fitzer E, Kochling K-H, Boehm HP, Marsh H. Recommended terminology for the description of carbon as a solid (IUPAC Recommendations 1995). Pure and Applied Chemistry 1995;67(3).
[37] Donnet J-B. Carbon fibers. 3rd ed. New York: Marcel Dekker; 1998.
[38] Chung DDL. Electrical applications of carbon materials. Journal of Materials Science 2004;39(8):2645–61.
[39] Edie DD. The effect of processing on the structure and properties of carbon fibers. Carbon 1998;36(4):345–62.
[40] Chung DDL. Composite materials: Science and applications. 2nd ed. London, New York: Springer; 2010.
[41] Bennett S, Johnson D. Structural heterogeneity in carbon fibers. In: Proceedings of the Fifth London International Carbon and Graphite Conference: Society of Chemical Industry; 1978, p. 377–386.

[42] dos Santos AS, Leite TdON, Furtado CA, Welter C, Pardini LC, Silva GG. Morphology, thermal expansion, and electrical conductivity of multiwalled carbon nanotube/epoxy composites. Journal of Applied Polymer Science 2008;108(2):979–86.
[43] Bryning MB, Islam MF, Kikkawa JM, Yodh AG. Very Low Conductivity Threshold in Bulk Isotropic Single-Walled Carbon Nanotube-Epoxy Composites. Advanced Materials 2005;17(9):1186–91.
[44] Barrau S, Demont P, Peigney A, Laurent C, Lacabanne C. DC and AC Conductivity of Carbon Nanotubes–Polyepoxy Composites. Macromolecules 2003;36(14):5187–94.
[45] Gallo GJ, Thostenson ET. Electrical characterization and modeling of carbon nanotube and carbon fiber self-sensing composites for enhanced sensing of microcracks. Materials Today Communications 2015;3:17–26.
[46] Todoroki A, Tanaka M, Shimamura Y. Measurement of orthotropic electric conductance of CFRP laminates and analysis of the effect on delamination monitoring with an electric resistance change method. Composites Science and Technology 2002;62(5):619–28.
[47] Wang S, Downes R, Young C, Haldane D, Hao A, Liang R et al. Carbon Fiber/Carbon Nanotube Buckypaper Interply Hybrid Composites: Manufacturing Process and Tensile Properties. Advanced Engineering Materials 2015;17(10):1442–53.
[48] Wang S, Chung DDL. Electrical behavior of carbon fiber polymer-matrix composites in the through-thickness direction. Journal of Materials Science 2000;35(1):91–100.
[49] Yamane T, Todoroki A, Fujita H, Kawashima A, Sekine N. Electric current distribution of carbon fiber reinforced polymer beam: Analysis and experimental measurements. Advanced Composite Materials 2016;25(6):497–513.
[50] Yamane T, Todoroki A. Analysis of electric current density in carbon fiber reinforced plastic laminated plates with angled plies. Composite Structures 2017;166:268–76.
[51] Iijima S. Helical microtubules of graphitic carbon. Nature 1991;354(6348):56–8.
[52] Iijima S, Ichihashi T. Single-shell carbon nanotubes of 1-nm diameter. Nature 1993;363(6430):603–5.
[53] Fiedler B, Gojny FH, Wichmann MHG, Nolte MCM, Schulte K. Fundamental aspects of nano-reinforced composites. Composites Science and Technology 2006;66(16):3115–25.

[54] Yu, Lourie, Dyer, Moloni, Kelly, Ruoff. Strength and breaking mechanism of multiwalled carbon nanotubes under tensile load. Science 2000;287(5453):637–40.
[55] Yu, Files, Arepalli, Ruoff. Tensile loading of ropes of single wall carbon nanotubes and their mechanical properties. Phys Rev Lett 2000;84(24):5552–5.
[56] Li C. Elastic moduli of multi-walled carbon nanotubes and the effect of van der Waals forces. Composites Science and Technology 2003;63(11):1517–24.
[57] Treacy MMJ, Ebbesen TW, Gibson JM. Exceptionally high Young's modulus observed for individual carbon nanotubes. Nature 1996;381(6584):678–80.
[58] Dresselhaus MS, Dresselhaus G, Eklund PC. C60-Related Tubules and Spherules. In: Dresselhaus MS, Dresselhaus G, Eklund PC, editors. Science of fullerenes and carbon nanotubes. 3rd ed. San Diego: Academic Press; 2002, p. 756–869.
[59] Saito R, Fujita M, Dresselhaus G, Dresselhaus MS. Electronic structure of chiral graphene tubules. Applied Physics Letters 1992;60(18):2204–6.
[60] Odom TW, Huang J-L, Kim P, Lieber CM. Atomic structure and electronic properties of single-walled carbon nanotubes. Nature 1998;391(6662):62–4.
[61] Wilder JWG, Venema LC, Rinzler AG, Smalley RE, Dekker C. Electronic structure of atomically resolved carbon nanotubes. Nature 1998;391(6662):59–62.
[62] Hiura H, Ebbesen TW, Fujita J, Tanigaki K, Takada T. Role of sp3 defect structures in graphite and carbon nanotubes. Nature 1994;367(6459):148–51.
[63] Dai H, Wong EW, Lieber CM. Probing Electrical Transport in Nanomaterials: Conductivity of Individual Carbon Nanotubes. Science 1996;272(5261):523–6.
[64] Stauffer D, Aharony A. Introduction to percolation theory. 2nd ed. London, Washington, DC: Taylor & Francis; 1992.
[65] Stauffer D. Scaling theory of percolation clusters. Physics Reports 1979;54(1):1–74.
[66] Balberg I, Anderson CH, Alexander S, Wagner N. Excluded volume and its relation to the onset of percolation. Physical Review B 1984;30(7):3933–43.
[67] Bauhofer W, Kovacs JZ. A review and analysis of electrical percolation in carbon nanotube polymer composites. Composites Science and Technology 2009;69(10):1486–98.
[68] Sandler JKW, Kirk JE, Kinloch IA, Shaffer MSP, Windle AH. Ultra-low electrical percolation threshold in carbon-nanotube-epoxy composites. Polymer 2003;44(19):5893–9.
[69] Kovacs JZ, Velagala BS, Schulte K, Bauhofer W. Two percolation thresholds in carbon nanotube epoxy composites. Composites Science and Technology 2007;67(5):922–8.

[70] McNally T, Pötschke P, Halley P, Murphy M, Martin D, Bell SEJ et al. Polyethylene multiwalled carbon nanotube composites. Polymer 2005;46(19):8222–32.
[71] Kilbride BE, Coleman JN, Fraysse J, Fournet P, Cadek M, Drury A et al. Experimental observation of scaling laws for alternating current and direct current conductivity in polymer-carbon nanotube composite thin films. Journal of Applied Physics 2002;92(7):4024–30.
[72] Fisher JC, Giaever I. Tunneling Through Thin Insulating Layers. Journal of Applied Physics 1961;32(2):172–7.
[73] Li C, Thostenson ET, Chou T-W. Dominant role of tunneling resistance in the electrical conductivity of carbon nanotube–based composites. Applied Physics Letters 2007;91(22):223114.
[74] Yu Y, Song G, Sun L. Determinant role of tunneling resistance in electrical conductivity of polymer composites reinforced by well dispersed carbon nanotubes. Journal of Applied Physics 2010;108(8):84319.
[75] Simmons JG. Generalized Formula for the Electric Tunnel Effect between Similar Electrodes Separated by a Thin Insulating Film. Journal of Applied Physics 1963;34(6):1793–803.
[76] Farrar CR, Worden K. An introduction to structural health monitoring. Philos Trans A Math Phys Eng Sci 2007;365(1851):303–15.
[77] Wilson CL, Lonkar K, Roy S, Kopsaftopoulos F, Chang F-K. 7.20 Structural Health Monitoring of Composites. In: Zweben CH, Beaumont PWR, editors. Comprehensive composite materials II. Amsterdam, Netherlands: Elsevier; 2018, p. 382–407.
[78] Cai J, Qiu L, Yuan S, Shi L, Liu P, Liang D. Structural Health Monitoring for Composite Materials. In: Hu N, editor. Composites and their applications. Rijeka, Croatia: InTech; 2012.
[79] Ciang CC, Lee J-R, Bang H-J. Structural health monitoring for a wind turbine system: A review of damage detection methods. Measurement Science and Technology 2008;19(12):122001.
[80] Diamanti K, Soutis C. Structural health monitoring techniques for aircraft composite structures. Progress in Aerospace Sciences 2010;46(8):342–52.
[81] Balageas D. Structural health monitoring. London, Newport Beach, CA: ISTE; 2006.
[82] Staszewski WJ, Boller C, Tomlinson GR. Health monitoring of aerospace structures: Smart sensor technologies and signal processing. West Sussex: John Wiley & Sons; op. 2004.
[83] Giurgiutiu V. Structural health monitoring of aerospace composites. London: Academic Press; 2016.

[84] Takeda N. Characterization of microscopic damage in composite laminates and real-time monitoring by embedded optical fiber sensors. International Journal of Fatigue 2002;24(2-4):281–9.

[85] Majumder M, Gangopadhyay TK, Chakraborty AK, Dasgupta K, Bhattacharya DK. Fibre Bragg gratings in structural health monitoring—Present status and applications. Sensors and Actuators A: Physical 2008;147(1):150–64.

[86] Meltz G, Morey WW, Glenn WH. Formation of Bragg gratings in optical fibers by a transverse holographic method. Opt Lett 1989;14(15):823–5.

[87] Lamb H. On Waves in an Elastic Plate. Proceedings of the Royal Society A: Mathematical, Physical and Engineering Sciences 1917;93(648):114–28.

[88] Kessler SS, Spearing SM, Soutis C. Damage detection in composite materials using Lamb wave methods. Smart Materials and Structures 2002;11(2):269–78.

[89] Groot PJ de, Wijnen PAM, Janssen RBF. Real-time frequency determination of acoustic emission for different fracture mechanisms in carbon/epoxy composites. Composites Science and Technology 1995;55(4):405–12.

[90] Loutas TH, Roulias D, Pauly E, Kostopoulos V. The combined use of vibration, acoustic emission and oil debris on-line monitoring towards a more effective condition monitoring of rotating machinery. Mechanical Systems and Signal Processing 2011;25(4):1339–52.

[91] Prasse T, Michel F, Mook G, Schulte K, Bauhofer W. A comparative investigation of electrical resistance and acoustic emission during cyclic loading of CFRP laminates. Composites Science and Technology 2001;61(6):831–5.

[92] Wisham M, Barton DP. Comparative vacuum monitoring: a new method of in-situ real-time crack detection and monitoring. Proceeding of 10th Asia-Pacific Conference On Nondestructive Testing 2001.

[93] Roach D. Real time crack detection using mountable comparative vacuum monitoring sensors. Smart Structures and Systems 2009;5(4):317–28.

[94] Boller C, Meyendorf N. State-of-the-Art in Structural Health Monitoring in Aeronautics. In: Proc. of Internat. Symposium on NDT in Aerospace, Fürth/Bavaria, Germany, December 3-5, 2008, p. 243–252.

[95] Montalvao D. A Review of Vibration-based Structural Health Monitoring with Special Emphasis on Composite Materials. The Shock and Vibration Digest 2006;38(4):295–324.

[96] Chung DDL. Carbon materials for structural self-sensing, electromagnetic shielding and thermal interfacing. Carbon 2012;50(9):3342–53.

[97] Choi H, Choi S, Cha H. Structural Health Monitoring system based on strain gauge enabled wireless sensor nodes. In: International Conference on Networked Sensing Systems, 2008. Piscataway, NJ: IEEE; 2008, p. 211–214.

[98] Caminero MA, Lopez-Pedrosa M, Pinna C, Soutis C. Damage monitoring and analysis of composite laminates with an open hole and adhesively bonded repairs using digital image correlation. Composites Part B: Engineering 2013;53:76–91.
[99] Krüger M, Grosse CU, Marrón PJ. Wireless Structural Health Monitoring Using MEMS. Key Engineering Materials 2005;293-294:625–34.
[100] Ogaja C, Li X, Rizos C. Advances in structural monitoring with Global Positioning System technology: 1997–2006. Journal of Applied Geodesy 2007;1(3):26.
[101] Seo D-C, Lee J-J. Damage detection of CFRP laminates using electrical resistance measurement and neural network. Composite Structures 1999;47(1-4):525–30.
[102] Weber I, Schwartz P. Monitoring bending fatigue in carbon-fibre/epoxy composite strands: A comparison between mechanical and resistance techniques. Composites Science and Technology 2001;61(6):849–53.
[103] Prabhakaran R. Damage assessment through electrical resistance measurement in graphite fiber-reinforced composites. Experimental Techniques 1990;14(1):16–20.
[104] Muto N, Yanagida H, Nakatsuji T, Sugita M, Ohtsuka Y, Arai Y. Design of intelligent materials with self-diagnosing function for preventing fatal fracture. Smart Materials and Structures 1992;1(4):324–9.
[105] Schulte K. Damage monitoring in polymer matrix structures. Le Journal de Physique IV 1993;3(C7):1629-1636.
[106] Ceysson O, Salvia M, Vincent L. Damage mechanisms characterisation of carbon fibre/epoxy composite laminates by both electrical resistance measurements and acoustic emission analysis. Scripta Materialia 1996;34(8):1273–80.
[107] Park JB, Okabe T, Takeda N. New concept for modeling the electromechanical behavior of unidirectional carbon-fiber-reinforced plastic under tensile loading. Smart Materials and Structures 2003;12(1):105–14.
[108] Masson LC, Irving PE. Comparison of experimental and simulation studies of location of impact damage in polymer composites using electrical potential techniques. In: Proc. SPIE 4073, Fifth European Conference on Smart Structures and Materials; 2000, p. 182–193.
[109] Todoroki A, Tanaka Y, Shimamura Y. Multi-prove electric potential change method for delamination monitoring of graphite/epoxy composite plates using normalized response surfaces. Composites Science and Technology 2004;64(5):749–58.
[110] Angelidis N, Khemiri N, Irving PE. Experimental and finite element study of the electrical potential technique for damage detection in CFRP laminates. Smart Materials and Structures 2005;14(1):147–54.

[111] Wang D, Wang S, Chung DDL, Chung JH. Comparison of the Electrical Resistance and Potential Techniques for the Self-sensing of Damage in Carbon Fiber Polymer-Matrix Composites. Journal of Intelligent Material Systems and Structures 2016;17(10):853–61.

[112] Cheney M, Isaacson D, Newell JC. Electrical Impedance Tomography. SIAM Rev. 1999;41(1):85–101.

[113] Fan W, Wang H, Cui Z. Damage detection of CFRP composites using open electrical impedance tomography. In: 2015 IEEE International Instrumentation and Measurement Technology Conference (I2MTC) Proceedings: IEEE; 2015, p. 1377–1381.

[114] Escalona Galvis LW, Diaz-Montiel P, Venkataraman S. Optimal Electrode Selection for Electrical Resistance Tomography in Carbon Fiber Reinforced Polymer Composites. Materials 2017;10(2).

[115] Baltopoulos A, Polydorides N, Pambaguian L, Vavouliotis A, Kostopoulos V. Damage identification in carbon fiber reinforced polymer plates using electrical resistance tomography mapping. Journal of Composite Materials 2012;47(26):3285–301.

[116] Cagáň J. Hardware implementation of electrical resistance tomography for damage detection of carbon fibre–reinforced polymer composites. Structural Health Monitoring 2016;16(2):129–41.

[117] Zarafshani A, Chatwin C, Bach T, Zheng B. Using planar electrical impedance tomography as a structural health monitoring method to detect and evaluate the damage to CFRP composite. In: Aerospace and Electronics Conference (NAECON) and Ohio Innovation Summit (OIS); 2016, p. 74–79.

[118] Leopold C, Augustin T, Schwebler T, Lehmann J, Liebig WV, Fiedler B. Influence of carbon nanoparticle modification on the mechanical and electrical properties of epoxy in small volumes. J Colloid Interface Sci 2017;506:620–32.

[119] Wicks S, Barber D, Raghavan A, Dunn C, Daniel L, Kessler S et al. Health monitoring of carbon nanotube (CNT) hybrid advanced composites for space applications. Proceedings of ECSSMMT 09 Conference, Toulouse, France 2009.

[120] Viets C, Kaysser S, Schulte K. Damage mapping of GFRP via electrical resistance measurements using nanocomposite epoxy matrix systems. Composites Part B: Engineering 2014;65:80–8.

[121] Naghashpour A, van Hoa S. A technique for real-time detection, location and quantification of damage in large polymer composite structures made of electrically non-conductive fibers and carbon nanotube networks. Nanotechnology 2013;24(45):455502.

[122] Zhang D, Ye L, Wang D, Tang Y, Mustapha S, Chen Y. Assessment of transverse impact damage in GF/EP laminates of conductive nanoparticles using electrical resistivity tomography. Composites Part A: Applied Science and Manufacturing 2012;43(9):1587–98.
[123] Gungor S, Bakis CE. Indentation damage detection in glass/epoxy composite laminates with electrically tailored conductive nanofiller. Journal of Intelligent Material Systems and Structures 2016;27(5):679–88.
[124] Hou T-C, Loh KJ, Lynch JP. Spatial conductivity mapping of carbon nanotube composite thin films by electrical impedance tomography for sensing applications. Nanotechnology 2007;18(31):315501.
[125] Loh KJ, Hou T-C, Lynch JP, Kotov NA. Carbon Nanotube Sensing Skins for Spatial Strain and Impact Damage Identification. J Nondestruct Eval 2009;28(1):9–25.
[126] Baltopoulos A, Polydorides N, Pambaguian L, Vavouliotis A, Kostopoulos V. Exploiting carbon nanotube networks for damage assessment of fiber reinforced composites. Composites Part B: Engineering 2015;76:149–58.
[127] Loyola BR, Briggs TM, Arronche L, Loh KJ, La Saponara V, O'Bryan G et al. Detection of spatially distributed damage in fiber-reinforced polymer composites. Structural Health Monitoring 2013;12(3):225–39.
[128] Loyola BR, La Saponara V, Loh KJ, Briggs TM, O'Bryan G, Skinner JL. Spatial Sensing Using Electrical Impedance Tomography. IEEE Sensors J. 2013;13(6):2357–67.
[129] Tallman TN, Gungor S, Wang KW, Bakis CE. Damage detection via electrical impedance tomography in glass fiber/epoxy laminates with carbon black filler. Structural Health Monitoring 2014;14(1):100–9.
[130] Tallman TN, Semperlotti F, Wang K. Enhanced delamination detection in multifunctional composites through nanofiller tailoring. Journal of Intelligent Material Systems and Structures 2015;26(18):2565–76.
[131] Tallman TN, Wang KW. Damage and strain identification in multifunctional materials via electrical impedance tomography with constrained sine wave solutions. Structural Health Monitoring 2016;15(2):235–44.
[132] Tallman TN, Hernandez JA. The effect of error and regularization norms on strain and damage identification via electrical impedance tomography in piezoresistive nanocomposites. NDT & E International 2017;91:156–63.
[133] Tallman TN, Gungor S, Koo GM, Bakis CE. On the inverse determination of displacements, strains, and stresses in a carbon nanofiber/polyurethane nanocomposite from conductivity data obtained via electrical impedance tomography. Journal of Intelligent Material Systems and Structures 2017;107:2617-2629.

[134] Gallo GJ, Thostenson ET. Spatial damage detection in electrically anisotropic fiber-reinforced composites using carbon nanotube networks. Composite Structures 2016;141:14–23.
[135] Mactabi R, Rosca ID, Hoa SV. Monitoring the integrity of adhesive joints during fatigue loading using carbon nanotubes. Composites Science and Technology 2013;78:1–9.
[136] Lim AS, Melrose ZR, Thostenson ET, Chou T-W. Damage sensing of adhesively-bonded hybrid composite/steel joints using carbon nanotubes. Composites Science and Technology 2011;71(9):1183–9.
[137] Zhao Y, Schagerl M. Shear Stress Monitoring of a Single-Lap Joint Using Inkjet-Printed Carbon Nanotube Strain Distribution Sensor. 8th European Workshop on Structural Health Monitoring 2016.
[138] Kang M-H, Choi J-H, Kweon J-H. Fatigue life evaluation and crack detection of the adhesive joint with carbon nanotubes. Composite Structures 2014;108:417–22.
[139] Kim C-H, Choi J-H, Kweon J-H. Defect detection in adhesive joints using the impedance method. Composite Structures 2015;120:183–8.
[140] Fernández Sánchez-Romate XX, Molinero J, Jiménez-Suárez A, Sánchez M, Güemes A, Ureña A. Carbon Nanotube-Doped Adhesive Films for Detecting Crack Propagation on Bonded Joints: A Deeper Understanding of Anomalous Behaviors. ACS Appl Mater Interfaces 2017;9(49):43267–74.
[141] de Gans B-J, Duineveld PC, Schubert US. Inkjet Printing of Polymers: State of the Art and Future Developments. Advanced Materials 2004;16(3):203–13.
[142] Shackelford JF. Introduction to Materials Science for Engineers. 8th ed.: Pearson; 2016.
[143] Kamyshny A. Metal-based Inkjet Inks for Printed Electronics. The Open Applied Physics Journal 2011;4(1):19–36.
[144] Allen GL, Bayles RA, Gile WW, Jesser WA. Small particle melting of pure metals. Thin Solid Films 1986;144(2):297–308.
[145] Kamyshny A, Magdassi S. Conductive Nanomaterials for Printed Electronics. Small 2014;10(17):3515–35.
[146] Buffat P, Borel J-P. Size effect on the melting temperature of gold particles. Physical Review A 1976;13(6):2287–98.
[147] Dearden AL, Smith PJ, Shin D-Y, Reis N, Derby B, O'Brien P. A Low Curing Temperature Silver Ink for Use in Ink-Jet Printing and Subsequent Production of Conductive Tracks. Macromolecular Rapid Communications 2005;26(4):315–8.

[148] Jeon E-B, Fujimura T, Takahashi K, Kim H-S. An investigation of contact resistance between carbon fiber/epoxy composite laminate and printed silver electrode for damage monitoring. Composites Part A: Applied Science and Manufacturing 2014;66:193–200.
[149] Takahashi K, Namiki K, Fujimura T, Jeon E-B, Kim H-S. Instant electrode fabrication on carbon-fiber-reinforced plastic structures using metal nano-ink via flash light sintering for smart sensing. Composites Part B: Engineering 2015;76:167–73.
[150] Joo S-J, Yu M-H, Jeon E-B, Kim H-S. In situ fabrication of copper electrodes on carbon-fiber-reinforced polymer (CFRP) for damage monitoring by printing and flash light sintering. Composites Science and Technology 2017;142:189–97.
[151] Kholghi Eshkalak S, Chinnappan A, Jayathilaka WADM, Khatibzadeh M, Kowsari E, Ramakrishna S. A review on inkjet printing of CNT composites for smart applications. Applied Materials Today 2017;9:372–86.
[152] Tortorich RP, Choi J-W. Inkjet Printing of Carbon Nanotubes. Nanomaterials 2013;3(3):453–68.
[153] Li J, Ye F, Vaziri S, Muhammed M, Lemme MC, Östling M. Efficient inkjet printing of graphene. Advanced Materials 2013;25(29):3985–92.
[154] Torrisi F, Hasan T, Wu W, Sun Z, Lombardo A, Kulmala TS et al. Inkjet-printed graphene electronics. ACS Nano 2012;6(4):2992–3006.
[155] ASTM. ASTM D7136 / D136M-05, Standard Test Method for Measuring the Damage Resistance of a Fiber-Reinforced Polymer Matrix Composite to a Drop-Weight Impact Event. West Conshohocken, PA: ASTM International; 2005.
[156] Hirano Y, Yamane T, Todoroki A. Through-thickness electric conductivity of toughened carbon-fibre-reinforced polymer laminates with resin-rich layers. Composites Science and Technology 2016;122:67–72.
[157] Lonjon A, Demont P, Dantras E, Lacabanne C. Electrical conductivity improvement of aeronautical carbon fiber reinforced polyepoxy composites by insertion of carbon nanotubes. Journal of Non-Crystalline Solids 2012;358(15):1859–62.
[158] Lodge KJ. The electrical properties of joints in carbon fibre composites. Composites 1982;13(3):305–10.
[159] Hirano Y, Katsumata S, Iwahori Y, Todoroki A. Artificial lightning testing on graphite/epoxy composite laminate. Composites Part A: Applied Science and Manufacturing 2010;41(10):1461–70.

[160] Zhang D, Ye L, Deng S, Zhang J, Tang Y, Chen Y. CF/EP composite laminates with carbon black and copper chloride for improved electrical conductivity and interlaminar fracture toughness. Composites Science and Technology 2012;72(3):412–20.

[161] Xia Z, Okabe T, Park JB, Curtin WA, Takeda N. Quantitative damage detection in CFRP composites. Composites Science and Technology 2003;63(10):1411–22.

[162] Gojny FH, Wichmann MHG, Köpke U, Fiedler B, Schulte K. Carbon nanotube-reinforced epoxy-composites: Enhanced stiffness and fracture toughness at low nanotube content. Composites Science and Technology 2004;64(15):2363–71.

[163] Knoll JB, Riecken BT, Kosmann N, Chandrasekaran S, Schulte K, Fiedler B. The effect of carbon nanoparticles on the fatigue performance of carbon fibre reinforced epoxy. Composites Part A: Applied Science and Manufacturing 2014;67:233–40.

[164] Chandrasekaran S, Sato N, Tölle F, Mülhaupt R, Fiedler B, Schulte K. Fracture toughness and failure mechanism of graphene based epoxy composites. Composites Science and Technology 2014;97:90–9.

[165] Johannsen I, Jaksik K, Wirch N, Pötschke P, Fiedler B, Schulte K. Electrical conductivity of melt-spun thermoplastic poly(hydroxy ether of bisphenol A) fibres containing multi-wall carbon nanotubes. Polymer 2016;97:80–94.

[166] Kovacs JZ, Andresen K, Pauls JR, Garcia CP, Schossig M, Schulte K et al. Analyzing the quality of carbon nanotube dispersions in polymers using scanning electron microscopy. Carbon 2007;45(6):1279–88.

[167] Kosmann J, Holzhütter D, Löbel T, Hühne C, Schollerer M. High Resolution Digital Image Correlation Strain Measurements of Adhesively Bonded Joints. 17th European Conference on Composite Materials (ECCM17) 2016.

[168] Todoroki A, Haruyama D, Mizutani Y, Suzuki Y, Yasuoka T. Electrical Resistance Change of Carbon/Epoxy Composite Laminates under Cyclic Loading under Damage Initiation Limit. Open Journal of Composite Materials 2014;04(01):22–31.

[169] Monetti RA, Albano EV. Critical behavior of the site percolation model on the square lattice in aLM geometry. Zeitschrift für Physik B Condensed Matter 1991;82(1):129–34.

[170] Marrink SJ, Knackstedt MA. Percolation thresholds on elongated lattices. Journal of Physics A: Mathematical and General 1999;32(44):L461-L466.

[171] Marrink SJ, Knackstedt MA. Finite size scaling for percolation on elongated lattices in two and three dimensions. Physical Review E 2000;62(3):3205–14.

[172] Leopold C, Liebig WV, Wittich H, Fiedler B. Size effect of graphene nanoparticle modified epoxy matrix. Composites Science and Technology 2016;134:217–25.

[173] Hobbiebrunken T, Fiedler B, Hojo M, Tanaka M. Experimental determination of the true epoxy resin strength using micro-scaled specimens. Composites Part A: Applied Science and Manufacturing 2007;38(3):814–8.
[174] ASTM. ASTM D3379-75(1989)e1, Standard Test Method for Tensile Strength and Young's Modulus for High-Modulus Signle-Filament Materials (Withdrawn 1998). West Conshohocken, PA: ASTM International; 1975.
[175] Shui X, Chung DDL. A piezoresistive carbon filament polymer-matrix composite strain sensor. Smart Materials and Structures 1996;5(2):243–6.

Supervised student theses and research projects

Schmidt, Marlo. Messstrategien für die elektrische Widerstandsmessung mit Elektrodennetzwerken zur Detektion und Lokalisierung von Schlagschäden an CFK-Laminaten. Master thesis, Hamburg University of Technology, 2018.

Hubert, Nils. Modifizierung und Analyse von reaktiven Klebmassen für Anwendungen mit hohen Schlagbelastungen. Master thesis, Hamburg University of Technology, 2018.

Steilmann, Thomas. Untersuchung der Auswirkung von plasmaaktivierten Kohlenstofffasern auf die Faser-Matrix-Anhaftung mit dem Single-Fiber-Fragmentation Test. Bachelor thesis, Hamburg University of Technology, 2018.

Grunert, Danny. Schadensdetektion und -lokalisierung an CFK mit im Laminat integrierten Leiterbahnen mittels elektrischer Widerstandsmessung. Research project, Hamburg University of Technology, 2018.

Reese, Julian. Parameterstudie über die Aktivierung von CFK-Strukturen durch Plasmabehandlung zur Verbesserung der Klebeeigenschaften und Bruchfestigkeit. Master thesis, Hamburg University of Technology, 2017.

Karsten, Julian. Schadendetektion und -lokalisierung an CFK Klebeverbindungen unter zyklischer Belastung. Master thesis, Hamburg University of Technology, 2017.

Knecht, Fabian. Untersuchung der Prozessparameter zur Applikation eines Cetyl-Schmierfilms. Bachelor thesis, Hamburg University of Technology, 2017.

Schmidt, Marlo. Investigation of the stress field in U-notched orthotropic laminates using analytical approaches. Research project, Hamburg University of Technology, 2017.

Leonhardt, Maren. Analysis of fatigue damage mechanisms in woven glass fiber fabric. Research project, Hamburg University of Technology, 2017.

Hubert, Nils. Vergleich von Methoden zur beschleunigten Dichtstoffaushärtung im Flugzeugbau. Research project, Hamburg University of Technology, 2017.

Manderla, Jannik. Detektion und Lokalisierung von Schlagschäden an CFK-Laminaten durch elektrische Widerstandsmessung mit Elektrodennetzwerken. Research project, 2017.

Kötter, Benedikt. Untersuchung der zerstörungsfreien Schadenserkennung von geklebten CFK-Komponenten mit Carbon Nanotube modifizierten Klebefilmen. Master thesis, Hamburg University of Technology, 2016.

Jungclaus, Simon. Konzeptentwicklung zur Funktionsintegration eines Online Structural Health Monitoring Verfahrens in eine FVK-Drehstabfeder. Master thesis, Hamburg University of Technology, 2016.

Schwebler, Thomas. Einfluss von Füllgrad und Partikelgeometrie auf die mechanischen Eigenschaften von Kohlenstoff-Nanopartikel-modifizierter Epoxidmatrix im Einzelfaser-Zugversuch. Bachelor thesis, Hamburg University of Technology, 2016.

Lehmann, Jonas. Einfluss von Füllgrad und Partikelgeometrie auf die elektrischen Eigenschaften von Kohlenstoff-Nanopartikel modifizierter Epoxidmatrix im Einzelfaser Zugversuch. Bachelor thesis, Hamburg University of Technology, 2016.

Grunert, Danny. Schadensdetektion und -lokalisierung an CFK mit aufgedruckten Leiterbahnen mittels elektrischer Widerstandsmessung. Bachelor thesis, Hamburg University of Technology, 2016.

Junge, Paul. Mechanische und elektrische Charakterisierung von Single-Walled Carbon Nanotube Polyester-Kompositen. Bachelor thesis, Hamburg University of Technology, 2016.

Höft, Sebastian. Mechanische und elektrische Charakterisierung von Single-Walled Carbon Nanotube-Epoxid-Kompositen. Master thesis, Hamburg University of Technology, 2015.

Wunderlich, Alexander. Konstruktion einer elektrisch-kontaktierenden Belastungseinheit. Bachelor thesis, Hamburg University of Technology, 2015.

Jungclaus, Simon. Überblick von Structural Health Monitoring Verfahren von Faserverbundstrukturen. Research project, Hamburg University of Technology, 2015.

Kötter, Benedikt. Untersuchung der elektrischen Eigenschaften von Filmen aus kohlenstoffnanopartikelmodifizierten Kunststoffen. Research project, Hamburg University of Technology, 2015.

Publications

Augustin T, Karsten J, Kötter B, Fiedler B (2018). Health monitoring of scarfed CFRP joints under cyclic loading via electrical resistance measurements using carbon nanotube modified adhesive films. *Composites Part A: Applied Science and Manufacturing*, 105:150-155.

Augustin T, Karsten J, Fiedler B (2018). Detection and localization of impact damages in carbon nanotube–modified epoxy adhesive films with printed circuits. *Structural Health Monitoring*, in press.

Augustin T, Grunert D, Langner H, Haverkamp V, Fiedler B (2017). Online monitoring of surface cracks and delaminations in carbon fiber/epoxy composites using silver nanoparticle based ink. *Advanced Manufacturing: Polymer & Composites Science*, 3(3):110-119.

Augustin T, Fiedler B (2017). Health monitoring of CFRP using printed circuits. *JEC composites magazine,* 117:61-63.

Leopold C, Augustin T, Schwebler T, Lehmann J, Liebig W, Fiedler B (2017). Influence of carbon nanoparticle modification on the mechanical and electrical properties of epoxy in small volumes. *Journal of Colloid and Interface Science*, 506:620-632.